Stochastic Processes and Interaction Dynamics in Bacterial Competition

Benedikt von Bronk

München 2018

Stochastic Processes and Interaction Dynamics in Bacterial Competition

Benedikt von Bronk

Dissertation
an der Fakultät für Physik
der Ludwig-Maximilians-Universität
München

vorgelegt von
Benedikt von Bronk
aus Bochum

München, den 02. August 2018

Erstgutachter: Prof. Dr. Joachim Rädler
Zweitgutachter: Prof. Dr. Erwin Frey
Tag der mündlichen Prüfung: 23.10.2018

Zusammenfassung

Diese Dissertation untersucht den Einfluss stochastischer Effekte auf die komplexe Interaktionsdynamik in bakteriellen Gemeinschaften und nutzt dafür neu entwickelte experimentelle Methoden und theoretische Modellierung.
In Mischung interagieren Populationen verschiedener Bakterienstämme sowohl kooperativ als auch kompetitiv. Im Rahmen dieser Arbeit wurde die räumliche Interaktionsdynamik des Colicin E2 Modellsystems untersucht, das aus toxinproduzierenden, -sensitiven und -resistenten Bakterien besteht. Hierbei findet die Toxinproduktion innerhalb der produzierenden Population jedoch nicht in jedem Individuum sondern nur durch zufällige Phänotypwechsel von Nichtproduzent zu Produzent statt. Die resultierende phänotypischen Heterogenität ist evolutionär notwendig, da produzierende Zellen bei der Toxinfreisetzung sterben.
Im Rahmen dieser Arbeit wird das Colicin E2-System zunächst ausführlich als konkretes Beispiel komplexer mikrobieller Systeme diskutiert, wobei besonders physikalische Modellierungsansätze herausgearbeitet werden (Kapitel 2).
Anschließend wird die Entwicklung des experimentellen Ansatzes dargestellt, der automatisierte Zoom-Fluoreszenz-Mikroskopie mit nanolitergenauer Probenvorbereitung kombiniert (Kapitel 3). Unterstützt von mathematischer und computergestützter Modellierung (Kapitel 4 und 5) wird dieser experimentelle Ansatz auf das Colicin E2 System angewandt.
Zunächst wird damit die Interaktion von toxinproduzierenden und -sensitiven Stämmen untersucht (Kapitel 6), wobei der experimentelle Ansatz es ermöglichte, die Interaktion von der Fast-Einzelzellebene bis hin zu makroskopischen Kolonien zu untersuchen. Dadurch konnte die Interaktionsdynamik in eine frühe stochastische und späte deterministische Phase unterteilt werden, wobei zum ersten mal gezeigt werden konnte, wie die stochastische Toxinproduktion Bistabilität im - typischerweise einzigartigen - Wettbewerbsausgang induziert. Bei hohen Zellzahlen wurde eine durchschnittliche phänotypische Heterogenität beobachtet, die die deterministische Makro-Dynamik bestimmte.
Durch die Erweiterung des Interaktionssystems um einen weiteren, resistenten Stamm (Kapitel 7) wurde das "Trittbrettfahren" als weitere Interaktionsform eingeführt, da der neue Stamm die Toxinwirkung ausnutzt ohne selbst zur Produktion beizutragen. Es konnte gezeigt werden, dass die anfängliche relative Positionierung der Zellen nicht nur Auswirkung auf die frühe stochastische Phase hat, sondern wegen einer Distanzabhängigkeit des "Trittbrettfahrens" langanhaltend ist.
Abschließend wird die Arbeit im breiteren Zusammenhang diskutiert und mögliche zukünftige Forschungsansätze aufgezeigt (Kapitel 8).
Die Haupterrungenschaft dieser Arbeit ist der erste experimentelle Nachweis, dass die Interaktionsdynamik im Colicin E2 System von Stochastizität in der Toxinproduktion beeinflusst wird - ermöglicht durch die neu entwickelte experimentelle Methode.

Abstract

This dissertation investigates the influence of stochastic processes on the complex interaction dynamics in bacterial communities using newly developed experimental and theoretical methods.
In mixed bacterial communities, populations of different bacterial strains interact with each other using competitive and cooperative traits. In this thesis, the spatially extended interaction dynamics in the Colicin E2 model system are investigated. This model system comprises toxin producer, sensitive, and/or resistant strains. Importantly, toxin production is subject to stochastic phenotype switches from non-producer to producer phenotype. The resulting phenotypic heterogeneity is crucial because toxin producing cells die in releasing the toxin.
In this thesis, the colicin E2 system is reviewed in more detail as a concrete example of complex microbial systems, which are discussed over various physical scales with a particular focus on modeling approaches (chapter 2).
Then, the development of a new multi-scale experimental approach is presented (chapter 3). This approach combined automated fluorescence time-lapse microscopy with zooming functionality and nano-liter precision sample preparation. In combination with mathematical and computational modelling of the bacterial interaction system (chapters 4 and 5), this approach was applied to the colicin E2 system.
First, focusing on the two-strain interaction between toxin producer and sensitive strain (chapter 6), the experimental approach facilitated tracking of the interaction dynamics over various scales from initial near single-cell level to later macroscopic colonies. This enabled to disentangle the initial stochastic from the later deterministic dynamics. In doing so, it was shown for the first time, how stochasticity in toxin production can induce competition outcome bistability. Furthermore, at large cell numbers, the degree of phenotypic heterogeneity was found to determine the macroscopic dynamics.
Then, the interaction system was extended with a third, resistant strain and investigated using the same methods (chapter 7). The third strain introduced cheating as a new interaction mechanisms as it exploited the toxin action without contributing to the production. Subsequently, it was shown that the relative positioning does not only play a role in the initial stochastic phase but plays an important role during the later deterministic phase due to distance dependent cheating.
Finally, the thesis concludes with discussing the presented work in a broader context and giving possible further research directions (chapter 8).
In conclusion, the thesis presents the first experimental proof of the relevance of stochastic toxin production for bacterial colicin E2 competition dynamics by using a new experimental approach for the multi-scale investigation of bacterial systems.

List of publications

Publications based on the results of this thesis:

[B1] **Benedikt von Bronk**, Sophia Anna Schaffer, Alexandra Götz, Madeleine Opitz (2017). Effects of Stochasticity and Division of Labor in Toxin Production on Two-strain Bacterial Competition in *Escherichia coli*. *PLoS Biology* 15(5): e2001457

[B2] **Benedikt von Bronk**, Alexandra Götz, Madeleine Opitz (2018). Complex microbial systems across different levels of description. *Physical Biology* 15: 051002

[B3] **Benedikt von Bronk**, Alexandra Götz, Madeleine Opitz (2018). Locality of interactions in three-strain bacterial competition in *E. coli*. *(accepted for publication in Physical Biology)*

Publications that are closely related to the investigations for this thesis:

[M1] Andreas Mader, **Benedikt von Bronk**, Benedikt Ewald, Sara Kesel, Karin Schnetz, Erwin Frey, Madeleine Opitz (2015). Amount of Colicin Release in Escherichia coli Is Regulated by Lysis Gene Expression of the Colicin E2 Operon. *PLoS ONE* 10(3): e0119124

[K1] Sara Kesel, **Benedikt von Bronk**, Carolina Falcon Garcia, Alexandra Götz, Oliver Lieleg and Madeleine Opitz (2017). Matrix composition determines dimensions of Bacillus subtilis NCIB 3610 biofilm colonies grown on LB agar. *RSC Advances* 7: 31886-31898

[G1] Alexandra Götz, Matthias Lechner, Andreas Mader, **Benedikt von Bronk**, Erwin Frey and Madeleine Opitz (2018). CsrA and its regulators control the timepoint of ColicinE2 release in *Escherichia coli*. *Scientific Reports* 8: 6537

[G2] Alexandra Götz, Andreas Mader, **Benedikt von Bronk**, Anna Weiß, Madeleine Opitz (2018). Gene expression noise in the ColicinE2 stress response system of *Escherichia coli*. *(in preparation)*

[S1] Almond Stöcker, Sarah Brockhaus, Sophia Schaffer, **Benedikt von Bronk**, Madeleine Opitz, Sonja Greven (2018). Boosting Functional Response Models for Location, Scale and Shape with an Application to Bacterial Competition. *(submitted for publication, preprint available https://arxiv.org/abs/1809.09881)*

Contents

Zusammenfassung v

Abstract vii

List of publications 129

1. Introduction 1

2. Concepts - From molecules to ecology 5
2.1. A hierarchy of description levels for bacterial systems 7
2.1.1. Gene regulatory networks 7
2.1.2. Single cells and phenotypic heterogeneity 10
2.1.3. Emergent collective properties 11
2.2. The colicin E2 system 13
2.2.1. Gene regulation of the colicin E2 operon 13
2.2.2. Phenotypic heterogeneity in colicin production 15
2.2.3. Population level and emergent ecological properties 16
2.3. Bacterial interactions 18
2.3.1. Well-mixed (non-spatial) systems 19
2.3.2. Spatially extended systems 21
2.4. Biofilm formation in Bacillus subtilis 23

3. Development of multi-scale fluorescence microscopy setup for automated long-term observation of bacterial interactions 27
3.1. Motivation and problem definition 27
3.2. Experimental approach 28
3.2.1. Bacterial culture 28
3.2.2. Sample preparation 31
3.2.3. Experimental setup 32
3.2.4. Automated image acquisition 33
3.3. Data analysis 35
3.3.1. Image analysis 36
3.3.2. Detail analysis 39
3.3.3. Data processing 40

3.4. Additional applications . . . 41
3.4.1. Biofilm cooperation . . . 41
3.4.2. Antibiotic screening . . . 41
3.5. Auxiliary high-resolution setup . . . 42
3.6. Discussion . . . 43

4. Population dynamics of colicin E2 producers 45
4.1. Phenotypic heterogeneity in colicin E2 production . . . 45
4.1.1. Experimental parameter determination . . . 46
4.2. Mathematical model of toxin producer fraction . . . 47
4.2.1. Master equations and deterministic rate equations for population dynamics . . . 47
4.2.2. Analytic solution of the population dynamics . . . 49
4.3. Numerical solution of the stochastic population dynamics . . . 51
4.3.1. Population survival conditions . . . 52
4.3.2. Survivial probability and initial population size . . . 54
4.4. Conclusion . . . 56

5. Population dynamics of mixed colicin E2 communities 57
5.1. Phenomenological model . . . 57
5.2. Mathematical model . . . 58
5.2.1. Master equations . . . 60
5.2.2. Extension to three strain interaction . . . 61
5.3. Numerical solution . . . 62
5.3.1. Stochastic lattice intitialization . . . 62
5.3.2. Stochastic lattice update . . . 63
5.3.3. Colicin field modelling . . . 64
5.3.4. Coarse graining . . . 65
5.3.5. Growth rate determination . . . 66
5.3.6. Parameter overview . . . 67
5.4. Simulation . . . 68
5.4.1. Competition dynamics . . . 68
5.5. Discussion . . . 69

6. Investigation of bacterial interactions: Competition by toxin production 71
6.1. Interaction scheme . . . 71
6.2. Competition Experiments . . . 72
6.2.1. Competition outcome . . . 73
6.3. Deterministic competition . . . 75
6.3.1. Experimental competition parameters: Growth rate and toxin producer fraction . . . 75

6.3.2. Simulation parameters: Switching rate, toxin sensitivity/effectivity, and growth rate . . . 77
6.3.3. Testing predictions: Alternative competition scenarios . . . 82
6.3.4. Conclusion of deterministic competition . . . 84
6.4. Stochasticity in positioning and toxin dynamics . . . 85
6.4.1. Stochasticity in positioning and phase 1 dynamics . . . 86
6.4.2. $N_{C,Edge}$ and deterministic competition parameters drive the population dynamics . . . 91
6.4.3. Statistical analysis of influencing factors . . . 92
6.5. Conclusion . . . 94

7. Investigation of bacterial interactions: Three-strain interaction 97
7.1. Interaction scenario . . . 98
7.2. Competition experiments . . . 99
7.2.1. Global competition outcome . . . 99
7.2.2. Computational outcome . . . 102
7.2.3. Alternative competition scenarios . . . 103
7.3. Early phase of interaction . . . 105
7.4. The importance of position . . . 109
7.4.1. Local analysis methods . . . 109
7.4.2. Local competition outcome . . . 111
7.4.3. Higher order interactions . . . 113
7.5. Conclusion . . . 116

8. Conclusion and outlook 119

A. Appendix for chapter 6 121
A.1. Experimental settings . . . 121
A.2. Strain growth rates . . . 122
A.3. Statistics for linear modeling of competition data . . . 122

B. Appendix for chapter 7 125
B.1. Experimental settings . . . 125
B.2. Strain growth rates . . . 126
B.3. Statistics for competition data . . . 126

List of publications 129

Bibliography 131

1. Introduction

Background: The mixed bacterial communities studied in this thesis are complex biological systems. As such, they contain a hierarchy of various physical scales and description levels in which collective phenomena emerge that impede naïve extrapolation between scales [1]. Similar emergent phenomena are known in physics [2–4] that traditionally tries to explain phenomena by their fundamental constituents and their interactions [5]. Consequently, in biophysics, one tries to understand the fundamental processes governing the biological phenomena in terms of a few simple principles using the tools from physics in manageable model systems [6–8].
Mixed bacterial communities studied here are comprised of single bacterial cells. Each of these cells is out of equilibrium because it takes up energy from its surrounding; stochasticity arises through noise in complex biochemical reaction networks (including gene regulatory networks); and cells interact either indirectly, e.g. via their influence on the environment, or directly, e.g. via secretion and sensing of molecules. Therefore, in the terms of physics, these systems could be described as stochastic non-equilibrium interacting many-particle systems [9–11].
In biology, one of the greatest challenges is to predict the emerging population dynamics that govern how the composition of a community evolves over time [12]. Understanding the underlying interaction mechanisms is thought to enable precise manipulation of host-associated microbiota for medical purposes in the future. Extensive research, both experimentally and theoretically, has shown how models for such interactions can be formulated from experimental data [13] and how interactions between microbes and with the environment influence the population dynamics [12].

The Colicin E2 model system: Colicin model systems have long been used to study the fundamental properties of microbial ecological competition [14] and typically consist of a toxin producing *Escherichia coli* (*E. coli*) strain that is mixed with toxin-sensitive and/or toxin-resistant *E. coli* strains.
In the simplest case, many individuals of the interacting species occupy the same habitat and spatial degrees of freedom can be neglected - conditions called *well-mixed*. Then, the population dynamics can be formulated in terms of ordinary differential equations and the long term state is determined by the fixed points of the system. Using the colicin system as a bacterial 'Rock-Paper-Scissor'-model in vitro [15] it was shown that under well-mixed conditions only a single strain could survive while the spatially extended

competition allowed coexistence. Consequently, well-mixed models of the population dynamics were replaced by spatially extended models. Using these models to investigate the interaction dynamics and its properties, such as coexistence or stability, revealed that the interactions allowed interesting spatio-temporal patterns to form [15, 16].
In addition to its role as a model system for microbial ecology, ColicinE2 expression is subject to phenotypic heterogeneity [17]. This phenotypic heterogeneity describes the presence of multiple phenotypes in isogenic populations [18] and arises through noisy gene expression in complex, often non-linear genetic circuits which creates multiple stable points in the high-dimensional phenotype space [19]. In ColicinE2 expression, only a subpopulation produces the toxin [17,20,21] and single cell fluorescence microsopy revealed that individual cells switch into the toxin producing state stochastically [20, 21]. Heterogeneity is crucial because toxin expression is accompanied by cell death of producing cells [22].
Phenotypic heterogeneity has gained increased attention in the last two decades due to the advancement of experimental techniques such as single-cell fluorescence microscopy [23, 24]. Furthermore, phenotypic heterogeneity is increasingly considered in computational models of the ecological competition [21, 25, 26]. However, most experimental studies on bacterial competition focused on macroscopic colony expansions, e.g. [15,25], and therefore did not investigate the relevance of a phenotypic substructure for competition. While the macroscopic limit and the concomitant mean-field approach is often a justified description level, it is well known that even for large cell numbers small fluctuations can lead to surprising phenomena such as population collapse [27].

Central questions of this thesis: Taken together, the influence of the phenotypic heterogeneity and the stochastic phenotype switching dynamics on the Colicin competition dynamics were largely unexplored prior to this thesis. In particular, the following questions were unanswered: Do stochastic effects in toxin production influence the competition dynamics and the competition outcome? Can one disentangle stochastic and deterministic effects of competition? Can one observe a transition from the random micro- to the deterministic macro-regime with increasing cell numbers? How does phenotypic structure of the C strain population influence the competition outcome? How is the competition altered if the third, resistant strain is added? How does the initial positioning influence the ensuing competition dynamics?
Having answers to these questions is important as it tests if the often proposed crucial stochasticity and heterogeneity is actually relevant in the context of bacterial competition [18]. Furthermore, it might help to choose appropriate description levels for the system of interest. Describing a system on the level of individuals, although it obeys average population behavior would be a waste of resources. On the other hand, *a priori* assuming average population behavior although fluctuations have a huge influence, can

be dramatic. For example, persister cells form a phenotypic subpopulation by stochastic phenotype switching and can lead to a relapse after antibiotic treatment [28].
Therefore, the main goal of this thesis was, first, to develop an experimental protocol that allows to study the interaction of mixed bacterial communities on multiple scales; starting from well-defined initial conditions near the single cell level to macroscopic bacterial colonies. Second, this protocol should then be applied to the ColicinE2 system to answer the questions above.

Outline of the thesis: In chapter 2, I complement the introductory background information given in this first chapter and revise core concepts needed to understand the work presented in this thesis. In particular, I discuss how a hierarchy of description levels arises naturally in mixed bacterial ecosystems. In chapter 3, I present the multi-scale experimental protocol that combines high precision nanoliter sample preparation and automated fluorescence time-lapse microscopy for the anaylsis of bacterial interactions. Then, I will derive the stochastic two-phenotype population dynamics within the pure colicin producer populations, show how stochasticity leads to large deviations from deterministic dynamics due to extinction, and derive a formula for the population survival probability (chapter 4). Afterwards, in chapter 5, I develop a theoretical model of the mixed-community competition dynamics, formulate the model in term of master equations, and describe how the system was solved numerically. Chapter 6 focuses on the two-strain competition of a toxin-producer and a toxin-sensitive strain. There, I will show how the combined effect of early stochastic toxin production dynamics and macroscopic division of labor gives rise to multi-stable competition outcomes. After that, in chapter 7, I present the study of an extended interaction system of three species (toxin-producer, toxin-sensitive and toxin-resistant). This investigation showed, how locally, the competition dynamics can differ significantly compared to the average global dynamics and how cheating as a higher-order interaction comes into play. Finally, chapter 8 concludes with discussing the results in a broader context and gives an outlook for further research directions.

Achievements: In conclusion, the main achievements of this thesis are two-fold. First, I developed a multi-scale experimental setup to investigate bacterial competition from the near single cell to the macroscopic level. Second, using this setup to investigate the Colicin E2 competition system, I could disentangle the stochastic and deterministic processes governing the competition dynamics and show for the first time experimentally that stochastic toxin production can induce competition outcome bistability. Prior to these efforts, the experimental verification of the importance of stochasticity in the context of bacterial competition was lacking.

2. Concepts - From molecules to ecology[1]

"All things are made of atoms, and [...] everything that living things do can be understood in terms of the jigglings and wigglings of atoms." [30]

Richard P. Feynman

The above citation reflects the reductionist view that, ultimately, every natural phenomenon can be explained by or *reduced to* its constituent parts; a view that wide spread in physics [5]. In turn, this view motivates an "upward causation" [31] in which macroscopic phenomena can be extrapolated from its microscopic constituents. Seemingly contradictory to that view, it is increasingly acknowledged that *emergent* system properties that cannot be naïvely extrapolated from its individual constituent parts [32] play an important role in both physical and biological phenomena [1–4, 31]. Examples of reducible and emergent phenomena from both physics and biology are illustrated in figure 2.1.

Although direct reduction to the microscopic components is not possible for emergent phenomena, the relevant information is nevertheless contained in the microscopic units and their interactions. Therefore, it is crucial to study complex systems, such as the bacterial competition systems investigated in this thesis, on various scales. Only investigating isolated microscopic units does not allow to observe the rich emerging properties while at the same time, only focusing on macroscopic observables prevents mechanistic insights.

In revising the most important concepts on which this thesis is based, I will show, how a hierarchy of description levels naturally arises for bacterial systems. This hierarchy includes gene regulatory networks, single cells, genetically identical populations, and emergent multi-cellular properties. After discussing this hierarchy for microbial systems in general, I focus on the colicin E2 system under investigation. In doing so, I will particularly focus on interactions between microbial (sub-) populations. Additionally, I will highlight studies to which I contributed but that were not the main focus of this thesis.

In addition to the colicin E2 system, I will present biofilm formation as an example for emergent properties in microbial systems.

[1]This chapter is largely based on publication [B2]. Images are partly reused and modified under Creative Commons License (CC BY 3.0). For more information see [29].

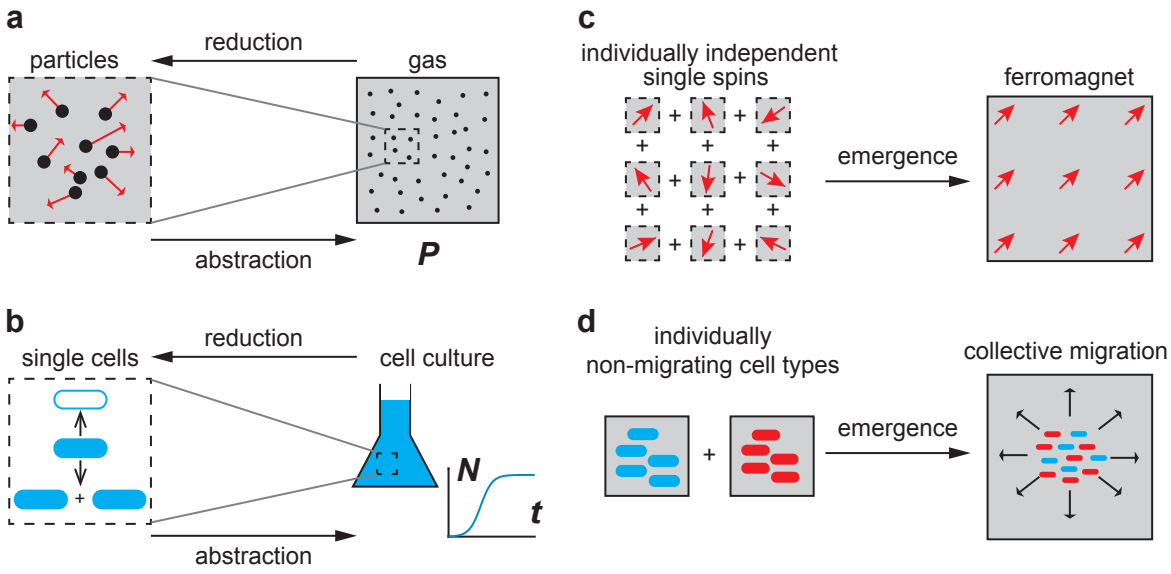

Figure 2.1.: Examples of reducible and emergent phenomena from physics and biology
a Physics: The macroscopic pressure of a gas can be reduced to collisions of individual microscopic particles with the container boundary. **b** Biology: Macroscopic cell culture growth can often be reduced to microscopic reactions of single cells, e.g. cell reproduction and cell death. These following examples illustrate emergent phenomena that cannot be predicted from the individual constituents. **c** Physics: If the temperature drops below a critical value, ferromagnetism emerges in a collective interaction of individually independent spins that usually should be able to freely rotate. **d** Biology: Individually non-migrating cell types can interact to collectively migrate [33, 34].

2.1. A hierarchy of description levels for bacterial systems

Complex bacterial systems can be understood using a hierarchy of physical description levels that includes (1) genetic networks, (2) single cells, (3) populations, and (4) emergent multi-cellular properties (Fig. 2.2).
In going from smaller to larger scales, many details can often be neglected, e.g. molecular details of the gene network can be averaged to an effective single cell response (reductionist view). However, in other cases, interactions of single cells on the population level give rise to qualitatively new emergent properties, such as biofilm formation [35] or collective motion [34] in multi-cellular communities.

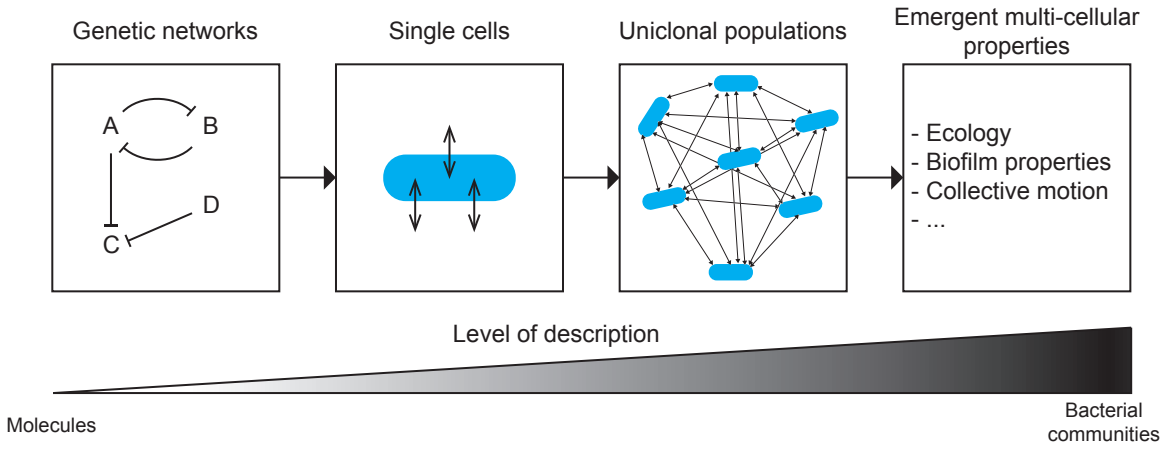

Figure 2.2.: A hierarchy of description levels in complex bacterial systems
Bacterial systems can be described using different levels of abstraction. Gene regulatory networks are the fundamental control of single cells, that aggregate to genetically identical populations. Individual cells of the same or of other (sub-)populations can interact giving rise to novel, emergent phenomena, such as biofilm formation [35] or collective motion [34].

2.1.1. Gene regulatory networks

Fundamentally, living organisms are controlled by the genetic program encoded on the DNA. According to the famous central dogma [36] the information of the DNA is converted into biochemically active proteins that constitute the cellular machinery. The classic model of transcriptional regulation considers operons consisting of regulatory regions and structural genes (see Fig. 2.3 a). A regulatory region comprises two kinds of domains, the promoter and the operator. The promoter is the binding sequence for the RNA polymerase that synthesizes the messenger RNA of the structural genes which will

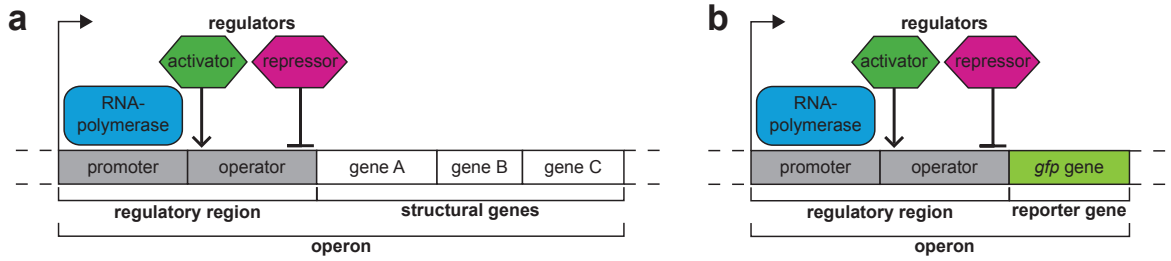

Figure 2.3.: Transcriptional regulation and reporter genes
a Operons are DNA sequences that consist of structural genes and the regulatory region to which regulatory proteins bind. These proteins regulate transcription of the structural genes into mRNA by the RNApolymerase. **b** Replacing the structural genes with a gene encoding a fluorescent protein allows to monitor its expression dynamics. Due to the same regulation, the dynamics of the reporter gene are expected to mirror the dynamics of the original structural genes.

then be translated into proteins [37]. Operators are binding sites for activating or repressing regulator proteins that can enhance or decrease the efficiency of the polymerase strongly. Cooperativity in regulator binding can thereby introduce complex nonlinear effects [38]. Regulator proteins themselves are regulated in a similar fashion giving rise to intricate interconnections. However, gene expression is regulated not only transcriptionally [37], but all along the protein synthesis pathway [39] which further increases the complexity.

Mathematical modelling

Collectively, the interconnected genes and regulatory proteins build large networks that can be modeled mathematically by differential equations [40]. In general, a vector of chemical species abundances $\mathbf{x}$ is modelled in terms of its biochemical reactions that can be described by non-linear functions $\mathbf{F}(\mathbf{x}, t)$ of the chemical species.

$$\frac{\mathrm{d}}{\mathrm{d}t}\mathbf{x} = \mathbf{F}(\mathbf{x}, t) \tag{2.1}$$

The complexity of these highly interconnected signaling pathways can give rise to emergent dynamical properties [41]. Despite this complexity, the relevant information is often only contained in sub-networks which justifies a modular analysis [42]. So-called network motifs, recurring interaction circuits from which the networks are built, are an useful concept that simplifies theoretical analysis and enables computational approaches [42–45]. Interestingly, even such small genetic circuits can contain rich dynamic behavior such as oscillations [46], multi-stability [47,48], and excitability [49] and

can be mathematically analyzed using methods from nonlinear dynamics.
In addition to nonlinearities of biochemical reactions and the inherent complexity of networks, noise in gene expression due to fluctuations in molecules numbers and stochasticity of biochemical reactions [50, 51] can lead to qualitatively different behavior in identical gene networks [48]. Consequently, in modeling the gene regulatory networks, this stochasticity has to be considered [7]. The temporal evolution of random state probability distributions can be described analytically using chemical master equations [52, 53]. Master equations are a versatile approach in the description of stochastic processes and can be applied to various levels of complexity (see equation 2.4). In this thesis, chemical master equations will be used to derive the stochastic population dynamics of colicin E2 producers (section 4). Often master equations can only be solved numerically using a stochastic simulation algorithm (SSA) such as the Gillespie algorithm [54].
In addition, gene regulatory networks can be extended using additional information, such as data on metabolic pathways [55], for example.

Experimental techniques

A large number of experimental techniques enables the modification of genetic sequences [56,57]. These techniques include but are not restricted to gene deletion (knock outs), gene insertion, and modification of individual bases and can be used to study the gene networks in vitro and in vivo [56]. A gene knockout denotes the deletion or otherwise inactivation of a certain gene and is used to study gene function [56]. Insertion of new genes is necessary to achieve new functionalities, such as antibiotic resistance for experimental selection or making an organism experimentally accessible. In particular, using the green fluorescent protein (GFP) and its derivatives [58,59] as reporter proteins enables to monitor protein expression dynamics in living cells. The idea is to insert the gene encoding a fluorescent protein into a genetic sequence that is subject to the same regulation as the functional protein that is to be monitored [60] (see Fig. 2.3 b). Consequently, expression of the reporter gene should reflect the expression of the monitored protein and can be measured using fluorescence microscopy [61]. Furthermore, sequence changes can alter the sequence-specific binding of DNA-binding molecules and thereby changes biochemical reaction rates [62].
These experimental investigation tools combined with theoretical modeling enabled the creation of synthetic regulatory motifs. The repressilator [46] and the genetic toggle switch [47] are beautiful examples for these efforts.

2.1.2. Single cells and phenotypic heterogeneity

At a the next level of abstraction, single cells and its machinery constitute the fundamental self-replicating units of living matter [56,63] that can be viewed as the hardware on which the DNA encoded instructions run. While this computerized view brings to mind deterministic input-output dependencies, phenotypes (cell states) can vary significantly between genetically identical cells [64] because of multi-stability in gene regulation, stochasticity in biochemical reactions, and other factors [26]. As a consequence, one can observe *phenotypic heterogeneity*, the presence of multiple phenotypes in populations of genetically identical cells under the same environmental conditions [18].
Phenotypic heterogeneity necessitates single cell experimental methods. In contrast to bulk methods, single cell methods unravel cell state distributions either in form of cross-sectional data or longitudinal data. Cross-sectional data, or cell state distribution snapshots, are commonly obtained by single cell 'omics' [65] or flow cytometry [66]. While these high-throughput methods generate huge sample sizes, their mechanistic insight is limited due to missing dynamical information of individual cells. Time-lapse methods, on the other hand, monitor individual cells to generate time traces (longitudinal data), mainly by single cell fluorescence microscopy [23, 24, 67].
It is suitable to think of a cell state as a point in a high dimensional space whose dimensions represent the concentrations of all outputs of the underlying gene regulatory network [19]. In the famous 'epigenetic landscape' abstraction, a potential landscape is assigned to these cell states with minima of the potential representing distinct cell fates [68]. Originally developed for differentiation in eukaryotes, generalizing this abstraction to various biological scales and incorporating stochasticity [69] it can be used to understand the discreteness of bacterial phenotypes as minima in the potential landscape. Additionally, it underlines emergent qualitative differences between phenotypes that cannot be linearly extrapolated from continuous cell state measures.

Illustrative example: the genetic toggle switch

Since phenotypic heterogeneity is an important concept in this study, its molecular origins are illustrated here with the genetic toggle switch. The genetic toggle switch [47] is a hallmark study in the understanding of genetic circuits and genetic bistability. Given two mutually repressing regulatory proteins i and j, of which one additionally controls a reporter gene, the dynamics were formulated for both i and j assuming cooperative repression and degradation of repressor molecules:

$$\partial_t x_i = \frac{\alpha_i}{1 + x_j^{\beta_i}} - x_i \tag{2.2}$$

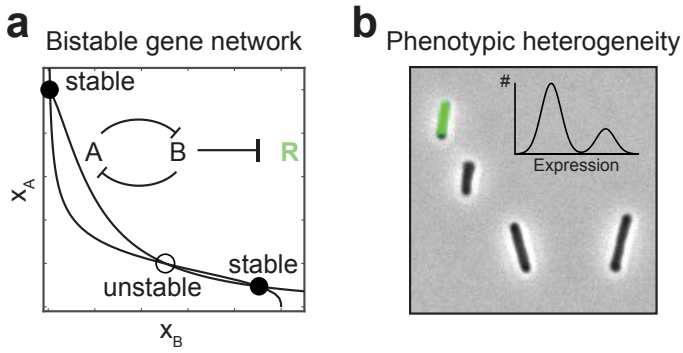

Figure 2.4.: Bistability in gene regulation leads to phenotypic heterogeneity
a Nullclines of genetic toggle switch dynamics (eq. 2.2) show two stable and one unstable fixpoint. Insert shows the mutually repressing scheme between repressors A and B and the reporter R. Figure reproduced from reference [47] with $\alpha_A = \alpha_B = 5$ and $\beta_A = 1.5$ and $\beta_B = 3$. **b** Phenotypic heterogeneity arises through simultaneous occupation of high and low expression states.

It is revealing to analyze the dynamics in terms of its fix-points that can be found by plotting the nullclines ($\partial_t x_i = 0$, $\partial_t x_j = 0$). Under the right choice of parameters α_i and β_i, the system exhibits bistability, i.e. two stable fix-points (high and low expression) that are separated by an unstable fix-point in between (see Fig. 2.4 a). Depending on the reaction parameters α_i and β_i stable and unstable fixpoint can be so close that fluctuations in gene expression can lead to the population of both states simultaneously, i.e. phenotypic heterogeneity (see Fig. 2.4 b).
While the genetic toggle switch is only one particular realization of bistable genetic networks, it nicely illustrates how non-linear coupled genes and gene expression noise lead to phenotypic heterogeneity. Section 2.2 discusses the phenotypically heterogeneous colicin E2 system which is controlled by the bistable SOS response system which carries a motif similar to the genetic toggle switch.

2.1.3. Emergent collective properties

In accumulations of cells, qualitatively new collective phenomena can emerge from the interactions of cells that can not be naïvely extrapolated from the individual behavior. This is true for populations of identical cells and even more so for (phenotypically) heterogeneous populations.
In homogeneous populations one way to organize collective behavior is via communication (see Fig. 2.5 a). This direct form of interaction is often realized by quorum sensing in which bacteria collectively monitor their environment to coordinate their behavior [70]. In general, communication via protein secretion and sensing enables versatile social behaviors [71].

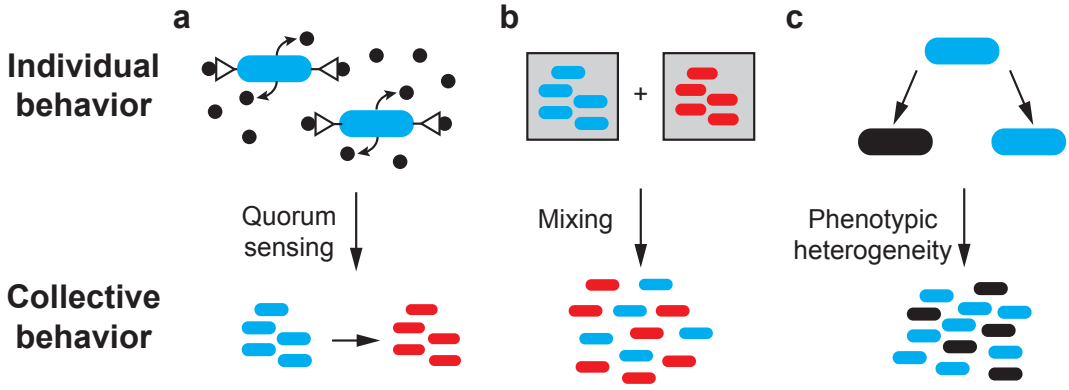

Figure 2.5.: Various forms of collective action in microbial systems
a Communication by quorum sensing allows coordination in homogeneous populations. **b** Mixing of genotypes can induce collective behavior. **c** In uniclonal populations similar behavior can be achieved by phenotyic heterogeneity.

In heterogeneous populations, either through mixing of different genotypes or by phenotypic heterogeneity (see Fig. 2.5 b & c), the cell collective can profit from the diverse functionalities that neither of the individual genotypes or phenotypes could achieve alone. In fact, in genetically identical populations phenotypic heterogeneity is the only way to achieve complex behavior such as division of labor or bet hedging [18, 72]. One of the most complex examples of collective microbial phenomena is biofilm formation in which motile, competent, sporulating, and biofilm matrix-producing phenotypes act collectively to achieve a primitive form of multi-cellularity [35, 73–76]. Section 2.4 discusses a recent study in which a phenomenological model is used to disentangle the influence of various biofilm building blocks.
Interestingly, while the stochastic decision for a phenotype is a single cell event and generally independent of all other cells [26], only on the population level bacteria can utilize the versatile behavior. The impact of most collective behaviors become only evident in competition with other populations within mixed communities or under certain environmental conditions. Thereby, the complex interactions between individual bacteria create effective fitness differences on the population level from which the community composition emerges [77, 78]. A general discussion of ecological interactions can be found in section 2.3. One particular form of direct ecological interactions, competition by bacterial toxin production, will be discussed in more detail in section 2.2.
Taken together, many microbial populations feature emergent collective behaviors that cannot be extrapolated from individually independent cells, but fundamentally originate from the underlying gene regulatory networks. As such, in investigating complex microbial systems, the relevant scales range from molecules to ecological interactions.

2.2. The colicin E2 system

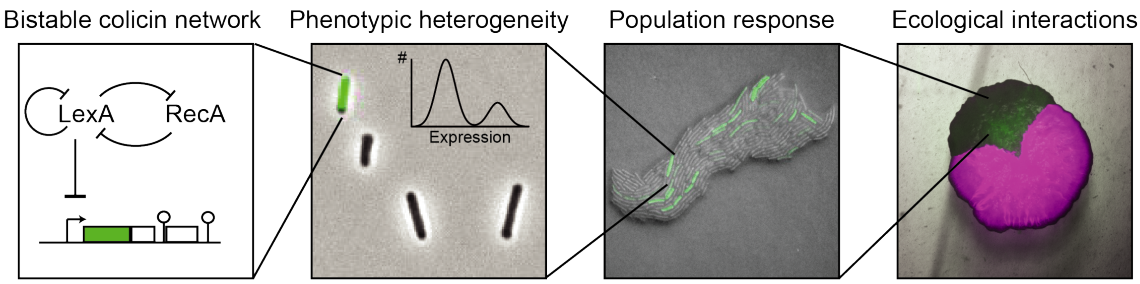

Figure 2.6.: A hierarchy of description levels in the colicin E2 system
The expression of colicin E2 is controlled by the stochastic, bistable SOS response system. This leads to phenotypic heterogeneity of reproducing and toxin producing cells whose toxin production can be visualized using fluorescence protein expression (green). On the population level, a balanced division of labor enables toxin production and secretion while being able to reproduce at the same time. Ecologically, this enables the colicin population to succeed in competition.

The bacteriocin colicin E2 is a bacterial toxin produced by some Escherichia coli strains to kill other bacteria in order to gain an ecological advantage in competition for resources [22]. In the spirit of the previous section, the colicin E2 system investigated in this thesis can be illustrated best using a hierarchy of description levels (see Fig. 2.6). The noisy and bistable SOS response system of E.coli controls the expression of colicin E2 transcriptionally [79, 80]. This bistability leads to phenotypic heterogeneity between single cells [81,82]. Depending on the external stressor that can tune the SOS response, the collective population response of to toxin production varies [83]. This population response then determines the ecological interaction with other population in mixed communities [84].
In the following, these aspects will be discussed in more detail.

2.2.1. Gene regulation of the colicin E2 operon

The colicin E2 system comprises three genes, *cea*, *cei* and *cel* that encode toxin, immunity and lysis proteins, respectively (see Fig. 2.7 a) [22] . Coexpression of *cea* and *cei* is imperative to ensure toxin-immunity protein complex formation that prevents Cea's DNA degrading activity [22,86] All three genes are encoded on plasmids, circular extrachromosomal DNA, and transcription is controlled via the SOS response system [22]. The SOS stress response system features two mutually inhibiting proteins LexA and

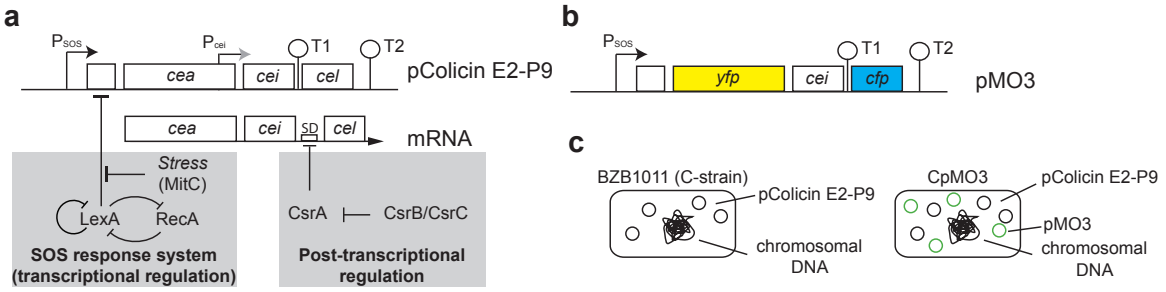

Figure 2.7.: Gene regulation of colicin E2 and reporter plasmid
a The colicin E2 system comprises three genes, *cea*, *cei* and *cel* that encode toxin, immunity and lysis proteins, repectively. Transcriptionally, these genes are controlled by the SOS response system, and translation of mRNA is post-transcriptionally regulated by the global regulator CsrA. **b** Genetic engineering yielded a reporter plasmid pMO3 in which *cea* and *cel* genes are replaced by genes encoding for yellow and cyan fluorescent proteins, respectively. **c** The original strain BZB1011 carries only the pColicin E2-P9 plasmid and the CpMO3 strain additionally carries the pMO3 plasmid. (Images are modified and reused from [20] under Creative Commons License (CC BY 4.0). For more information see [85].)

RecA, reminiscent of the genetic toggle switch. Ideally, in absence of stress, binding of the repressor LexA to the promotor sites represses transcription of genes under its control [81]. In case of DNA damage, RecA proteins are activated by single-stranded DNA and can cleave the LexA proteins bound to DNA [87] thereby initiating transcription. However, the SOS system is subject to gene expression noise which results in heterogeneous expression [81, 82]. Here, the heterogeneous expression serves an important biological function because *cel* gene expression leads to release of the Cea-Cei complex into the environment via cell lysis [88] and lysis causes the death of highly expressing cells [89]. Consequently, a population, in which all cells deterministically produce the toxin and lyse in doing so, dies out. While in absence of external stress, small fractions of the population produce the toxin due to noisy repression, the expression can be triggered by induction of DNA damage via antibiotic agents such as Mitomycin C (MitC) [83] or UV radiation [17].
In addition, the colicin E2 system features two more regulatory subtleties. First, due to two transcriptional terminators T1 and T2 (see Fig. 2.7 a), mRNAs of two different lengths are transcribed, a long mRNA containing all three genes and a short one lacking the lysis gene [79, 90]. However, this will be neglected for the remainder of this thesis. Second, translation of the *cel* gene transcript is repressed by binding of the global carbon storage regulator protein CsrA to the Shine-Dalgarno (SD) sequence [90]. After simulations predicted the ability of this post-transcriptional regulation to delay the time-point of *cel* [91], a combined experimental and theoretical study confirmed this prediction [92][2]. In particular, the study demonstrated how the timing of ColicinE2 re-

[2]The author contributed to this work listed in the publication list as [G1]

lease is controlled by CsrA sequestering nucleic acids, such as the CsrA binding sRNAs CsrB and CsrC [93] and single stranded DNA (ssDNA). Thereby, the study introduced ssDNA as a gene regulatory element [92].

2.2.2. Phenotypic heterogeneity in colicin production

Abstracting from the gene regulatory details, recent single cell studies analyzed the colicin expression dynamics via fluorescence time-lapse measurements using fluorescence reporter genes [20, 21, 81, 92].
In order to study the expression of *cea* and *cel* separately in individual cells, a reporter plasmid was genetically engineered in which both genes were replaced by genes encoding for yellow and cyan fluorescent proteins, respectively [20][3] (see Fig. 2.7 b). Transformation of the resulting reporter plasmid into the original colicin strain BZB1011 E2C [15] yielded the strain CpMO3 (see Fig. 2.7 c and section 3.2.1).
Single-cell time-lapse fluorescence microscopy of this strain revealed the dynamics of production and release [20]. In these phenotypically heterogeneous populations, individual cells exhibit generic fluorescence time-traces. Figure 2.8 a illustrates how a cell starts at a basal fluorescence level, then starts to produce the fluorescence protein, i.e. the toxin, until it reaches a maximum and drops abruptly due to cell lysis. In comparing many individual cell traces (Fig. 2.8 b), one sees that toxin production happens after a lag time over a broad time window. The lag time is due to a time delay between addition of the agent and actual induction of toxin production by external stress with MitomycinC. From the individual curves, one could obtain the distribution of switching time-points to the toxin producing state. Comparing the average and width of these switching time distributions revealed stress-dependent tunable response dynamics, ranging from basal expression to synchronized responses [20] (see Fig. 2.8 c). With synchronizing population behavior, the average fluorescence intensity shows increasingly peak-shaped behavior. In section 4.1.1, data from this study is reevaluated in order to formulate a stochastic model of the switching dynamics.
Furthermore, the genetically engineered pMO3 plasmid and modifications thereof were used to determine the gene expression noise in the colicin operon [94][4].
Studies of other groups relied on similar approaches and, among other things, explicitly quantified the role of autoinduction on the phenotypic heterogeneity [95] and stochastic state-switching between toxin production and reproduction [21].
A common feature of these studies on the phenotypic heterogeneity in the colicin E2 system is the binary classification of cells into producing and non-producing phenotypes

[3]The author contributed to this work listed in the publication list as [M1]
[4]The author contributed to this work listed in the publication list as [G2]

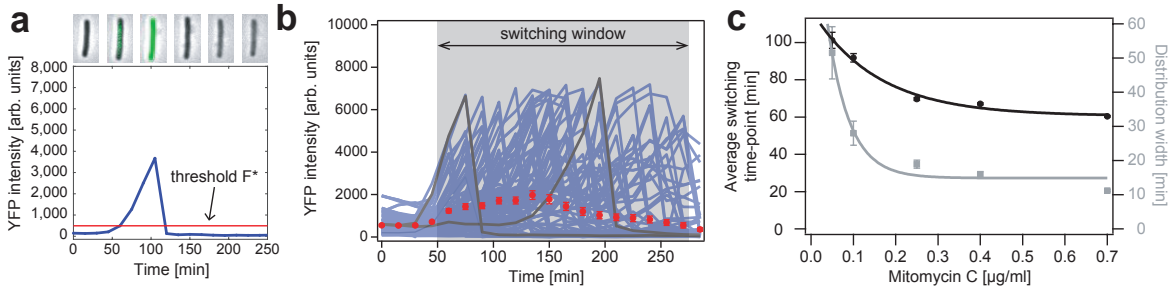

Figure 2.8.: ColicinE2 expression dynamics

a YFP fluorescence expression as a proxy for toxin expression increases over time, until it reaches a maximum and drops sharply due to cell lysis in the CpMO3 strain. **b** Multiple cell traces (blue lines, $N = 100$) reveal a broad temporal distribution of expression within the population at low external stress levels (0.05 μg/ml MitC). Individual cell traces (blue and two highlighted in black) are clearly different from the average population behavior (red). **c** With increasing inducer concentration, the distribution width (grey dots and fit) and average (black dots and fit) of switching time-points to the toxin producing state synchronize.

instead of continuous fluorescence intensity measures. This shifts the view away from the individual cell level to the population level.

2.2.3. Population level and emergent ecological properties

While originating from the structure of the gene regulatory network, only on the population level, the colicin population can profit from the phenotypic heterogeneity. Populations of neither pure toxin non-producers nor toxin producers could profit from both phenotypes. In addition, the strategy to produce toxin makes only sense in ecological competition with other populations.

Colicin model systems have long been used to study the fundamental properties of microbial ecological competition both experimentally and theoretically [14]. In particular, investigating two-strain interactions of toxin producer and toxin sensitive strains revealed frequency-dependent bistability of competition outcome in liquid habitats [96] and the role of habitat structure on coexistence of two strains [97]. The three-strain interactions of toxin producing, toxin sensitive, and toxin resistant strains have been used as a bacterial 'Rock-Paper-Scissor'-model in vitro [15], in vivo [98], and in silico [15, 16, 99] to probe the interaction dynamics and its properties, such as coexistence or stability. Furthermore, combined experimental and theoretical studies identified coexistence conditions that do not rely on cyclic dominance as in the classic Rock-Paper-Scissor game [25] and explicitly quantified the cheating effect of R on C [100].

While theoretical and computational studies often model the interaction at the microscopic scale, the role of phenotypic heterogeneity was only rarely taken into account.

Instead, the microscopic processes of toxin production, lysis, and toxin action on the recipient were only considered as effective macroscopic interaction parameters [99, 101] such as fitness costs, i.e growth rate reductions, and toxin effectivity parameters. Even when the phenotypic heterogeneity was explicitly considered [25], the influene of the degree of division of labor, i.e. the toxin producer fraction, on the competition was not assessed.

Open questions

Prior to this thesis, experimental studies mainly focussed on the macroscopic interactions and consequently neglected the influence of the microscopic population structure on the macroscopic competition dynamics. This motivated the development of an experimental approach to bridge the gap between micro an macro-scale. In this thesis, it was explicitly investigated how phenotypic diversity and stochasticity in phenotype switching influence the competition dynamics.

2.3. Bacterial interactions

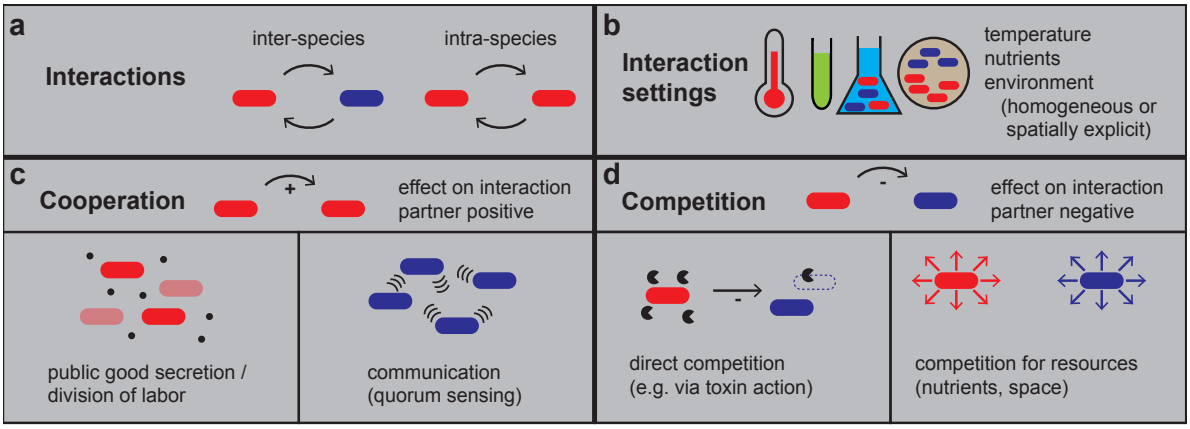

Figure 2.9.: Overview of microbial interaction mechanisms

a Interactions can occur between microbes from the same or from different species. **b** Interactions are strongly influenced by the settings in which the interactions occur. Interactions can be cooperative (**c**) or competitive (**d**) and are classified according to the effect on the interaction partner. Examples for both types are discussed in more detail in the main text.

As outlined above, many multi-cellular properties are only effective when interacting with other populations. In particular, toxin production as a strategy to kill competitors directly aims at influencing other bacteria. Therefore, this section reviews the basics of bacterial interactions and presents modelling approaches.

Individual bacteria interact either directly, e.g. via secretion and absorption of molecules, or indirectly by inducing a change that also influences the other bacteria, e.g. by consuming nutrients that are subsequently not available to the others [77]. Consequently, the composition of a microbial community arises through the interactions between the individuals and their environment [78]. Depending on the recipient of the interaction, interactions are denoted as inter- or intra-species interactions [77] (Fig. 2.9 a). Note that here, the term species does not necessarily signify a taxonomic type but depends on the description level, e.g. interactions between taxonomic sub-species.

In terms of evolutionary biology, the composition of competing traits is said to originate from fitness differences [102]. Consequently, ecological interactions can be characterized according to their effect on the fitness of the recipient [13, 77, 103–106]. Interactions that increase or decrease the recipients fitness are called cooperative (Fig. 2.9 b) or competitive (Fig. 2.9 d), respectively [12, 77, 107] and can be further classified [13, 108]. Competition and not cooperation has been proposed to dominate the interactions between microbial species [109] partially due to a negative effect of resource utilization on the interactions partner even in the absence of direct competition mechanisms.

The interactions are often mediated microscopically by secreted molecules, such as di-

gestive enzymes or toxins [14, 110, 111]. Irrespective of the impact on the recipient, the production and secretion of molecules itself is often accomplished cooperatively, e.g. by division of labor [112] or quorum sensing [113]. As such, the production and secretion of a molecules can carry characteristics of both intra-species cooperation and inter-species competition if the produced molecule benefits the producing population harming others. In order to model these interacting communities appropriately, it is important to take into account the interaction settings (see Fig. 2.9 b) and in particular the spatial structure of the environment. Depending on the scope and information available, the mathematical models used to describe the systems vary greatly. Unspecific generalized models [13, 114] can be used to make sense of large interaction system, such as the human microbiome, that feature a high number of interacting taxa. Here, experimental sequencing techniques offer a wealth of data, but the information on the specific interaction mechanisms and settings are sparse.
In contrast, in order to master the complexity, interacting bacterial systems are often studied in reduced well-defined experimental model systems [15, 25, 103, 115] or with the help of theoretical and computational modeling [12, 116]. In this thesis, a similar approach is taken by using a well-defined model system in which the most important dynamical parameters can be controlled.
In the following sections, the most common modelling approaches are discussed.

2.3.1. Well-mixed (non-spatial) systems

In well-mixed systems, the environment in which the interaction takes place is assumed to be homogeneous, such that the positions of individual bacteria do not matter and interactions occur between all individuals equally [117].

The Lotka Volterra equations - deterministic dynamics

In the limit of large bacteria numbers, stochastic fluctuations are negligible and one can formulate the population dynamics in terms of deterministic rate equations. A useful model to understand the dynamics of N interacting populations are the *Lotka-Volterra* equations (eq. 2.3) that model the abundance x of a (sub-) species i using ordinary differential equations (ODEs) involving growth processes with rate μ_i and interactions between (sub-) species i and j with an interaction parameter α_{ij} [118].

$$\partial_t x_i(t) = \mu_i \, x_i(t) + \sum_{j=1}^{N} \alpha_{ij} \, x_i(t) \, x_j(t) \tag{2.3}$$

The interaction parameter α_{ij} then classifies the interactions into cooperative ($\alpha_{ij} > 0$) or competitive ($\alpha_{ij} < 0$) neglecting microscopic details [114]. Later in this thesis (see chapter 4), an extended model is considered that additionally carries a conversion term from (sub-) species i to j with rate σ_{ij} such that $\sum_{j=1}^{N} (\sigma_{ji}\, x_j(t) - \sigma_{ij}\, x_i(t))$ is added to equation 2.3.
The benefit of the Lotka-Volterra model is its simplicity that abstracts details of billions of microscopic processes into a growth and an interaction parameter set. At the same time many important details are potentially omitted. While (sub-) species conversions, higher order interactions, and nonlinearities of the interaction terms could be added easily to obtain more generalized models [114, 119, 120], other properties of the system to be modeled are fundamentally incompatible, such as spatial degrees of freedom or stochasticity.

The master equation - Stochastic dynamics

In addition to the increased consideration of gene expression noise and the resulting phenotypic heterogeneity (see sections 2.1.1 & 2.1.2), the importance of stochastic effects in population dynamics have been reported mainly theoretically [26, 116, 117, 121]. Concrete experimental validation is sparse and mainly macroscopically motivated [115]. Systems in which stochastic fluctuations cannot be neglected are not appropriately described by the deterministic Lotka-Volterra dynamics. For example in cyclic rock-paper-scissor interactions, a finite numbers of agents renders the deterministically stable dynamics unstable leading to extinction of two out of three populations [121].
Originally developed for the description of chemical reactions, a versatile approach to describe stochastic processes is using the (chemical) master equation. The master equation describes the temporal evolution of state probability distributions. When using discrete states, the probability $P(n, t|n_0, t_0)$ to be in state n at time t conditioned on having been in state n_0 at t_0 evolves according to the processes leading into state n and out of it. The master equation is then composed of gain terms that lead from a state m into state n and loss terms that lead out of the state n to a state m [122]:

$$\partial_t P(n, t|n_0, t_0) = \sum_m \left[w_{nm}(t)\, P(m, t|n_0, t_0) - w_{mn}(t)\, P(n, t|n_0, t_0) \right] \tag{2.4}$$

Here, $w_{nm}(t) = w_{m\to n}(t) = \lim_{\delta t \to 0} \frac{1}{\delta t} P(n, t + \delta t|m, t)$ denotes the rate for the transition from state m to state n [122] and captures the dynamic properties of the underlying microscopic process. In many cases, master equations can only be solved numerically by using a stochastic simulation algorithm (SSA) such as the Gillespie algorithm [54].
In the context of bacterial interactions, the abstract state n could represent the com-

position vector $\mathbf{x}$ that contains the number of individuals of a given (sub-)species x_i as components and the transitions between neighboring states are due to the microscopic ecological processes such as growth, death, conversion, etc. In contrast to the macroscopic Lotka-Volterra equations, the individual interactions are not abstracted to an effective interaction parameter α_{ij} but instead are considered in terms of their impact on the state vector $\mathbf{x}$ via the transition rates $w_{nm}(t)$. In chapter 4, a stochastic population dynamics model is formulated in terms of its master equation and compared to the associated deterministic dynamics.

2.3.2. Spatially extended systems

Both modelling approaches presented so far (equations 2.3 & 2.4) lack any spatial degrees of freedom. This is problematic if one takes into account that spatially extended communities constitute the dominant lifestyle of bacteria [123]. And indeed, experimental studies showed that competition performed in liquid (well-mixed) conditions and spatially extended competition varied greatly [15, 124]. Consequently, various approaches have been developed to incorporate the spatial information.

Continuous space - Reaction-diffusion equations

Reaction-diffusion equations model the abundance fields $X_i(\mathbf{x})$ of a species i in terms of a interaction function f_i that depends on all abundances fields, signified by $\mathbf{X}$. Note, that the species i do not only represent species of bacteria but also of external concentration fields, e.g. nutrients or interaction mediating molecules, such as toxins [97]. Then, in general the equation reads:

$$\partial_t X_i = f_i(\mathbf{X}) + D_i \Delta X_i \tag{2.5}$$

Furthermore, such reaction-diffusion equation can be extended with noise terms ξ_i to incorporate stochasticity. Reaction-diffusion system have long been known to exhibit fascinating pattern forming properties [125–128]. A theoretical study showed the emergence of dynamic patterns in rock-paper-scissor systems motivated by bacterial systems [15, 16].

Discreteness of space and bacteria - individual-based models

Although stochasticity can be incorporated into the reaction diffusion by using noise terms, the individuality of bacteria cannot be modeled. To resolve this problem, individual-

based models are used [116]. In individual-based models the units considered are individual cells or coarse-grained cell clusters that interact with the other clusters and the environment according to the underlying biological processes. Individual-based models range from simplistic cellular automata on a lattice with deterministic update rules [118] to complex models that model individual cells in 3D space taking into account cell morphology [129], the intra-cellular metabolism and molecule secretion [130], and others details [116]. Nonetheless, even simple lattice models can be used to model biologically important processes such as spiral wave formation in amobae by use of a continuum signal molecule field [131]. Due to the broad range of model types, the nomenclature is ambiguous. Here, we use the term individual-based and agent-based model interchangeably.
Most individual based models can be mathematically described by a master equation in which the probability of an individual i to be in state n can be formulated analogously to equation 2.4. Omitting the conditionals for the sake of clarity one finds:

$$\partial_t P_i(n,t) = \sum_m \left[w_{nm}\, P_i(m,t) - w_{mn}\, P_i(n,t) \right] \tag{2.6}$$

In general, the expressions for the transition rates will be more complex containing additional factors that influence the underlying biological processes. Then the transition rates $w_{mn} = w_{mn}(\mathbf{x}_i, \mathbf{s}, \mathbf{c}, t)$ can depend on the position $\mathbf{x}_i$, the states of all other individuals s_j and all resources fields c_k of relevant resources r_k. Often, the individual-based models are set up on lattices. Then, the position $\mathbf{x}$ is not needed because a lattice site itself represents an individual. Furthermore, in many cases, the interactions between individuals are distance dependent such that only nearest neighbors are considered which reduces the number other individuals s_j to include.
In chapter 5, a stochastic lattice agent-based model is presented that uses a continuous toxin concentration field.

2.4. Biofilm formation in Bacillus subtilis[5]

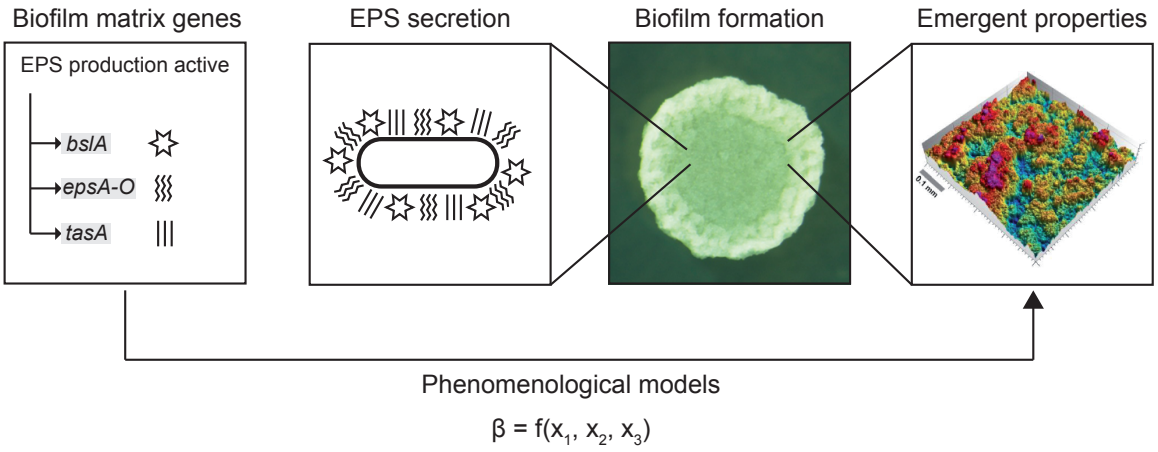

Figure 2.10.: A hierarchy of description levels for biofilm formation
Biofilm building bacteria produce and secrete exopolymeric substances (EPS) in which they embed themselves. The biofilm matrix typically induces a wrinkled colony morphology and gives rise to emergent properties, such as increased resistance against mechanical stress or chemical agents.

Bacterial biofilm formation is of great interest because it constitutes the dominant lifestyle of bacteria [123]. In biofilms, bacteria embed themselves in an extra-cellular matrix of exopolymeric substances such as proteins, polysaccharides, DNA, or lipids [35, 132, 133] to increase the communities' resistance to antibiotics and other chemicals [134–136], to protect themselves from high shear forces or other mechanical stresses [137, 138] and to resist invasion [139]. In addition to the production of these matrix building blocks and the embedding, a division of labor between various phenotypes including motile, competent, sporulating, and biofilm matrix producing ones has been shown to occur inside the biofilm [73, 74, 76].
One model system to study these biofilms is the Bacillus subtilis NCIB 3610 strain that produces three matrix building blocks; a surface layer protein BslA, a fiber protein TasA, and the exopolysaccharides EpsA [73, 76]. While the key biofilm matrix building blocks are known, an comprehensive understanding of how the macroscopic biofilm properties emerge from the specific molecules is still missing. Therefore, a phenomenological model was developed that used time-lapse data of the macroscopic biofilm properties area, height, and surface roughness of the wild-type strain and three knock-out mutant strains to quantify the effect of each biofilm building block on the respective macroscopic property.

[5]This section is largely based on the author's contribution to publication [K1].

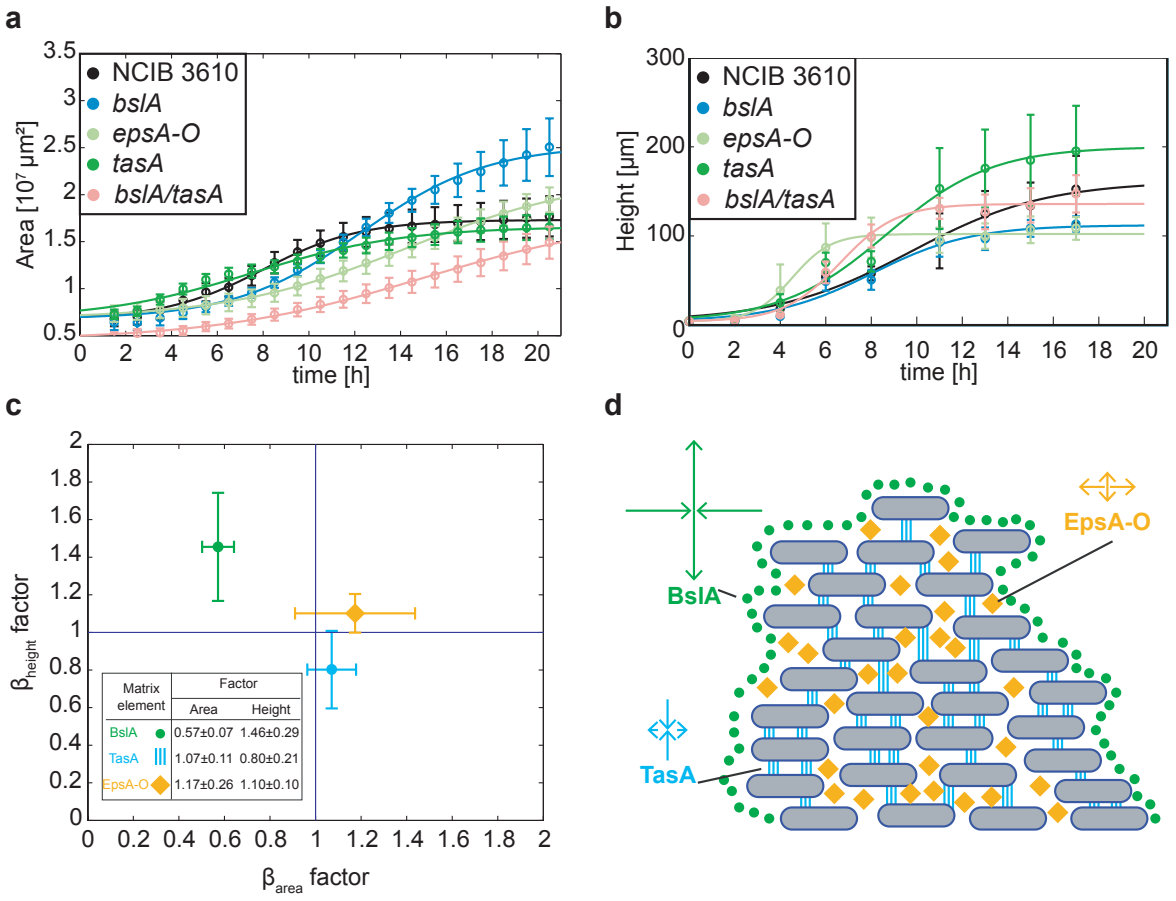

Figure 2.11.: Matrix building blocks influence biofilm properties

Biofilm area (**a**) and height (**b**) curves for different mutants and the wild type strain show changed growth characteristics for the various building blocks. **c** The individual building blocks can influence the biofilm properties positively ($\beta > 1$) or negatively ($\beta < 1$). **d** Comprehensive model illustrates function and contributions to height and area. Arrow lengths and directions indicate direction and strength of contributions β_i. (Images are partly reused and modified from [140] - published by The Royal Society of Chemistry under Creative Commons License 3.0 [29].)

The experimental data of all three properties exhibited sigmoidal behavior (data for colony area and height are shown in Fig. 2.11 a and b). Therefore, the data of each property P of strain $i \in \{\Delta bslA, \Delta epsA\text{-}O, \Delta tasA\}$ was fitted by the following sigmoidal logistic function:

$$P_i(t) = \frac{k_{P,i}\, P_{0,i}\, e^{r_{P,i}\, t}}{k_{P,i} + P_{0,i}\,(e^{r_{P,i}\, t} - 1)} + \overline{P_0} \tag{2.7}$$

Here, $\overline{P_0}$ is the average initial value for property P, $k_{P,i}$ the carrying capacity and $r_{P,i}$ the growth rate, and $P_{0,i}$ the value at $t = 0$. In order to assess the final macroscopic

quantity, the carrying capacity $k_{P,i}$ of the sigmoidal functions was further analysed. For the sake of simplicity, the index P is dropped in the following. Taking a multiplicative ansatz for the carrying capacity for each mutant, we generally find, using β_0 as the basal property value:

$$k_{\text{mutant}} = \beta_0 \cdot \prod_i \beta_i^{\delta_{\text{mutant},\,i}} \tag{2.8}$$

Multiplication by the contribution factors β_i for each of the building blocks i present in the considered mutant then allows to describe the carrying capacity. Note that a composition indicator $\delta_{\text{mutant},\,i}$ was used:

$$\delta_{\text{mutant},\,i} = \begin{cases} 1, & \text{if building block } i \text{ is present in the mutant} \\ 0, & \text{otherwise} \end{cases} \tag{2.9}$$

Inserting the building block contributions to the different mutants, one can explicitly write down a system of equations according to equation 2.8. Note, that expression of surface layer protein BslA depends on the expression of the *epsA-O* operon and therefore, the composition indicator $\delta_{\Delta epsA,\,i}$ was set to zero for both building blocks $i \in \{\text{EpsA, BslA}\}$ in the *epsA* knock out mutant.

$$\begin{aligned} k_{WT} &= \beta_0 \cdot \beta_{\text{BslA}} \cdot \beta_{\text{EpsA-O}} \cdot \beta_{\text{TasA}} \\ k_{\Delta tasA} &= \beta_0 \cdot \beta_{\text{BslA}} \cdot \beta_{\text{EpsA-O}} \cdot 1 \\ k_{\Delta bslA} &= \beta_0 \cdot 1 \cdot \beta_{\text{EpsA-O}} \cdot \beta_{\text{TasA}} \\ k_{\Delta epsA\text{-}O} &= \beta_0 \cdot 1 \cdot 1 \cdot \beta_{\text{TasA}} \end{aligned} \tag{2.10}$$

Extracting the values k_{mutant} from fitting equation 2.7 to the experimental data this system of equations can be used to determine the individual contributions β_i (see Fig. 2.11 c). One finds that the presence of specific building blocks can lead to an increase or decrease in the biofilm properties. The insert table in figure 2.11 c quantifies these contributions.
Disentangling the specific building block factors leads to a comprehensive model illustration (see Fig. 2.11 d). The illustration shows the composition of the biofilm and represents the contributions of the individual buiding blocks to the area (lateral expansion) and height (horizontal expansion) as arrows that show the direction (increase or decrease) and size of the effects. Furthermore, the quantified effects were used to predict the the carrying capacities for a double knock out mutant that missed both, *bslA* and *tasA* genes:

$$k_{\Delta bslA,\,\Delta tasA} = \beta_0 \cdot 1 \cdot \beta_{\text{EpsA-O}} \cdot 1 \tag{2.11}$$

Here a good agreement of the predicted and experimentally determined colony height (prediction: 134.60 μm, experiment: 131.88 μm) was found whereas the predicted colony area did not agree with experimental data (prediction: 17.72 mm^2, experiment: 13.85 mm^2). This might indicate non-linear cooperative effects that are not considered in the phenomenological model (equations 2.7 & 2.8).
Taken together, the phenomenological model allowed us to bridge the scale between micro- and macro level and to quantify the collective effect of the specific building block types. Using the obtained values to predict the properties of a double mutants was partly successful and indicates effects not considered here. However, the approach might be applicable to other bacterial systems.

3. Development of multi-scale fluorescence microscopy setup for automated long-term observation of bacterial interactions[1]

3.1. Motivation and problem definition

Interactions within macroscopic bacterial communities, ultimately originate from processes on the single cell level. Therefore, a comprehensive understanding of the processes on various scales is crucial. Previously, experimental approaches to study these interactions focussed on the microscopic or macroscopic level independently and often involved computational modelling to combine insights from both realms. Furthermore, community snapshot data obtained from microbiome studies, relates the microscopic composition revealed by sequencing to macroscopic desease phenotypes. However, it is hard to extract mechanistic insights therefrom.
Consequently, a novel experimental approach was needed that bridges the gap between microscopic and macroscopic scales and generates time-lapse data to gain causal insights. Since the smallest units of interest were single cells that are accessible with optical methods, a microscopy approach was favored. In particular, the following list of requirements was developed for this multi-scale setup.

1. **Multi-scale funtionality** The major requirement was to be able to following interacting communities from the well-defined microscopic single-cell level to macroscopic colonies.
2. **Fluorescence** In order to be able to analyze mixed communities composed of different bacteria, fluorescence labelling was a promising method to classify cells.
3. **Parallelization** In order to achieve statistical significance, the experiments should yield high replicate numbers.
4. **Long-term experiments** In order to follow the communities from single cell to macroscopic levels, experiments should at least be observable for 48 hours.
5. **Automation** Long-term experiments necessitate a high degree of automation to minimize experimenter interaction.

[1]Images are partly reused and modified from [141] published under creative commons license 4.0. [85]

6. **Constant conditions** Long-term experiments necessitate constant cultivating conditions for the sample.
7. **Sample preparation** The multi-scale nature of experiments prevents the exploitation of biological self organization for sample preparation. Therefore, novel approaches must be developed.
8. **Automated data analysis** Following data acquisition, the data must be analyzed for which a data analysis pipeline must be developed.

In the next section, I will discuss how the experimental approach developed for this thesis fullfils these requirements.

3.2. Experimental approach

Fig. 3.1 presents the general workflow of the experimental approach. First, liquid bacterial cultures are mixed at the desired strain ratios and densities. Using Acoustic Droplet Ejection (ADE) [142], small volumes of this mixed bacterial cultures can be transfered reliably to a solid agar growth medium in large one-well plates (Fig. 3.1 a). Then, the bacterial communities are imaged using a customized fluorescence microscope with zooming functionality. Constant cultivating conditions are ensured by a heating and humidifying box and a computer-controlled microscope stage enables observation of up to 80 communities in parallel (Fig. 3.1 b). Automated setup control and image acquisition includes zooming steps to accommodate for colony growth (Fig. 3.1 c). After acquisition, image processing includes segmentation and pixel classification based on fluorescence signals (Fig. 3.1 d). From these images, quantities such as relative and absolute population area are calculated and were subject to further data analysis.
In the following, I will discuss the components in more detail and how they fulfill the above mentioned requirements.

3.2.1. Bacterial culture

The culturing conditions and media are specific to the bacteria used. The following discussion is restricted to the colicin E2 system that was investigated during this thesis but can be generalized to other strains of bacteria.
The three colicin E2 strains C (BZB1011 E2C), R (BZB1011 E2R), and S (BZB1011) [15], have been supplied with fluorescence reporter plasmids that additionally carry an ampicillin resistance to allow differentiation and antibiotic selection. Table 3.1 contains an overview of the strains used.

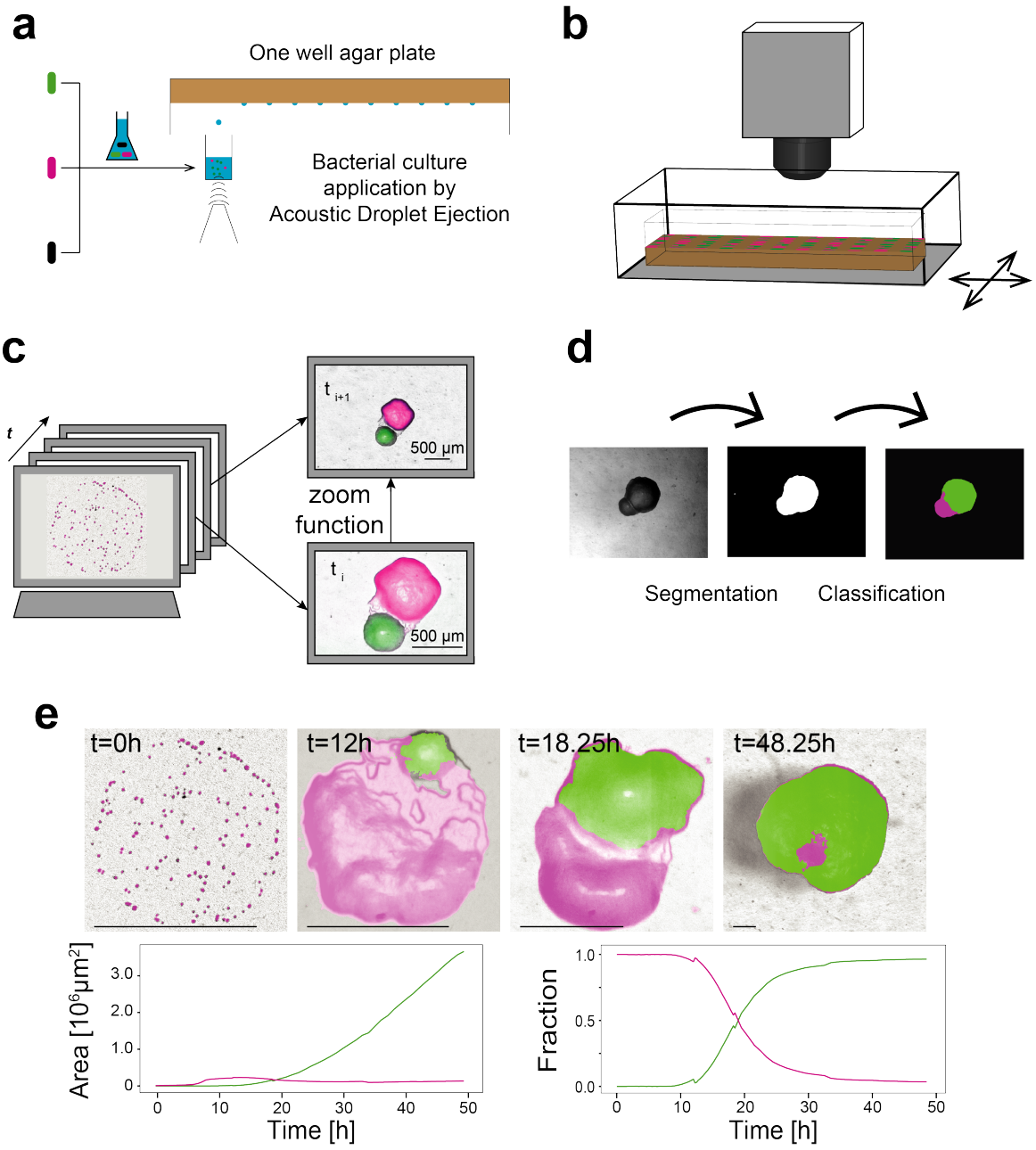

Figure 3.1.: Experimental approach overview

a Sample preparation uses transfer of nano liter volumes to an one-well plate (85.5 mm x 128 mm) via Acoustic Droplet Ejection (ADE). **b** This one-well plate is placed inside a heating and humidifying chamber to ensure constant cultivating conditions and is imaged using a fluorescence zooming microscope. **c** Computer controlled automated image acquisition includes zooming and enables long-term experiments. **d** Image processing performs fluorescence signal based pixel classification. **e** Example observation shows two competing populations (green and magenta) as an overlay of bright-field image and classification for four different time-points. Note, the zooming in-between images indicated by changes in scale bar length ($400\mu m$). Bottom row plots show absolute (left) and relative (right) area occupied by the respective populations derived from the pixel classification.

Strain	Description	Information	Reference
C_{pMO3}	C + pMO3	Colicin producing strain, carrying pColE2-P9 and the fluorescence reporter plasmid pMO3	[20]
S_{RFP}	S + pBAD24-mCherry	Colicin sensitive strain with arabinose inducible mCherry-fluorescence reporter plasmid	[25, 143]
R_{NFP}	R + pBAD24-nfp	Colicin resistant strain with ampicillin resistance plasmid	[25, 143]
S_{NFP}	S + pBAD24-nfp	Colicin sensitive strain with ampicillin resistance plasmid	[25, 143]
R_{RFP}	R + pBAD24-mCherry	Colicin resistant strain with arabinose inducible mCherry-fluorescence reporter plasmid	[25, 143]
S_{YFP}	S + pMO2	Colicin sensitive strain with pMO2 reporter plasmid	[20, 141]

Table 3.1.: Bacterial strains

Overview of bacterial strains used in this thesis with original reference.

Bacteria are stored in LB medium with 15% glycerol at -80°C. Cultivating plates containing LB with 1.5% agar are supplemented with $100\mu g/ml$ ampicillin and 0.2% arabinose.

Prior to competition experiments, cultures are separately grown in M63 minimal medium [144] with 0.5% glycerol, $100\mu g/ml$ ampicillin and 0.2% arabinose. Colonies for over night cultures are picked from cultivating plates and grown at 37°C and shaken at 300 rpm. In the morning, over night cultures are diluted to 0.1 OD_{600} and grown again to 0.2 OD_{600}. The C culture is then filtered by centrifugation with a 100-kDa filter in order to remove colicin molecules (62 kDa) and diluted to the desired density ρ (typically $\rho = 0.1\,OD_{600}$). Without centrifugation, the other cultures are diluted to a density ρ as well. Subsequently, the diluted cultures are mixed at the desired ratio $I_C : I_R : I_S$ (in case of three strains) and $40\mu l$ of this mixture are then transfered to the a source well on a 384-well poly-propylene plate used for sample preparation.

Experimental one-well plates for competition experiments contain the M63 minimal medium with 0.5% glycerol, $100\mu g/ml$ ampicillin and 0.2% arabinose and are supplemented with 1.5% agar. Additionally, the plates are supplemented with the SOS response inducing agent MitomycinC (MitC) at different concentrations $[MitC]$ (typically $[MitC] = 0.0, 0.005, 0.01, 0.1 \quad \mu g/ml$). Prior to transfer, experimental plates are warmed at 37°C to reduce transfer stress on the bacteria.

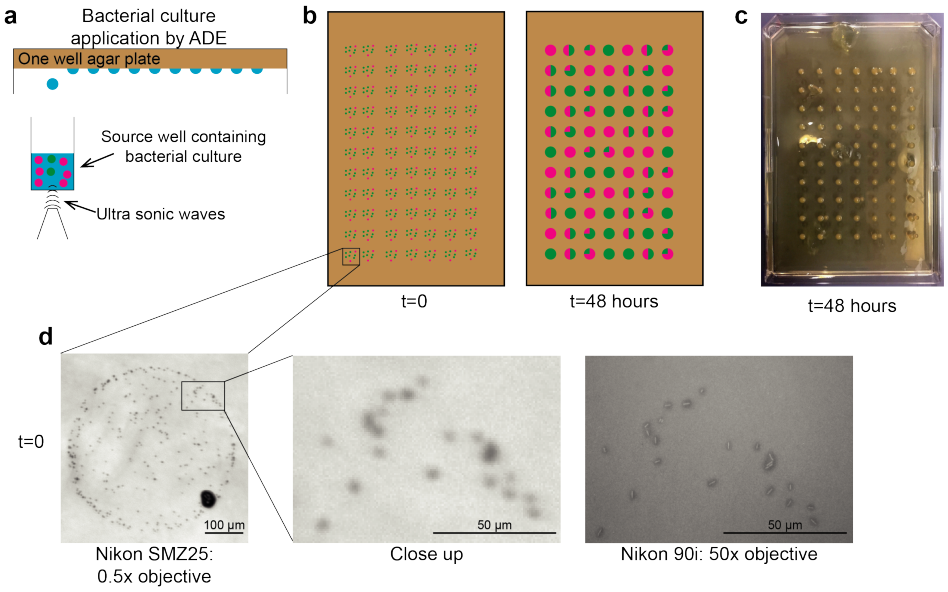

Figure 3.2.: Sample preparation
a Nano liter volumes are transferred to experimental agar plates by acoustic droplet ejection. **b** Transfer yields sparsely distributed initial communities that mature during competition. **c** Image shows an example experimental plate after competition. **d** Example initial community imaged in SMZ setup reveals near single cell resolution in comparison to high resolution microscopy (right image).

3.2.2. Sample preparation

After culture preparation, Acoustic Droplet Ejection (ADE) is used to transfer volumes V (typically $V = 2.5nl$) from the source well to the experimental plate. This ensures well-defined initial communities in an otherwise empty surrounding. Furthermore, the accuracy of the technique enables reproducible positioning of the initial communities which minimizes the time between transfer and experiment start. Figure 3.2 illustrates ADE technique and shows examples of an experimental plate after competition (Fig. 3.2 c) and of initial communities (Fig. 3.2 d).
In ADE droplets are formed by focusing acoustic energy into a well containing a liquid and it is commonly used in life science applications to transfer samples between multi-well plates [142]. In the experiments presented here, a Labcyte Echo 550 Liquid Handler was used.

The importance of the sample preparation technique cannot be overstated for these experiments. The multi-scale nature of experiments necessitates initial conditions at the single cell level. However, at the same time, the inoculum site of a community must be far away from the neighboring sites in order to allow expansion over the time-course of the experiment without influencing neighboring colonies. Consequently, the desired pattern features highly localized, fairly dense initial community sites in an otherwise

empty environment.
Micro-patterning techniques have been proven useful in creating micro-structured environments [145], in which eukaryotic cells self-organize to adhesion sites [146] and can be investigated using microscopy techniques. However, such approaches are not suitable for our purposes because the use of adhesion sites would confine the expansion or would not ensure empty surroundings. Similarly, for prokaryotic systems, fixation techniques include attachment of cells to coated microfluidic channels [147] or agarose pads [24]. However, these techniques are not suitable because such methods yield fairly homogeneous occupation.

3.2.3. Experimental setup

After sample preparation, the experimental plate is placed inside the experimenal setup (see Fig. 3.3 a). The main component, the Nikon SMZ 25 stereoscopic fluorescence microscope, was assembled on a Newport Isostation table with a custom-built mount. Images were acquired by a Nikon Qi1 CCD camera with a Nikon DS-U3 camera controller.
The first crucial feature of this microscope is its zooming functionality. This is achieved by placing a zoom unit between the objective and the beam splitter / filter block [148]. In general, a zoom unit consists of fixed and movable optical elements that change the size of a surpassing beam and thereby the magnification while not focussing the light. For illustration, a simple system of two converging lenses L_1 and L_3 with a diverging lens L_2 in between is discussed in the following. While L_3 facing the objective stays fixed, the other two lenses can be moved along the optical axis. By changing the position relative to each other and to L_3, the magnification is changed. Figure 3.3 b shows a scheme of such a zoom system for two different magnification values. A 25-fold change in magnification (0.63x - 15.75x) enables the automated multi-scale analysis from near single-cell to macroscopic levels without changing the objective. Figure 3.2 d compares images of single cells obtained with maximum magnification using a 0.5x objective in comparison to an conventional upright microscope with fixed magnification.
In order to differentiate different strains of bacteria, the setup is equipped with the suitable excitation and emission filter components. In particular, Nikon P2-EFL GFP-B and P2-EFL RFP-L filter blocks are employed for fluorescence excitation and emission filtering, and a customized OG-570 long pass filter is used to reduce phototoxicity from bright-field illumination. A Lumencor Sola SE II LED lamp provides the light for bright-field illumination and fluorescence excitation.
A Märzhäuser SCAN 130 x 85 scanning stage controlled via a Märzhäuser TANGO 2 controller facilitated the parallel observation of multiple communities on one-well agar

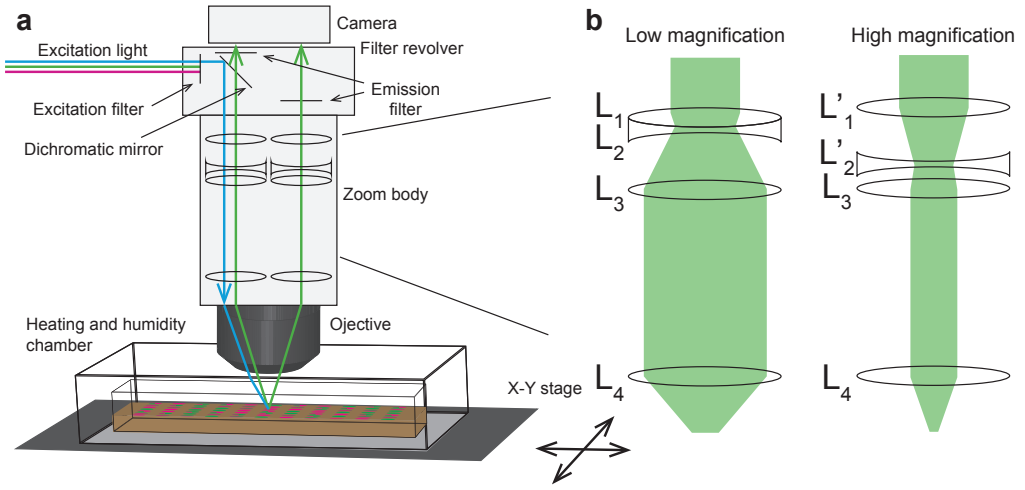

Figure 3.3.: Experimental setup and zoom ray optics

a A schematic illustration of the experimental setup depicts important parts of the microscope during fluorescence measurements. In the filter block, excitation light is filtered for the right wavelengths, guided through the zoom body and objective to the sample within the sample chamber (blue). Emitted fluorescence light is then guided through the objective, the zoom body and the emission filters to the CCD camera (green). **b** An example afocal zoom system is depicted for two magnification values. Depending on the positions of L_1 and L_2 the magnification is changed, while L_3 is fixed. The illustration is based on ray optics simulations [149] with the following values (arb. units), $f_1 = f_1' = f_3 = f_3' = 200$, $f_2 = f_2' = -70$, $f_4 = f_4' = 100$, $\overline{L_1L_2} = 10$, $\overline{L_2L_3} = 90$, $\overline{L_1'L_2'} = 80$, $\overline{L_2'L_3} = 32$.

plates.

Microscope, camera, scanning stage, and LED lamp are controlled by a computer running the Nikon NIS-Elements AR 4.30.01 64-bit software with the required plug-ins. This computerized control enables fully automated image acquisition.

Finally, a gas incubation and heating system for multi-well plates (Ibidi) ensured constant environmental conditions (37°C and 80% humidity) to enable long-term observations and was customized to incorporate one-well plates.

Taken together, the individual components of the setup fulfill the requirements formulated above and constitute a multi-scale investigation approach for bacterial interaction systems.

3.2.4. Automated image acquisition

Throughout the time-course of the experiment, images are taken with a time resolution Δt in the bright-field, RFP and GFP channels at every saved position. Finding and saving the positions can be tedious and is a critical step in the experiment. To minimize search time, the accurate positioning of initial communities by the ADE protocol

is essential. However, even with this accurate droplet application, precise positioning of the sample plate into the setup is crucial in order to bring the positions close to the pre-saved positions of earlier experiments.
During the experiment, the computer-controlled zoom accounts for the colony expansion. The use of multiple zoom levels, creates the need to convert pixel sizes into metric spatial measure. Sampling different magnification-pixelsize value pairs using the built-in conversion tool, an explicit conversion formula was derived by fitting (see Fig. 3.4 a):

$$l_{\mu\mathrm{m}} = \frac{6.45}{\mathrm{Zoom} \cdot \mathrm{Objective}} l_{\mathrm{pixel}} \tag{3.1}$$

Knowing the dimension of the field of view for every magnification allows to customize the imaging to account for the specific growth rates. Figure 3.4 b illustrates the division of an experimental time-course in four distinct zoom regimes with changed magnification that accounts for the colony growth.

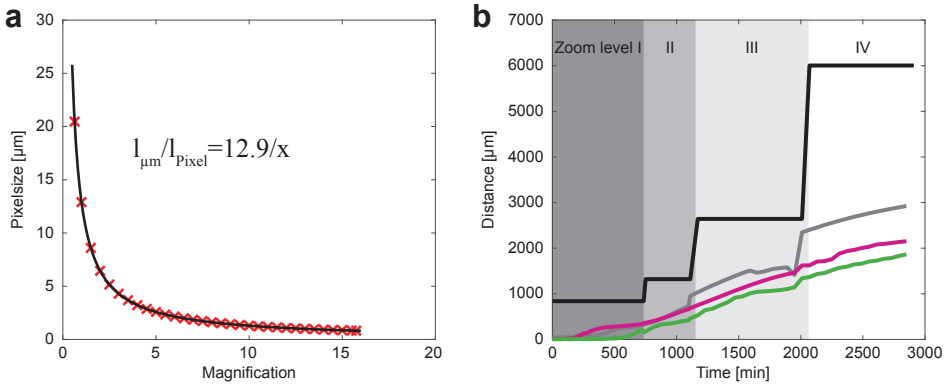

Figure 3.4.: Zoom levels

a Using the 0.5x objective, various magnification-pixelsize value pairs (red crosses) were sampled and fitted using the formula $f(x) = 12.9/x$ (black line) that agrees perfectly with the data (goodness of fit $R^2 = 1$). **b** In order to follow the colony expansion, zooming occurs during the time-course of the experiment. Here, a 48 hour measurement is divided into four distinct zoom regimes (maginfication = 15.75x, 10x, 5x, and 2.2x). The black line indicates the vertical size of the field of view within a zoom regime, and the three lines represent average radii r of growing colonies (calculated by $r = \sqrt{A/\pi}$). While two curves (magenta and green) are well captured by the zooming, the grey curve flattens when nearing a zoom level change, indicating growth out of the field of view.

In addition to the change in magnification, the processes within the observed community might induces changes over the time-course of the experiment that require altered image acquisition settings, such as illumination intensity or exposure time. Particularly

	Zoom Level			
Experimental Parameter	**1**	**2**	**3**	**4**
Magnification	15.75	10	5	2.2
$T_{Start}[h:min]$	00:00	12:15	18:30	33:30
Δt[min]	15	15	60	60
Pixel size [μm]	0.819	1.29	2.58	5.86
Bright field intensity [%]	9	5	5	5
Bright field signal gain	1	1	1	1
Bright field exposure time [ms]	7.3	5	2.1	1.9
RFP excitation intensity [%]	100	100	100	100
RFP signal gain	46	9.6	1	1
RFP exposure time [ms]	2000	2000	2000	1000
GFP excitation intensity [%]	100	100	100	100
GFP signal gain	46	9.6	1	1
GFP exposure time [ms]	2000	2000	2000	1000

Table 3.2.: Microscope configuration settings
Overview of microscope configuration and image acquisition settings for two-strain interaction (chapter 6).

demanding is the tuning of fluorescence excitation and exposure time. For example, in transitioning from single cells to macroscopic colonies, the absorption of excitation light is strongly increased and the resulting emitted fluorescence light can easily lead to over-saturation. Consequently, not only the magnification but the whole microscope configuration is changed multiple times during image acquisition which makes later analysis even more complex.
Typically, experiments for this thesis were divided into four distinct zoom regimes. The set of microscope configurations was kept constant for the different experiments. The individual settings for each zoom level were determined iteratively in test experiments. Table 3.2 contains the microscope configurations used in the two-strain competitions presented in chapter 6.

3.3. Data analysis

In order to gain insights from the acquired data, the raw data must be processed and key measures quantified, i.e. images have to be turned into numbers. Furthermore, these numbers have to be related to each other statistically.
This general procedure applies for a variety of systems but must be adjusted to the individual system under investigation and the questions asked. In the following, I discuss the analysis pipeline for the competition experiments presented in this thesis (chapters 6 & 7).

3.3.1. Image analysis

The outputs of long-term competition experiments are large image stacks, in which 1024x1280 pixels 12-bit images for every channel (bright field, RFP, and GFP), for every time-point, and for every position are saved. A typical experiment with 77 positions imaged over 108 time-points measures over 62 giga byte in file size. The raw output files of the image acquisition are single Nikon specific *.nd2-files containing all the data. While the accumulation of data in single files is simple, the large file size prevents loading of these files for data processing. Therefore, the large files are split into handleable stacks that contain only information for one specific position and were compressed to 8-bit.
As outlined above (see section 3.2.4), varying image acquisition settings and changes in colony structure and composition during the experiment alter the signal structure. Consequently, the image processing has to be customized for the various zoom levels and the different competition outcomes to account for the signal characteristics.
A consequence of this adjustment is that in the following the image processing will be discussed in general and the actual operation parameters are given later for every condition.

Pre-processing

Experiments were manually screened in order to identify erroneous spots which were excluded from further processing. One reason for exclusion were sample preparation errors (spotting errors) in which the droplet volume applied to the sample was too high or droplets dispersed during ejection and created misshaped initial communities. A second reason for exclusion was the missing of an interacting strain since, at low volumes and small strain ratios, initial communities could be missing a strain completely just by chance.
However collecting information on the competition outcome was a seond reason for screening the experiments. Due to the change of signal characteristics with colony composition, the two-strain competition experiments presented later (chapter 6) were pre-screened in order to get a rough estimate of the final colony composition. This was necessary because the green fluorescence signal was favored compared to the red signal and favoring the green signal without having any green cells present lead to wrong classifications.
Favoring the green signal was unavoidable because the fluorescence intensity between the two strains varied strongly due to different expression characteristics. While the S strain produced the red fluorescing protein continuously, the C strain produced the yellow fluorescing protein only when toxin production in a given cell was activated

resulting in much lower average fluorescence values. In plain words: If there is no green fluorescing strain present, the algorithm does not have to look for it.
Since the three-strain experiments featured red, green, and no fluorescing strains, the artificial signal boosting of the green signal was omitted and the screened outcome information was not needed.

Image processing

Typically, the image processing involves two main steps, image segmentation and pixel classification. By segmenting the image, the algorithm decides which pixel belongs to the bacterial colony and which pixel is a background pixel. In classification, the algorithm uses the fluorescence signal to classify the pixels into different bacterial types, e.g. C and S strain.

Segmentation Mathematically speaking, grey scale images can be presented as matrices $G \in \mathbb{S}^{m\times n}$ where m and n are the number of rows and columns in the image and $\mathbb{S}$ is the set of intensities available at a given bit depth. For 8-bit images one finds $\mathbb{S} = \{0, ..., 2^8 - 1\} = \{0, ..., 255\}$. Segmentation now aims to binarize the image into a matrix $B \in \{0, 1\}^{m\times n}$ where the pixel equaling 1 represent pixels of the bacterial colony and zero pixels represent the background.
The segmentation process typically involves complex manipulation of the matrix G. Since the mathematically explicit formulation is not instructive, I discuss the operations only schematically (see Fig. 3.5). First, the image is inverted and background corrected by subtracting the image from a smoothed background image of the specific position acquired at the same magnification prior to the actual experiment. Second, the resulting image is gamma and noise corrected using different filters. After noise reduction, the image is segmented into background and bacteria pixels using intensity based thresholding according to the Otsu [150] or Kittler-Illingworth [151] methods. Intensity based thresholding binarizes the processed grey scale images G' according to an intensity threshold τ:

$$B_{ij} = \begin{cases} 1, & \text{if } G'_{ij} \geq \tau \\ 0, & \text{otherwise} \end{cases} \tag{3.2}$$

At high magnification, when colonies feature inhomogeneous shapes, these intensity based methods are supplemented with edge detection (Canny algorithm [152]). These segmented images are subject to morphological operations such as hole filling to yield the final segmentation B_{BF}.

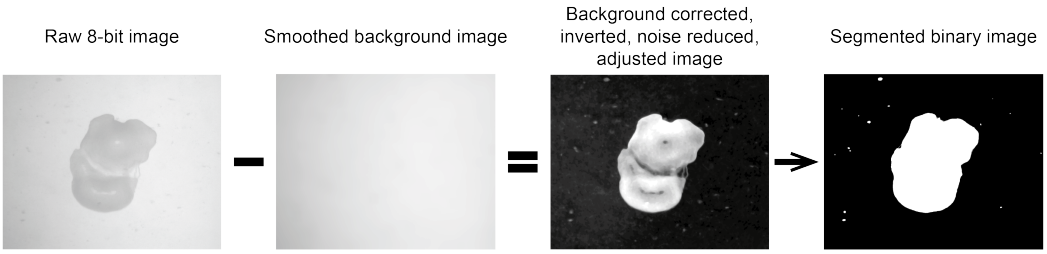

Figure 3.5.: Bright field segmentation scheme
The original 8-bit image is background corrected and inverted using a smoothed background image of the position acquired prior to experiment. The resulting image is filtered for noise reduction and gamma corrected before segmentation using intensity based thresholding.

Classification Similar to the bright field segmentation, the pixel classification procedure includes background correction and segmentation steps (see Fig. 3.6) but is less general compared to the bright field segmentation procedure presented above due to different fluorescence properties of the strains investigated. In the following, I will outline the classification procedure used for the two strain interactions (chapter 6) and point out at when it differed from the procedure used for the three strain interaction (chapter 7).
In accordance to the bright field segmentation, images are background corrected using smoothed background images. Only for the two-strain experiments, noise reduction and autofluorescence corrections by subtraction of the median fluorescence value followed. Again similar for both datasets, fluorescence images were restricted to the segmented bright field area and pixels were segmented into fluorescent or non-fluorescent pixels yielding the binarized images B_{RFP} and B_{GFP}. In case a pixel was positively segmented in both fluorescence channels, a decision rule was implemented to uniquely classify a given pixel into RFP or GFP, in the two-strain experiments, such that $B_{RFP,ij} + B_{GFP,ij} \leq 1, \quad \forall(i,j)$.

For the three strain experiments, pixels of the colony could also be of type non-fluorescent. This complicated the classification. In particular, no decision rule was implemented and pixels could be of type, RFP, GFP, non-fluorescent and RFP&GFP.

Area calculation After image segmentation and pixel classification, the total areas and the areas of the individual fluorescence channels were calculated by summing up all pixels of the respective binary images. Here, A_T denotes the area of type $T \in$ {BF, RFP, GFP}

$$A_T = \sum_{i,j}^{m,n} B_{T,ij} \tag{3.3}$$

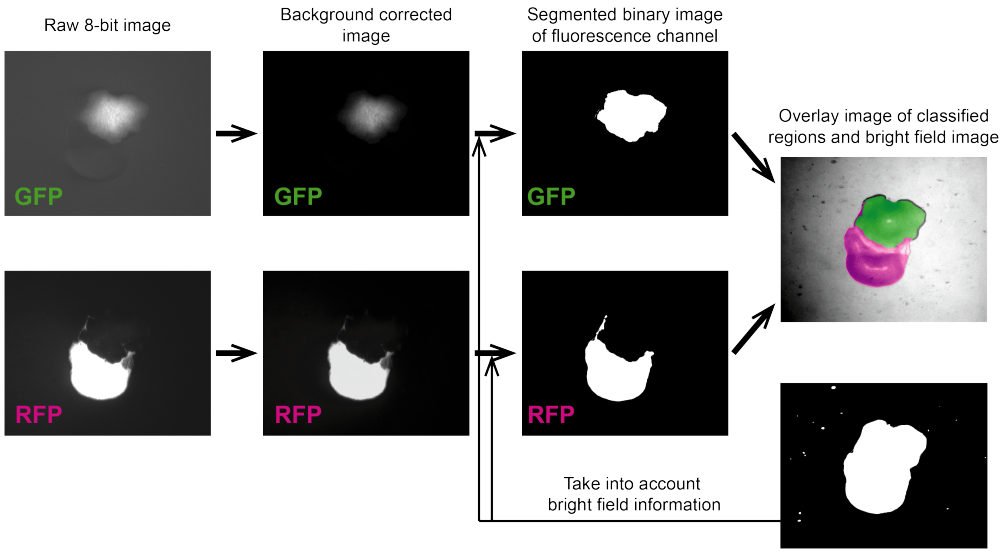

Figure 3.6.: Fluorescence classification scheme
Pixel classification example from two-strain competition. The raw 8-bit images are background corrected like the bright field background correction (see Fig. 3.5). It is evident, that the signal-to-noise ratio of the GFP channel is markedly weaker that for the RFP channel (left images). Therefore, information on the bright-field segmentation is used to aid in the binary segmentation of the fluorescence signals (pixel classification). Overlay shows bright-field image and fluorescence classification.

With the square of the pixel area conversion factor (eq. 3.1), the areas could be converted into metric values. Note, in case of RFP-GFP double classification in the three-strain experiments, these pixel were counted only half to each of the areas to conserve the total area.

Post processing

Despite the intricate adjustment of image processing parameters, mis-segmentations and mis-classifications occurred. In order to remove singular erroneous data points, the resulting area and relative area data curves were screened. Data points were removed if they qualitatively changed the outcome. An example is given in Figure 3.7.

3.3.2. Detail analysis

In addition to the automated image analysis discussed above, the initial phase of experiments was more thoroughly investigated by computer-aided manual inspection. Manual inspection was necessary because missing or only very weak single-cell fluorescence of C cells at early time-points of the experiments prevented automatic detection. This was

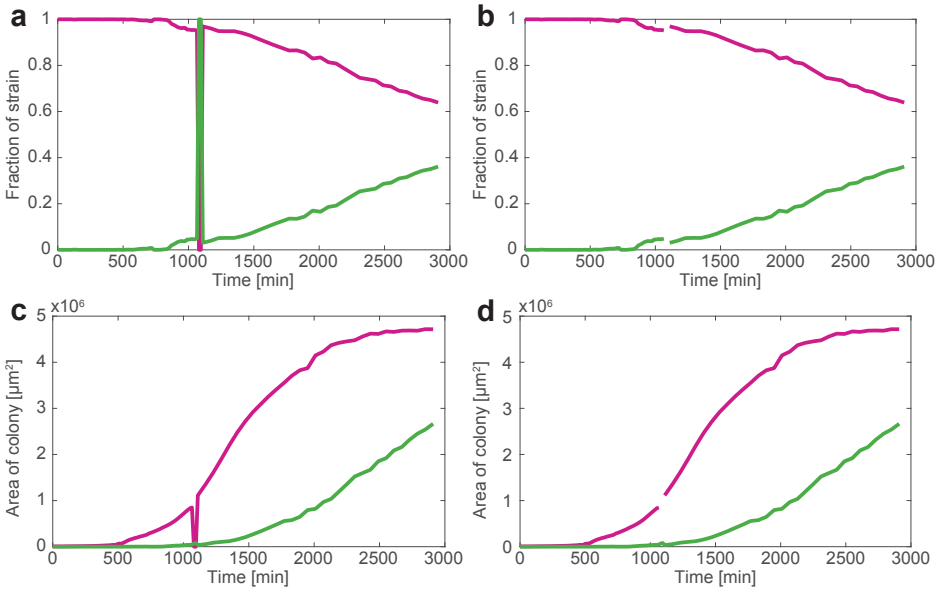

Figure 3.7.: Post-processing example
Exemplary time-traces of S (magenta) and C (green) area show that the mis-processing of an individual frame of the colony time-lapse (**b**) completely changed the qualitative behavior of the relative area $\frac{A_C}{A_C+A_S}$ (**a**). Therefore, the individual data points were removed. The resulting post-processed traces for relative (**b**) and total area (**d**) are shown on the right.

especially problematic in using C and non-fluorescing R cells together as they could not be clearly distinguished in the beginning. Typically, the detail analysis includes locating C cells or clusters, indicating their fate (reproduction or early lysis), and whether they evolved into a large C cluster that has access to the colony edge at later time-points.
In case of three strain experiments, a similar characterization was performed for the R cells. Additionally, a localized analysis after 48 hours was performed based on the early phase positions determined in the detail analysis.
The specifics of the details analysis will be discussed in the respective results chapters (see sections 6.4.1 and 7.4.1).

3.3.3. Data processing

Image analysis yielded time series data of absolute $A_T(t)$ and relative area $A_T(t)/\sum_i A_i(t)$ for a considered type T, at the different positions, under various experimental conditions. In addition, the data is supplemented with detailed information on the community composition at early time points.
Taken together, these data that can be aggregated into a high dimensional data set that is subject to further statistical analysis which will be specifically discussed in the respective results chapters.

3.4. Additional applications

In addition to the colicin E2 competition presented in this thesis, the setup has been used for various applications with other gram negative bacteria (*Pseudomonas aeruginosa*) and gram postive bacteria (*Bacillus subtilis*).
Of these other applications, I will only briefly discuss two as a proof of concept, biofilm cooperation in *Bacillus subtilis* and antibiotic resistance screening.

3.4.1. Biofilm cooperation

Biofilm formation relies on the cooperative production and secretion of extracellular matrix components [35]. A long-standing question in the field of biofilm formation was whether knock-out mutants that each miss a certain gene for the expression of a matrix component could cooperate to reconstitute wild-type behaviour in mixed communities. In order to investigate the potential cooperation, mixtures of fluorescently labeled knock-out mutants that each miss one matrix building block gene were investigated using the presented setup. Analysis of communities after 24 hours revealed an fitness increase measured in total colony area of mixed communities compared to the pure (unmixed) knock-out mutant colonies.
Despite the promising preliminary results, the project was discontinued as soon as we gained knowledge that a similar study was about to be published investigating the same question, featuring similar knock-out mutants [153]. Still, the preliminary results underlined the versatility of the method.

3.4.2. Antibiotic screening

The reliable sample preparation, high degree of automation, and the relatively high degree of parallelization was a motivation to explores the capabilities of the setup to act as antibiotic resistance screening device for medical/industrial applications.
The idea was to compartmentalize the experimental plate (see section 3.2.1) by using a punching die (Fig. 3.8 a), and to apply different antibiotic agents to the individual compartments by either manual pipetting or acoustic droplet ejection. Bacterial samples were then transferred to the compartmentalized plate as usual (Fig. 3.8 b) and microscpic growth was monitored using the setup (Fig. 3.8 d). Depending on the resistance to a certain agent, growth could be detected or not in a real-time analysis program (Fig. 3.8 e). The advantage of the setup would have been to easily screen multiple conditions in parallel (Fig. 3.8 c). However, compartmentalization using a punching die did not prevent diffusion of antibiotic agents to neighboring compartments. Alternative

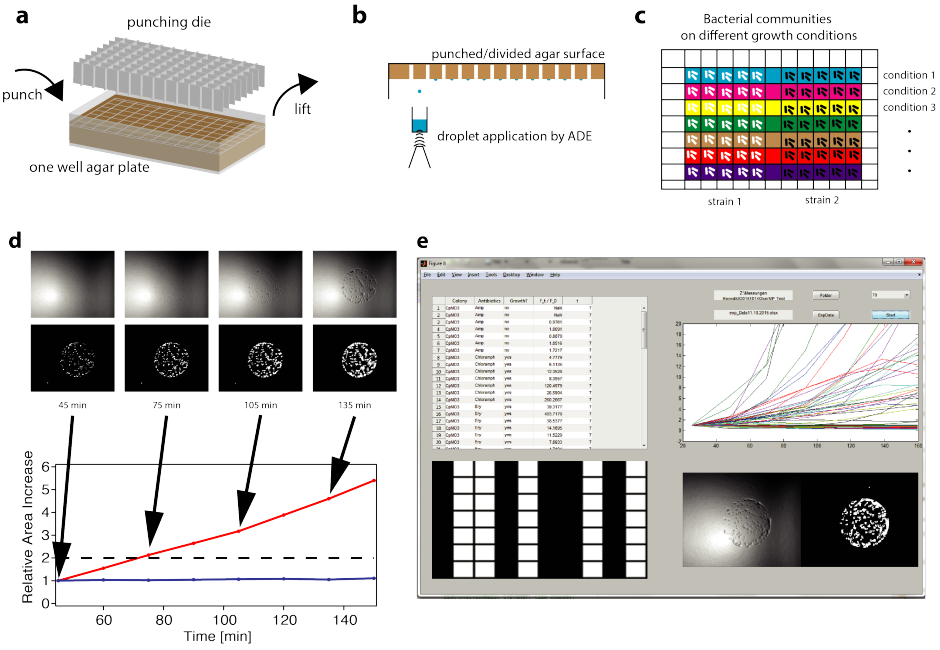

Figure 3.8.: Antibiotic screening assay

a A punching die was used to compartmentalize the experimental plate into separate sections. **b** Each of the compartments were individually treated with antibiotic agents for transfer of bacterial cultures. **c** This allowed a highly parallel investigation of multiple conditions. **d** Bacterial growth was monitored using the experimental setup in combination with image processing. Growing (red) and non-growing (blue) bacteria could be differentiated already within the first 2 hours. **e** A real-time analysis program should return the monitored information in table form (top left) or as binary growth/non-growth scheme (bottom left) derived from the individual time traces (top right) based on the image processing (bottom right).

strategies to create separated compartments, such as agar filled multi-well plates did not prove successful and the project was discontinued.
Although the approach was not developed to perfection, the exploration showed that the setup monitored microscopic growth reliably enough to let an image analysis algorithm decide if a strain is resistant or not. In addition, it again underlined the versatility of the setup.

3.5. Auxiliary high-resolution setup

To complement the multi-scale experiments and to extract single cell parameters, a Nikon 90i high-resolution upright microscope was used.
The workflow of overnight cultures, day cultures, and transfer to an experimental plate was similar to the multi-scale experiments 3.2.1. However, diluted day cultures were

pipetted manually onto solid M63 growth in standard round petri dishes. After transfer to the experimental plate, the plate was either incubated at 37°C within the setup for continuous imaging or it was incubated within an external incubator and placed into the setup only for imaging. The actual workflows are discussed in the respective results sections.
Imaging in the bright-field-, YFP-, and CFP channels was performed using a Nikon Eclipse 90i upright microscope with 50x magnification. The samples were illuminated by a Nikon Intensilight C-HGFIE lamp. Illumination light was filtered with a 570nm long pass filter (bright field), a 535 nm filter (YFP), and a 485 nm filter (CFP). Emitted light was filtered with the corresponding filters and recorded by a Nikon DS Qi1Mc camera. The objective and a Prior OptiScan II stage carrying the sample were enclosed in a custom-built heat box keeping the system at 37°C during the experiment. An additional encasing (Pecon GmbH, Erbach, Germany) prevented drying of the agar plate for continuous imaging. The imaging was operated with Nikon NIS-Elements software (Version 3.2).

3.6. Discussion

This chapter presented a novel experimental approach that fulfills previously defined requirements for the multi-scale investigation of bacterial colonies. In doing so, the approach combines high throughput sample preparation with automated fluorescence zoom microscopy and image analysis. As first applications the investigation of cooperation in biofilm formation and antibiotic screening assays were mentioned in addition to the colicinogenic interaction that the rest of the thesis focuses on.
The approach is most useful in systems that feature combined effects on the micro- and the macro-scale; for example the colicin system in which the stochastic single cell events might become important in the macroscopic competition. Furthermore, the setup is helpful when macro-scale comparisons with relatively high replicate numbers are needed; for example, when screening the colony morphology of biofilm formers, ordinary round petri dishes can contain roughly 18 colonies in reasonable distance, while the larger one-well plates allow investigates of 77 colonies in parallel.
However, the versatility of the methods comes with some draw-backs. First of all, the resolution is not comparable to inverse microscopy used in single-cell studies with 100-fold magnification. However, as was shown above, the ”near” single cell resolution is good enough to identify single cell clusters and a good compromise between maximal magnification and magnification range. The microscope could be equipped with a 2-fold magnification objective (opposed to the currently used 0.5x objective), which was omitted to avoid too large restriction in observable spatial scales.

Second, the zoom functionality necessitates high excitation powers and long exposure times for fluorescence. The total image acquisition time for all spots and fluorescence channels is the main limitation for increasing the temporal resolution. Anyway, most observable processes happen on time scales larger than the resolution.
Third, the increase of sample sizes is limited by the space available on the one-well experimental plate. Increasing the community density could lead to undesired interactions between individual colonies and would additionally decrease the temporal resolution of image acquisition. Bypassing the interactions by using larger sample plates is not possible due to standardization of the droplet ejection robot. One could think of using multiple plates in parallel to increase sample size. This would however necessitate the additional incorporation of a high precision sample changer and a completely new control unit for cultivating conditions.
In addition, the strict limitations listed above, future work could in principle improve the approach further. A feedback from the system state during acquisition by real-time analysis could improve the dynamic microscope configuration. Furthermore, image analysis still is a hard endeavor and advanced image processing techniques, such as using convolutional neural nets for example [154], could be helpful.
Despite the aforementioned limitations, the setup, once called the ”bacterial boxing ring”, fulfills the complex requirements for the autometed multi-scale observation of bacterial interactions and is a highly valued addition to existing experimental approaches [155].

4. Population dynamics of colicin E2 producers

In this chapter, I derive a phenomenological model for the population dynamics of the phenotypically heterogeneous toxin producer population based on experimental observations. Furthermore, I discuss under which conditions an average deterministic description breaks down.

4.1. Phenotypic heterogeneity in colicin E2 production

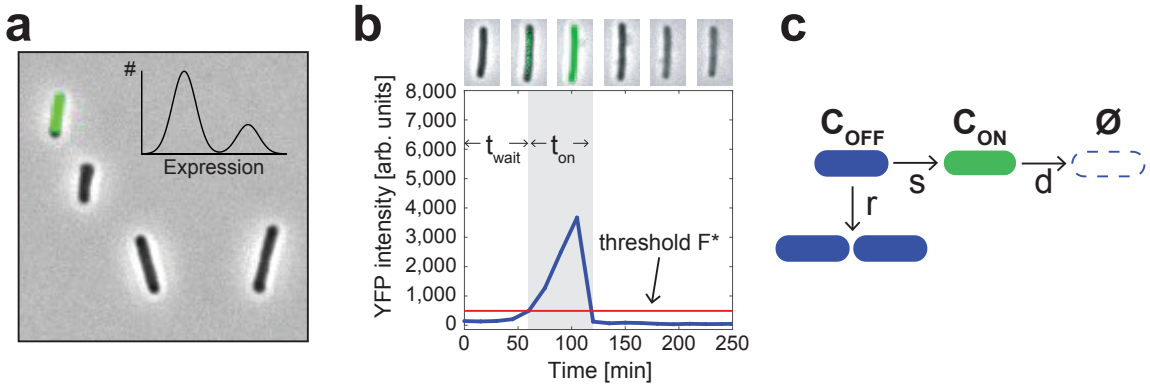

Figure 4.1.: Phenotypic heterogeneity in colicin E2 production

(a) A population snapshot illustrates the simultaneous presence of highly fluorescent and non-fluorescent phenotypes which translates into bimodal fluorescence level distribution (insert). Here, fluorescence is coupled to toxin production (see sections 2.2 & 4.1). **(b)** Time-lapse data of single-cells reveals the toxin expression dynamics. Formerly non-expressing cells switch to a highly expressing state and thereby overcome a classification threshold after a waiting time t_{wait}. After a time t_{on} in the toxin producing state, cells lyse, relase the toxin and fluorescence molecules which leads to a sharp decrease in fluoerescence intensity. **(c)** Experimental observations motivated the following model of the population dynamics. Replicating C_{OFF} cells reproduce with a rate r but can also switch to the toxin producing state C_{ON} with a rate s. Once a cell switched *on*, the cell lyses with a rate d and dies. (Images are partly reused and modified from [1] - published under creative commons license 3.0 [29].)

As outlined in chapter 2.2, colicin E2 production is subject to phenotypic heterogeneity with the presence of toxin producers and non-producing replicator phenotypes. In a

population snapshot, one detects both phenotypes simultaneously (Fig 4.1 a). Following the toxin expression dynamics with help of fluorescence reporter genes, as performed by Mader et al. [20][1], one sees how individual cells start expression randomly, followed by a steady increase up to a sharp decline in fluorescence intensity - the lysis time-point (Fig 4.1 b). By using a fluorescence threshold, cells are classified into either producer or non-producer phenotypes and toxin production can be described in terms of a stochastic switch into the producing state and out of the producing state by stochastic lysis. Additionally taking into account non-producer replication, a phenomenological model of the population dynamics can be described as in Fig. 4.1 c.

4.1.1. Experimental parameter determination

The three parameters describing the C population dynamics can be determined experimentally: the waiting time t_{wait} to switch into the toxin producing C_{ON} state, the time between switching on and lysis t_{on}, and the rate of C replication.

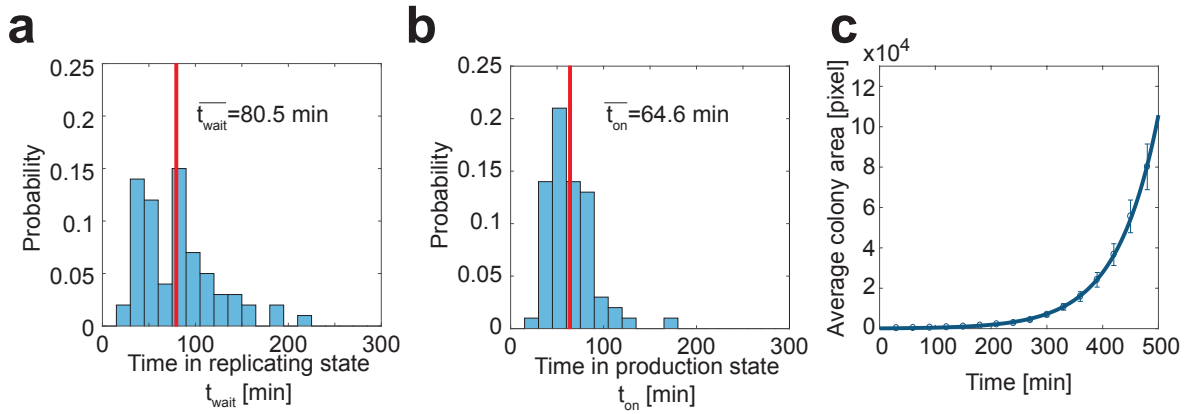

Figure 4.2.: Experimentally determined parameters of toxin dynamics
(a) Distribution of waiting times t_{wait} until a single cell switches to the on state. **(b)** Distribution of times t_{on} between switch to the on state and subsequent lysis of single cells. **(c)** Exponential area growth of mirco-colonies.

To this end, the individual fluorescence intensity time-traces (cf. Fig. 4.2 b) obtained by Mader et al. [20] were manually analysed to determine the time-point t_{wait} at which the trace starts to rise. The time in the on state t_{on} was then defined as the difference between maximum fluorescence intensity value and t_{wait}. Distributions of both values are shown in Fig. 4.2 a and b, respectively. The average value of both variable was then

[1]The author contributed to this work listed in the publication list as [M1]

used to determine the switching rate

$$s = \frac{1}{\overline{t_{wait}}} \tag{4.1}$$

and lysis rate

$$d = \frac{1}{\overline{t_{on}}}. \tag{4.2}$$

Unfortunately, the single-cell time-lapse data did not allow investigation of the replication rate. In order to determine it experimentally, microcolonies originating from single cells were incubated within an experimental setup and imaged every 30 minutes for 6-8 hours. For experimental details see section 3.5 (pipetted day culture: 4μl diluted to $OD_{600} = 0.0075$). Colony area $A(t)$ was determined using image analysis. Averaged growth data is depicted in Fig. 4.2 c with an exponential fit according to $A(t) = A(t_0)\exp(g \cdot t)$. Using the area growth rate g, the replication rate reads:

$$r = \frac{g}{\ln(2)} \tag{4.3}$$

A summary of the parameter values can be found in Table 4.1.

Symbol	Explanation	Value		Experiment
s	switching rate	0.0124 ± 0.008	min^{-1}	Single-cell time-lapse data from [20]
d	lysis rate	0.0155 ± 0.0007	min^{-1}	Single-cell time-lapse data from [20]
r	C growth rate	0.019 ± 0.001	min^{-1}	Micro-colony data (see sec. 3.5)

Table 4.1.: C population dynamics parameters

Overview of C population dynamics parameters (average ± SEM) and corresponding experiments.

4.2. Mathematical model of toxin producer fraction

4.2.1. Master equations and deterministic rate equations for population dynamics

From the phenomenological model presented in Fig. 4.1 c, one can easily find the possible transitions from and into the considered state $\mathbf{x} = (C_{OFF}, C_{ON})$ that describes the abundance of C_{OFF} replicators and C_{ON} producers in the population. Figure 4.3 explicitly displays all possible reactions.

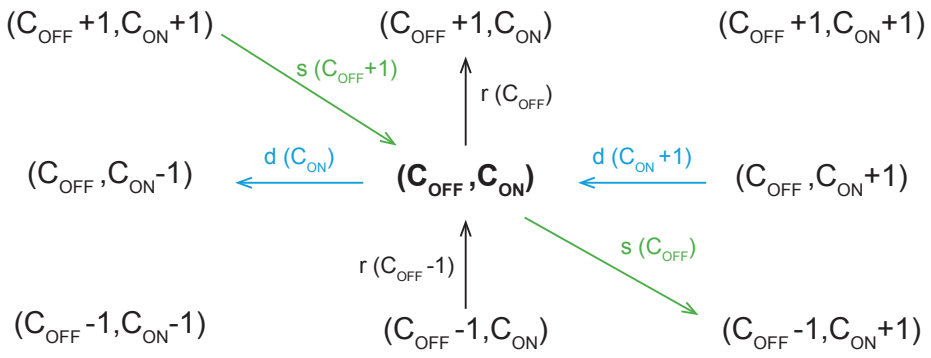

Figure 4.3.: State transitions

Focussing on the state vector $\mathbf{x} = (C_{OFF}, C_{ON})$, reactions that lead into the state (gain processes) and that originate from the state (loss processes) are due two three types of reactions: Replication of C_{OFF} cells (black), switch from C_{OFF} to C_{ON} (green) and lysis of C_{ON} cells.

Based on model presented in Fig 4.3, one can derive the stochastic population dynamics in terms of the master equations for the state vector $\mathbf{x} = (C_{OFF}, C_{ON})$ analogously to equation 2.4. Considering replication of the C_{OFF} population, switches from C_{OFF} to C_{ON} and lysis of the C_{ON} phenotype with rates r, s, and d, respectively, the master equation reads [52] (dropping the conditionals for the sake of readability):

$$\begin{aligned}
\partial_t P(\mathbf{x},t) =& \partial_t P(\mathbf{x},t|\mathbf{x_0},t_0) = \partial_t P((C_{OFF},C_{ON}),t) = \\
&+ \underbrace{r\ (C_{OFF}-1)\ P((C_{OFF}-1,C_{ON}),t) - r\,C_{OFF}\,P((C_{OFF},C_{ON}),t)}_{\text{growth}} \\
&+ \underbrace{s\ (C_{OFF}+1)\ P((C_{OFF}+1,C_{ON}-1),t) - s\,C_{OFF}\,P((C_{OFF},C_{ON}),t)}_{\text{phenotype switching}} \\
&+ \underbrace{d\ (C_{ON}+1)\ P((C_{OFF},C_{ON}+1),t) - d\,C_{ON}\,P((C_{OFF},C_{ON}),t)}_{C_{ON}\text{ lysis}}
\end{aligned} \tag{4.4}$$

Before solving the stochastic dynamics numerically (see section 4.2.2), we focus on the deterministic dynamics. For large cell numbers, fluctuations are negligible and the master equation 4.4 can be recast into deterministic rate equations [52]:

$$\begin{aligned}
\partial_t C_{OFF} =& r\,C_{OFF} - s\,C_{OFF} \\
\partial_t C_{ON} =& s\,C_{OFF} - d\,C_{ON}
\end{aligned} \tag{4.5}$$

Equation 4.5 is a system of coupled linear ordinary differential equations (ODE) that is solved analytically in the next section. Its solution allows to determine the average long-term behavior of the population dynamics. However, as we will see later (section 4.3), neglecting fluctuations can lead to strong deviations from the fully stochastic description.

4.2.2. Analytic solution of the population dynamics

In order to solve equation 4.5 analytically, a general solution scheme will be employed. For the sake of completeness, it is presented in the following

General solution of coupled linear ordinary differential equations

A system of coupled linear ordinary differential equations (ODE) can be generally solved analytically using the following *eigendecomposition* scheme (adapted from [156]):

1. Reformulate the ODE system in the form: $\partial_t \mathbf{x} = A \cdot \mathbf{x}$
2. Calculate the eigenvalues λ_i and the eigenvectors $\mathbf{v}_i$ of A.
3. Calculate the matrix $P = \begin{pmatrix} \vdots & \vdots & \vdots \\ \mathbf{v}_1 & \mathbf{v}_2 & \dots \\ \vdots & \vdots & \vdots \end{pmatrix}$ and its inverse P^{-1}. Here the columns of P are given by the eigenvectors $\mathbf{v}_i$ of A.
4. Use P^{-1} to calculate $\mathbf{y} = P^{-1}\,\mathbf{x}$ with $\partial_t \mathbf{y} = \mathrm{diag}(\lambda_1, \lambda_2, ...)\,\mathbf{y}$ in which $\mathrm{diag}(\lambda_1, \lambda_2, ...)$ denotes the diagonal matrix with the eigenvalues λ_i occupying the diagonal matrix elements.
5. The solution of $\partial_t \mathbf{y}$ is then given by $\mathbf{y}(t) = \underbrace{\mathrm{diag}(e^{\lambda_1 t}, e^{\lambda_2 t}, ...)}_{E(t)}\,\mathbf{y}(t=0)$
6. Finally, backtransformation yields the solution for the original ODE system $\partial_t \mathbf{x}(t)$

$$\mathbf{x}(t) = PE(t)P^{-1}\,\mathbf{x}(0) \tag{4.6}$$

.

Application of solution scheme to population dynamics

Using $\mathbf{x} = (C_{OFF}, C_{ON})^T$ one can rewrite the system of equations 4.5 to

$$\partial_t\,\mathbf{x} = \begin{pmatrix} r-s & 0 \\ s & -d \end{pmatrix} \cdot \mathbf{x} = A \cdot \mathbf{x} \tag{4.7}$$

The eigenvalues λ_i of A are defined by $\det(A - \lambda\,\mathbb{1}) = 0$ and after some algebra one arrives at:

$$\begin{aligned}\lambda_1 =& r - s\\ \lambda_2 =& -d\end{aligned} \tag{4.8}$$

Using the eigenvalues of A (eq. 4.8), the resulting eigenvectors are:

$$\mathbf{v}_1 = \begin{pmatrix}(d + (r-s))/s\\ 1\end{pmatrix}, \qquad \mathbf{v}_2 = \begin{pmatrix}0\\1\end{pmatrix} \tag{4.9}$$

Substituting $a = (d + (r-s))/s$, one obtains:

$$P = \begin{pmatrix}a & 0\\ 1 & 1\end{pmatrix}, \qquad P^{-1} = \begin{pmatrix}1/a & 0\\ -1/a & 1\end{pmatrix}, \qquad E(t) = \begin{pmatrix}e^{(r-s)\,t} & 0\\ 0 & e^{-d\,t}\end{pmatrix} \tag{4.10}$$

Combining the matrices from eq. 4.10 with the initial conditions $x_1(0) = C_{OFF}(0) = C^0_{OFF}$ and $x_2(0) = C_{ON}(0) = C^0_{ON}$ and using eq. 4.6, the solution for the population dynamics read:

$$\begin{aligned}C_{OFF}(t) =& C^0_{OFF}\, e^{(r-s)\,t}\\ C_{ON}(t) =& \left[C^0_{ON} - C^0_{OFF}\,\frac{s}{r+d-s}\right] e^{-d\,t} + C^0_{OFF}\,\frac{s}{r+d-s} e^{(r-s)\,t}\end{aligned} \tag{4.11}$$

In order to obtain the fraction of toxin producers within the total population, both variables (eq. 4.11) are combined to obtain:

$$Frac(t) = \frac{C_{ON}(t)}{C_{ON}(t) + C_{OFF}(t)} = \frac{C^0_{ON}\, e^{-d\,t} + C^0_{OFF}\,\frac{s}{r+d-s}\,(e^{(r-s)\,t} - e^{-d\,t})}{C^0_{ON}\, e^{-d\,t} + C^0_{OFF}\,\left(\frac{s}{r+d-s}(e^{(r-s)\,t} - e^{-d\,t}) + e^{(r-s)\,t}\right)} \tag{4.12}$$

Equation 4.12 is the analytic solution of the population dynamics in dependence on the reaction parameter r, s, and d and the initital conditions C^0_{ON} and C^0_{OFF}.
In order to capture the long term behavior of the system, lets consider the case of $t \to \infty$ with active lysis ($d > 0$) and a priori non decaying populations ($r > s$). This yields the steady state toxin producer fraction:

$$\boxed{Frac(t)_{SS} = \left[\frac{C_{ON}(t)}{C_{ON}(t) + C_{OFF}(t)}\right]_{t\to\infty} = \frac{s}{r\,+\,d}} \tag{4.13}$$

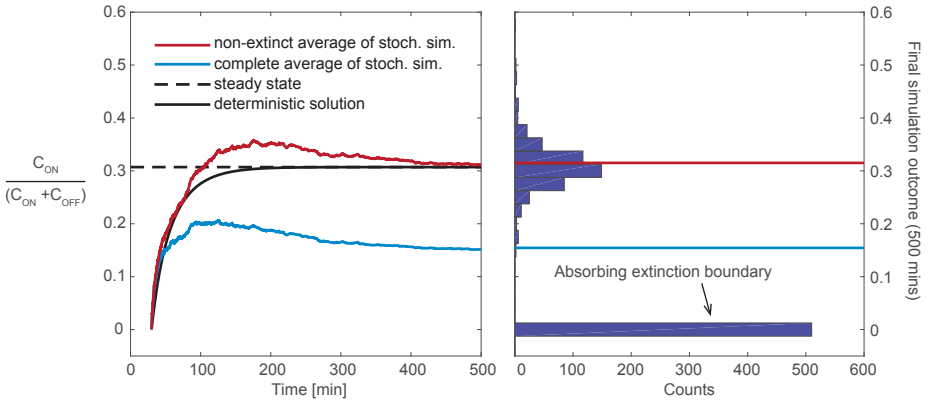

Figure 4.4.: Simulated C population dynamics

The temporal evolution (left) of the toxin producer fraction within a simulated C population shows, how the average of stochastic simulations (blue) and deterministic (black) solutions differ. The final state distribution at $t = 500min$ of 1000 stochastic realizations (right) illustrates the difference. Due to fluctuations, populations in the stochastic simulation can go extinct which is represented by the peak at $C_{ON}(t) = C_{OFF}(t) = 0$, labelled "Absorbing extinction boundary". Non-extinct populations approach the deterministic steady state value. Averaging only non-extinct realizations (red curve) creates trajectories close to the deterministic solution. (Simulation conditions: $s = 0.0124 \quad \text{min}^{-1}$, $d = 0.0155 \quad \text{min}^{-1}$, $r = 0.025 \quad \text{min}^{-1}$, $C_{ON}(0) = 0$, and $C_{OFF}(0) = 1$, $N_{total} = 1000$, $N_{extinct} = 510$)

The functional relationship of steady state and reaction rates is intuitively right. An increasing switching rate s increases the abundance of toxin producers, while an increasing lysis rate d decreases it. Larger growth rates r lead to more non-producers which decreases the relative producer abundance.

4.3. Numerical solution of the stochastic population dynamics

In order to investigate how well the population dynamics are approximated by the deterministic (eq. 4.11) and steady state solutions (eq. 4.13), the stochastic dynamics (eq. 4.4) were simulated using the Gillespie stochastic simulation algorithm [52, 54]. Figure 4.4 display a comparison of stochastic simulations, steady state and deterministic solutions of the population dynamics. In particular, the figure shows the temporal evolution of the toxin producer fraction of the C population $Frac(t) = \frac{C_{ON}(t)}{C_{ON}(t)+C_{OFF}(t)}$ (left plot) and the final distribution of 1000 realizations of the stochastic simulation (right plot). When comparing the complete average of the stochastic simulations (blue curve) to the deterministic (solid black curve) and the steady state solution (broken black

line), one observes a clear difference. This difference is due to the absorbing boundary at $C_{ON}(t) = C_{OFF}(t) = 0$ where the community is extinct with no surviving cells. Note that these cases would return $Frac(t) = 0/0$ in the simulation and were therefore set to 0.
The stochastic dynamics result in a bimodal final state distribution that includes a large peak at the absorbing boundary $Frac(t) = 0$ and a smoothly distributed accumulation around the steady state value (Fig. 4.4 right). So, the stochastic realizations create two states; one state that represents the dynamics of continuously evolving populations with large cell numbers that approach the steady state producer fraction, and an extinction state in which populations are non-viable. Therefore, when neglecting the extinction cases in averaging over the realizations, the stochastic curve approaches the deterministic solution (red curve in Fig. 4.4). In the deterministic dynamics this extinction state is never reached, once the system starts at values $C_{OFF}(t) > 0$ and the rates satisfy $d, r, s > 0$ and $r > s$. Therefore, the deterministic dynamics fails to predict the population dynamics under the conditions used above because fluctuations enable extinction. In the next section, the extinction and survival condition are discussed in more detail.

4.3.1. Population survival conditions

The above considerations raised the question under which conditions do the communities survive? In order to answer this, the stochastic simulations were repeated for a range of s, r, and d values with 1000 realizations each and the survival probability was calculated. Here, the survival probability for N realizations of the population dynamics under the same conditions was defined as:

$$S(t) = 1 - \frac{1}{N} \sum_{i=1}^{N} \delta_{0,(C_{OFF}(t)+C_{ON}(t))} \tag{4.14}$$

Here the Kronecker Delta was used that returns a contribution to the sum if the colony is extinct, i.e. $C_{OFF}(t) = C_{ON}(t) = 0$. In the following the discussion focuses on the survival probability after 500 minutes of simulations time $S = S(t = 500\text{min})$.
The lysis rate is expected to only weakly influence the survival probability because the ON state is only a delay between the replicating state and cell death. In order to investigate the influence of d on the survivial probability, both variables were plotted for the various s and r values (see Fig. 4.5). For most r-s combinations, S does not vary consistently with d. Fluctuations arise from the stochasticity of the processes and a small negative effect of d on S for small s, and r values is due to the delaying effect of d. That is, for finite simulation times, populations are not yet extinct but are expected to do so soon. Consequently, the correlation between S and d is negligible and insignificant

($r = -0.03$, $df = 998$, $p = 0.34$).

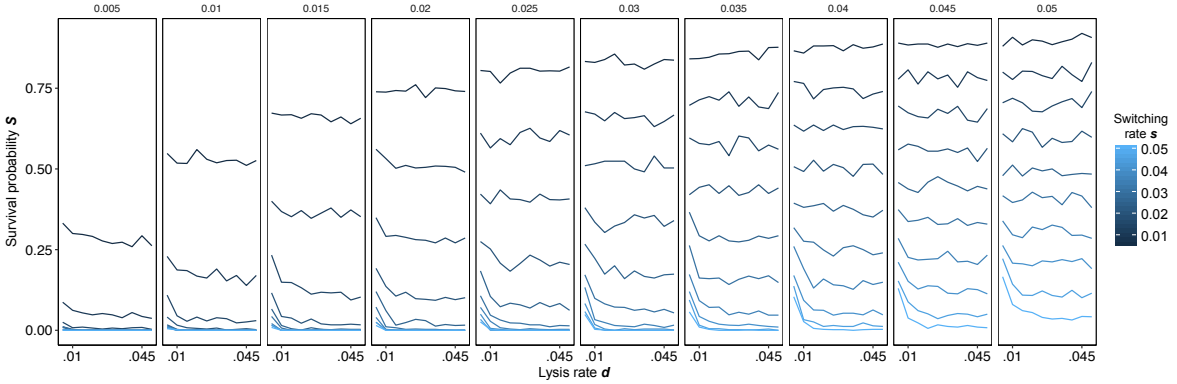

Figure 4.5.: Survival probability is independent of lysis rate

Survival probability (y-axis) in dependence on lysis rate d (x-axis) is shown for various replication rates r (panels) and switching rates s (color code).

It is evident that in the regime $s > r$ no survival is possible. There, switching is more likely than reproduction and the population goes extinct. In the ecologically reasonable regime $s < r$, S increases with r and decreases with s. Plotting the relations to S for each condition separately (see Fig. 4.6 a & b) allows to experimentally determine functional relationships for the dependencies. From the plots one finds $S \propto 1 - 1/r$ and $S \propto -s$.

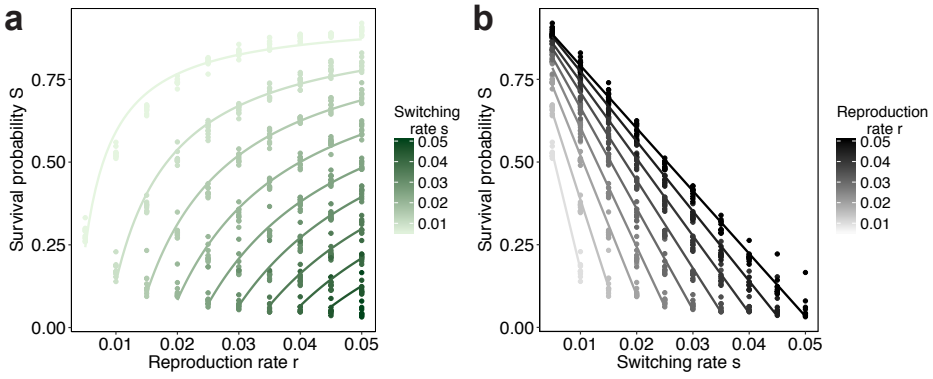

Figure 4.6.: Survival probability and reaction rates

a Under ecologically reasonable conditions ($r > s$), survival probability S increases with r and can be approximated by a fit proportional to $S \propto 1 - 1/r$ (lines), different s conditions are given by color code. **b** Similarly, dependence of S on switching rate s was investigated for a range of r values (color code). Here, a negative trend $S \propto -s$ (lines) could be identified.

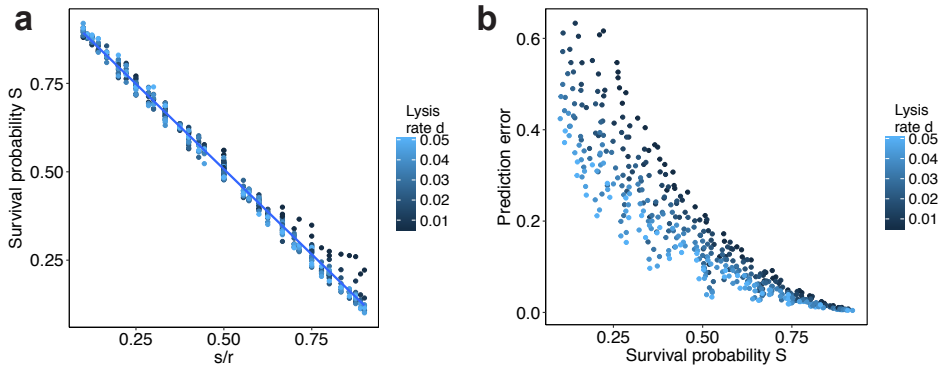

Figure 4.7.: General survival rule and prediction error

a The survival probability S depends linearly on s/r (Eq. 4.15) and various d collapse onto a common line. **b** The prediction error increases with decreasing survival probability and lysis rate d.

Combining the two proportionalities into a combined survival rule yields $S \propto -s/r$. Plotting S versus s/r validates the above considerations (see Fig. 4.7 a) and the survival rule can be identified as:

$$S = 1 - s/r \tag{4.15}$$

In order to asses the deviation of deterministic prediction and the average of stochastic simulation, the difference between both variables was calculated and plotted for the various survival probabilities (see Fig. 4.7 b). With increasing survival probability, the extinction probability is decreased and consequently the deviation from the deterministic prediction reduced.
Interestingly, the deviation is changing with respect to the lysis rate d (color code in Fig. 4.7 b). Especially for low survival probabilities, smaller d values increase the error.

4.3.2. Survivial probability and initial population size

In the above discussion was restricted to initial populations of $\mathbf{x_0} = (1, 0)$. For the sake of generality, the range of $\mathbf{x_0} = (C_0, 0)$ initial populations was simulated for a range of r and s values with a fixed $d = 0.05$.
Plotting the survival probability S versus the s/r ratio for the various C_0 cases (Fig. 4.8 a), it is evident that the shape of the relation changes from a straight line to concave dependence.

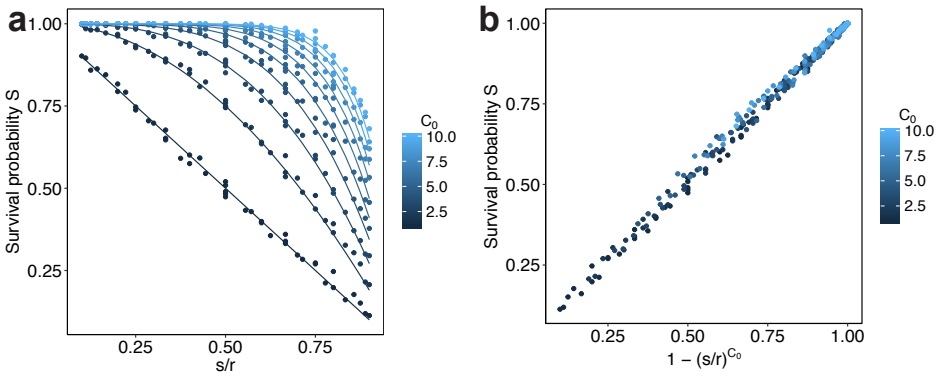

Figure 4.8.: Survival probability and population size

a The S-s/r diagram shows a clear dependence on C_0 (color code). The results of stochastic simulations (dots) agree very well with the derived general survival rule (lines according to eq. 4.16) **b** Plotting S versus the survival rule, shows a collapse of various C_0 conditions on a common line.

In order to understand this change, we calculate the survival probability function. In equation 4.15, one can identify s/r as the extinction probability for the $C_0 = 1$ case. In case of two initial C_{OFF} cells, the extinction probability for the first cell is s/r, and for the second cell it is also s/r. In the general case of C_0 initial cells, the extinction probability is $\prod_{j=1}^{C_0} s/r = (s/r)^{C_0}$ and the survival probability reads:

$$\boxed{S = 1 - (s/r)^{C_0}} \tag{4.16}$$

Plotting this functional relationship into the S-s/r diagram for various C_0 values (Fig. 4.8 a) shows a perfect agreement and validates the above considerations. Additionally, S was plotted against $1 - (s/r)^{C_0}$ and here one sees, how well the different C_0 conditions collapse onto a common line (Fig. 4.8 b). Quantifying the agreement using linear regression, one finds very high values for both the significance ($p < 2.2 \cdot 10^{-16}$) and the goodness of fit ($R^2 = 0.9965$).

4.4. Conclusion

In this chapter, a phenomenological population dynamics model was developed for the phenotypic heterogeneity in colicin E2 production. Corresponding reaction rates were derived from experimental data. From this model, the stochastic population dynamics were formulated in terms of master equations and a deterministic approximation resulted in a system of ODE that was solved analytically. Comparing results of the deterministic and the stochastic population dynamics revealed a clear difference between both approaches. This break-down of the deterministic approximation was found to be due to population extinction enabled by fluctuations.
Consequently, the following investigation focused on the conditions of survival and extinction. Computational and theoretical arguments resulted in a survival rule that depends on reaction rates and the initial population size. Later, in chapter 6, a similar empirical survival rule is found to be proportional to the number of viable C clusters.
Furthermore, the results showed that the lysis rate d did not influence the survival probability. However, small d were found to increase the prediction error, or stated positively, the variability of community composition. This increase in variability is likely a second evolutionary purpose of enlarged delay times, i.e. small lysis rates, that were recently found in wild type strains [92], in addition to increased amounts of toxin produced.

5. Population dynamics of mixed colicin E2 communities

In this chapter, I will formulate a mathematical model to describe the interaction of the colicin producing population with a population of sensitive bacteria. First, I will present a phenomenological model of the interaction to motivate the reactions considered. Second, I will derive a stochastic, lattice based 2-D model of the interaction in terms of a master equation and extend the model to include a third bacterial population. Subsequently, I will outline, how the underlying biological processes are simulated computationally and finally, I will discuss the advantages and disadvantages of the model and compare it to previous studies.

5.1. Phenomenological model

Starting from the two-phenotype model of the colicin producer population (see section 4.1), it is not hard to arrive at the a model for the two-strain competition of the colicin producer (C) with sensitive bacteria (S strain) (see Fig. 5.1). In contrast to earlier studies that reduce the toxin production to effective growth rate costs for the C and the toxin action to an effective growth rate reduction of the S strain, this model starts from the individual cell level. The importance of cell individuality and stochasticity has been highlighted and discussed in the previous chapter.
In addition to the reactions considered in the colicin producer population model, one now includes the release of colicin into the environment upon cell lysis.
Like the C cells, S cells can proliferate with a rate r_S and switch into a growth arrested state S_{Stop} upon encountering the toxin. The rate of this switch reaction is given by the toxin sensitivity times the colicin concentration at the position of the S cell $s_S \cdot [Colicin]$. In general, S_{Stop} cells can die with a rate $d_{S_{Stop}}$.

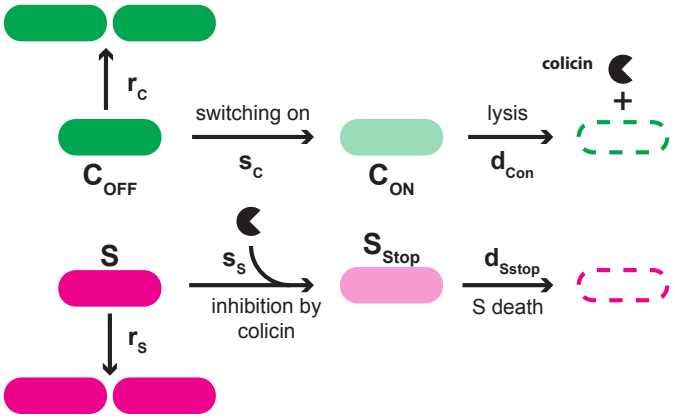

Figure 5.1.: Phenomenological model of two-strain colicinogenic interaction
Two competing bacterial populations of heterogeneously toxin producing (S, green) and toxin sensitive (C, magenta) bacteria can react in the following way. C and S cells can proliferate with rate r_C and r_S, respectively. C cells can switch into the toxin producing state C_{ON} with rate s_C and subsequently lyse with a rate $d_{C_{ON}}$ and release the toxin. Upon encountering toxin molecules, S cells can switch into a growth inhibited state S_{Stop} with rate $s_S \cdot [Colicin]$ before they die with rate $d_{S_{Stop}}$.

5.2. Mathematical model

From the phenomenological model presented above, one can formulate master equations in analogy what was done in chapter 4. However, here, the goal is to develop a spatially explicit model that captures the features of the range expansion experiments (chapter 6 and 7). Therefore, a spatially discretized version of the master equation on a lattice was used.
Here, the variable $P(T; x, y, t)$ describes the probability to find a lattice site of type T at position (x, y) at time t. In general, the set of possible lattice types and transitions between them depend on the system under consideration. In the two-strain interaction of S and C, the five possible lattice types are proliferating C cells, toxin producing C_{ON} cells, proliferating S cells, growth inhibited S_{Stop} cells, and free lattice sites which are denoted with the symbol F (see Fig. 5.2 c).
Transitions between cells states happen according to the six processes discussed above: growth with rate r_T, switch to the toxin producing state or the growth inhibited state, respectively, with rate s_T, or liberation of occupied sites by cell lysis or death with rate d_T (see Fig. 5.2 c). Growth of cells during one reaction step can only happen to nearest neighbor sites defined by a set of positions $\mathcal{N}(x, y)$ called neighborhood of a given position (x, y). Here, a Moore neighborhood of 8 nearest neighbors is used [157].
In addition to the bacterial cells occupying the lattice sites, a discretized colicin con-

centration field $c(x, y, t) = [Colicin]$ is present at every position.

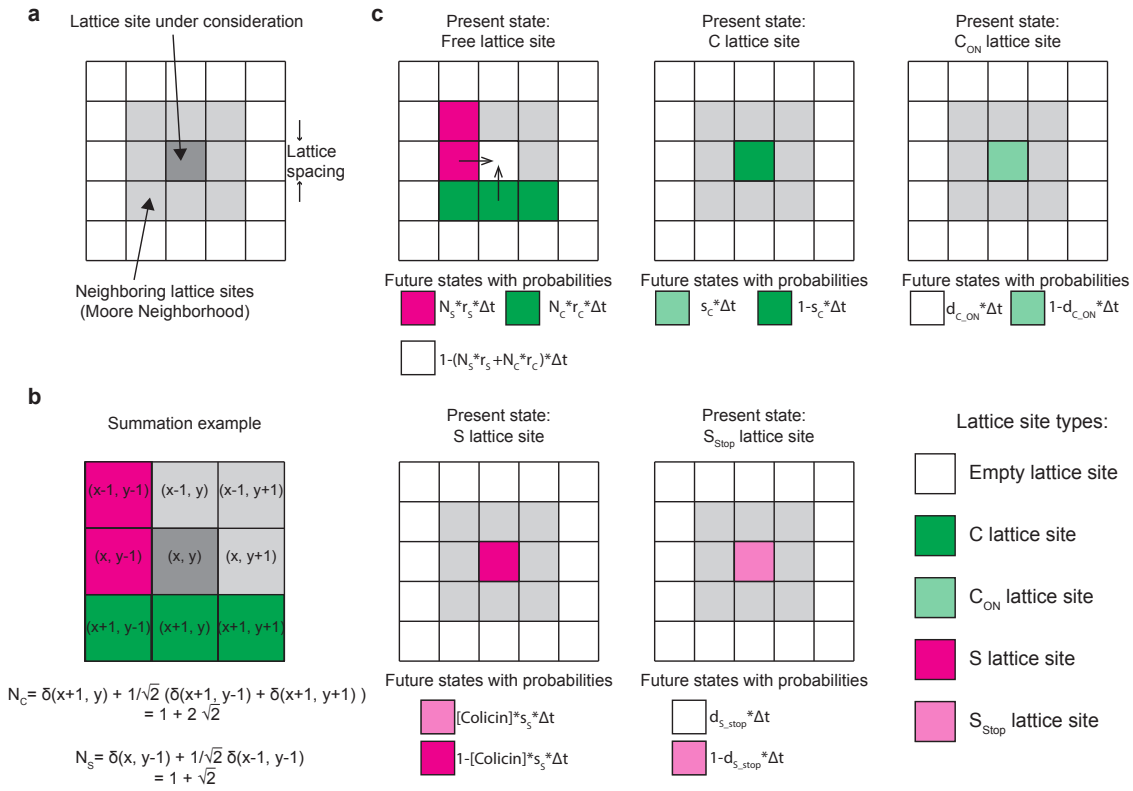

Figure 5.2.: Lattice model of the two-strain colicinogenic interaction
(a) For every non-boundary cells, a neighborhood $\mathcal{N}(x, y)$ contains the 8 nearest neighbors. **(b)** The summation with diagonal scaling according to equation 5.2 is illustrated. Note that δ-functions that return 0 are omitted for readability. **(c)** For every possible lattice type, the possible future states and corresponding reaction probabilities are shown.

While the state switch and death reactions happen locally, growth reactions can occur from neighboring sites. Therefore the number of S or C cells in the neighborhood determines the probability of growth into the focal free spot in during the present time-step. Using

$$\delta_{T,C}(x^*, y^*) = \begin{cases} 1, & \text{if} \quad T(x^*, y^*) = C \\ 0, & \text{if} \quad T(x^*, y^*) \neq C \end{cases} \tag{5.1}$$

as the type indicator δ-function and $f \in \{1, \frac{1}{\sqrt{2}}\}$ as a prefactor, we find for the number of neighboring C cells:

$$
\begin{aligned}
N_C(x,y) = &\sum_{\substack{(x^*,y^*)\\ \in\mathcal{N}(x,y)}} f\cdot\delta_{T,C}(x^*,y^*)\\
=&\delta_{T,C}(x-1,y)+\delta_{T,C}(x+1,y)+\delta_{T,C}(x,y-1)+\delta_{T,C}(x,y+1)\\
+&\frac{1}{\sqrt{2}}\Big[\delta_{T,C}(x-1,y-1)+\delta_{T,C}(x+1,y-1)+\delta_{T,C}(x-1,y+1)+\delta_{T,C}(x+1,y+1)\Big]
\end{aligned}
\tag{5.2}
$$

Note that the influence of diagonal neighbors is scaled by a pre-factor $\frac{1}{\sqrt{2}}$ as performed in earlier studies [25]. Analogously one defines $N_S(x,y) = \sum_{\substack{(x^*,y^*)\\ \in\mathcal{N}(x,y)}} f\cdot\delta_{T,S}(x^*,y^*)$. Figure 5.2 b illustrates this summation with an example.
The S state-switching occurs upon encountering of colicin molecules. Therefore the switch reaction is proportional to the colicin concentration $c(x,y,t)$. See section 5.3.3 for a detailed discussion on how the colicin field is modelled.

5.2.1. Master equations

In general the master equation for the systems reads analogously to equation 2.6:

$$\partial_t P(T;x,y,t) = \sum_U \left[w_{TU}\,P(U;x,y,t) - w_{UT}\,P(T;x,y,t)\right] \tag{5.3}$$

Here, the state T of a given lattice site (x,y) at time t is given by gain and loss reactions from and to state U. Taking into account the above considerations, one can write down the master equations for the five different states.
The reproducing lattice states C and S grow from free lattice sites F and can switch to the non-reproducing states C_{ON} and S_{Stop}, respectively. Consequently, one finds:

$$\partial_t P(C;x,y,t) = r_C\,N_C\,P(F;x,y,t) - s_C P(C;x,y,t) \tag{5.4}$$

and

$$\partial_t P(S;x,y,t) = r_S\,N_S\,P(F;x,y,t) - s_S\,c(x,y,t)\,P(S;x,y,t) \tag{5.5}$$

The toxin-producing state C_{ON} and the inhibited state S_{Stop} gain from switching and lose due to cell death. Accordingly, one writes down:

$$\partial_t P(C_{ON};x,y,t) = s_C\,P(C;x,y,t) - d_{C_{ON}}\,P(C_{ON};x,y,t) \tag{5.6}$$

and

$$\partial_t P(S_{Stop}; x, y, t) = s_S\, c(x, y, t)\, P(S; x, y, t) - d_{S_{Stop}}\, P(S_{Stop}; x, y, t) \tag{5.7}$$

Finally, the free lattice sites F gain from cell death and lose due to growth from neighboring sites. The master equation for this state reads:

$$\begin{aligned} \partial_t P(F; x, y, t) =& d_{C_{ON}}\, P(C_{ON}; x, y, t) + d_{S_{Stop}}\, P(S_{Stop}; x, y, t) \\ & - r_C\, N_C\, P(F; x, y, t) - r_S\, N_S\, P(F; x, y, t) \end{aligned} \tag{5.8}$$

One can easily see that the equations fulfill conservation of probability because of $\sum_T \partial_t P(T; x, y, t) = 0$.

5.2.2. Extension to three strain interaction

While the above derivation was motivated by the two-strain interaction of colicin producing and sensitive populations, it is not hard to extend the model to include a third, resistant strain R. An additional equation for the R strain must be introduced but since resistance prevents colicin induced state switching it just contains a growth term with growth rate r_R:

$$\partial_t P(R; x, y, t) = \underbrace{r_R\, N_R\, P(F; x, y, t)}_{\text{R growth}} \tag{5.9}$$

Furthermore, the free lattice state is affected by growth and because of missing R cell death, only a growth loss term is added:

$$\begin{aligned} \partial_t P(F; x, y, t) =& d_{C_{ON}}\, P(C_{ON}; x, y, t) + d_{S_{Stop}}\, P(S_{Stop}; x, y, t) \\ & - r_C\, N_C\, P(F; x, y, t) - r_S\, N_S\, P(F; x, y, t) - \underbrace{r_R\, N_R\, P(F; x, y, t)}_{\text{R growth}} \end{aligned} \tag{5.10}$$

Simulations of three strain interactions will be presented and discussed in chapter 7. For the remainder of this chapter, however, we focus on the two-strain interaction.

5.3. Numerical solution

Due to the categorical nature of the state variable T and the limited number of interacting agents, the spatially explicit consideration will always be subject to non-negligible fluctuations. Therefore, the model was solved numerically using a stochastic simulation algorithm on a $N \times N$-lattice. An overview of the simulation algorithm is given in Fig. 5.3.
In short, the algorithm includes three nested loops. The first loop iterates over the individual experimental conditions and replicates. In general, for each condition and replicate the lattice to be simulated is newly initialized, except for cases in which comparison of exactly the same initial conditions were desired. After initialization, the algorithm iterates over the second temporal loop with fixed time-step until the simulation time is reached. Within the temporal loop, iteration over the individual lattice sites occurs (loop three) and for each lattice site stochastic updates happen. Notably, the simulation algorithm includes coarse-graining steps if the simulated community touches the lattice boundary and the lattice is rescaled. The individual aspects mentioned here in short are discussed in detail in the following sections.

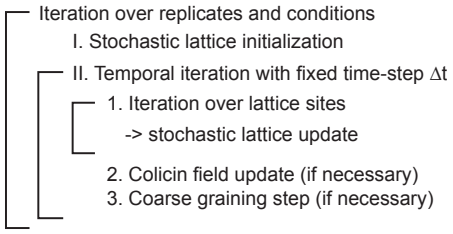

Figure 5.3.: Simulation algorithm
The simulation algorithm contains three nested loops that iterate over the replicates and simulation conditions, the time-steps, and the lattice sites.

5.3.1. Stochastic lattice intitialization

The initial conditions were chosen in accordance to the experimental setting. The circular shape of initial experimental communities was approximated by a sixteen-sided polygon with a diameter $D_{polygon}$. The initial community composition was generated stochastically according to the initial experimental ratio $I_C : I_S$.
In particular, a random $N \times N$ matrix $\mathcal{R}$ with values ranging from 0 to 1 was elementwise multiplied with a matrix $\mathcal{P}$ containing the sixteen-sided polygon as ones and otherwise zeros resulting is a matrix $\mathcal{G}$. Then, using the initial density of cells ρ the random numbers were used to classify pixel into one of the three state variables F, C, S according

to:

$$T(x,y,t=0) = \begin{cases} S, & \mathcal{G}(x,y) < \frac{I_S}{I_C+I_S} \cdot \rho \\ C, & \mathcal{G}(x,y) > 1 - \frac{I_C}{I_C+I_S} \cdot \rho \\ F, & \text{otherwise} \end{cases} \tag{5.11}$$

The classification scheme (eq. 5.11) can be easily generalized to include more lattice species. The process is illustrated in Fig. 5.4.

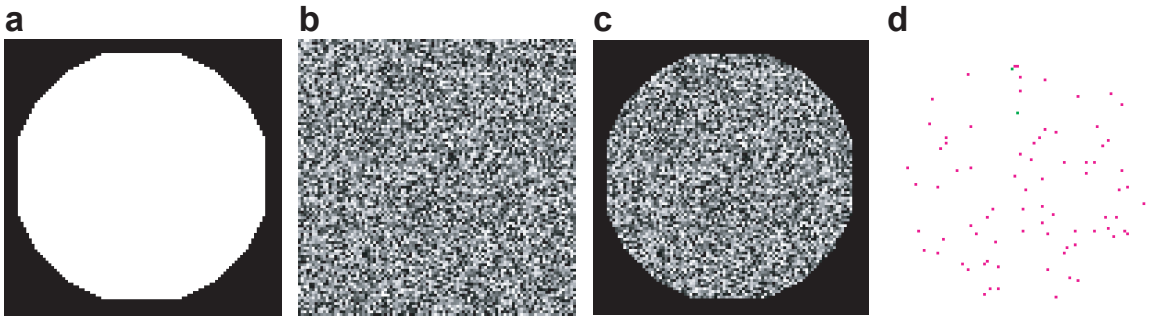

Figure 5.4.: Example initialization

Initiation example depicted for $\rho = 0.01$, $I_C = 2$, $I_S = 100$, and $N = 100$. **(a)** Shape matrix $\mathcal{P}$ is elementwise multiplied with random matrix $\mathcal{R}$ **(b)** resulting in matrix $\mathcal{G}$ **(c)** which is used for classification. **(d)** After classification according to eq. 5.11 the initial lattice $T(x,y,t=0)$ is constructed. Here, S lattice sites are colored magenta, C lattice sites green and free lattice sites F are white.

5.3.2. Stochastic lattice update

At the core of the simulation algorithm is the iterative stochastic lattice update (Fig. 5.5). Here, a fixed time step Δt is used in a *naïve* stochastic simulations algorithm (SSA) [158].

At every time-point, the algorithm iterates over all non-empty ($T \neq F$) and adjacent lattice sites. At every lattice site, the reaction probabilities are calculated according to the lattice site type, reaction rates, time-step size Δt, and Neighborhood composition (in case of $T = F$). See Fig. 5.2 c for an overview of lattice sites and corresponding reaction probabilities. Then, a random number is drawn that determines the reaction to happen, and the lattice site is updated. See Fig. 5.5 for an illustrating example of a lattice update. After the algorithm updated all relevant lattice sites, the simulation time $t_i = t_{i-1} + \Delta t$ is updated. The iteration is repeated until the final simulation time $t = \mathcal{T}$ is reached.

From the explicit calculation of reaction probabilities one sees a difficulty of a fixed-time step algorithm. Care must be taken in choosing Δt in order to prevent partial reaction

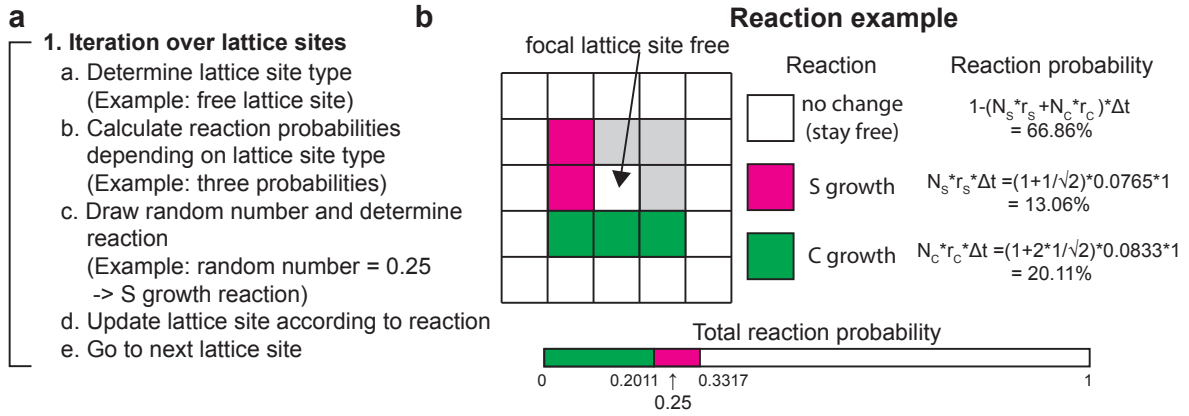

Figure 5.5.: Lattice update iteration with example

(a) Lattice update algorithm is illustrated in detail for the lattice update at a given lattice site in general and refers to example on the right. **(b)** Example of lattice update for a free lattice site. For the three possible reactions C growth, S growth, and no lattice site change, the reaction probabilities are calculated. Then, a random number is drawn (e.g. 0.25) and compared to the cumulative total reaction probability (bottom line). As the random number 0.25 falls into the red interval representing S growth reactions, the lattice site is updated to be a S site in the following.

probabilities > 1.

5.3.3. Colicin field modelling

During a lysis reaction of a C_{ON} cell, colicin is released into the environment. In the model, the toxin distribution is realized via an global colicin field $c(x, y, t)$ which is described as the superposition concentration profiles that originate from lysed C_{ON} cells. The colicin profiles are assumed to decay exponentially in space with rate λ and stay constant in time [25, 159, 160]. Mathematically, the colicin profile is then defined as

$$c(x, y, t) = \sum_{(x_j, y_j)} e^{-\frac{1}{\lambda}\sqrt{(x_j - x)^2 + (y_j - y)^2}} \cdot \sum_{\tau=0}^{t} \Pi(x_j, y_j, \tau; C_{ON} \to F) \tag{5.12}$$

Here, the lysis events at a given position and time (x, y, t) are denoted with

$$\Pi(x, y, t; C_{ON} \to F) = \begin{cases} 1, & \text{if lysis event occured at } (x, y, t) \\ 0, & \text{otherwise} \end{cases} \tag{5.13}$$

Figure 5.6 illustrates the numerical construction of a colicin profile that originates from a newly lysed C_{ON} cell.

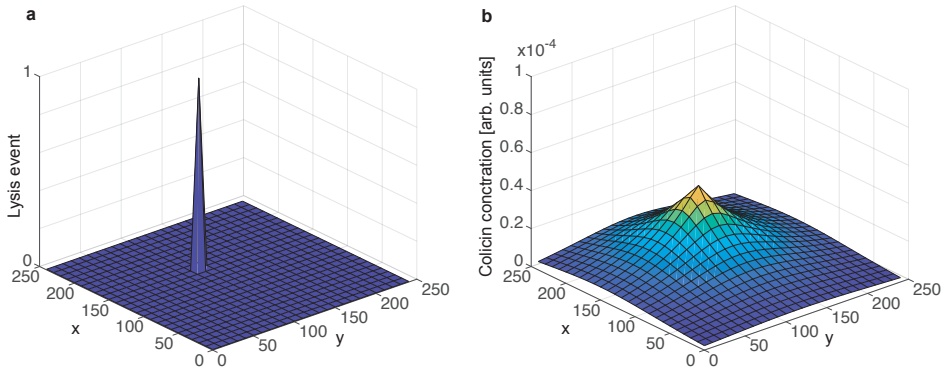

Figure 5.6.: Construction of colicin profile

(a) The position of a recently lysed C_{ON} cell is depicted with a sharp peak. **(b)** In order to construct the colicin profile from this, an exponentially decaying profile is assumed to originate from this position.

The static construction of colicin profiles presented here is computationally much simpler compared to the explicit consideration of colicin diffusion. It is justified because colicin diffusion happens on much faster time scales compared to the other reactions considered [25, 161].

5.3.4. Coarse graining

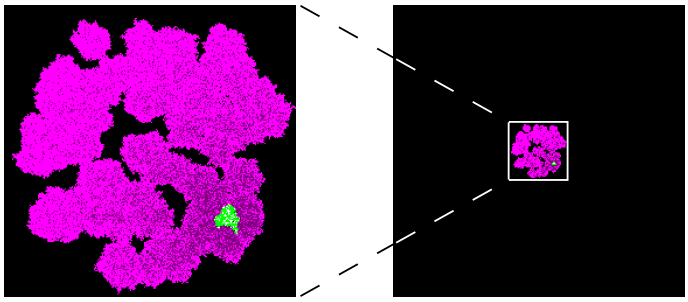

Figure 5.7.: Coarse-graining illustration

As soon as the expanding colony reaches the lattice edge, the simulated community is rescaled by a constant factor z and the resulting $N/z \times N/z$ lattice is placed at the center of a new $N \times N$ lattice. (here: $N = 250$, $z = 5$)

The detailed spatial resolution and the fixed time-step are computationally expensive and necessitate the use of small lattices to make the simulation computationally tractable. At the same time, the simulated community is expanding occupying ever

increasing lattice space, which calls for large lattice sizes. In order to resolve this conflict, coarse-graining was used motivated by the experimental zooming functionality (see section 3.2.3).
As illustrated in Fig. 5.7, the simulated lattice is rescaled by a factor z as soon as the expanding colony reaches the lattice edge. The resulting $N/z \times N/z$ lattice is placed at the center of a new $N \times N$ lattice. Rescaling is performed by inheriting only every z-th element and discarding the rest. After the rescaling step, the simulation is continued with rescaled reaction rates $r' = r/z$.

5.3.5. Growth rate determination

The strain growth rates were determined by fitting of the simulations of pure communities ($I_C = 0$ or $I_S = 0$) to average experimental growth data obtained in control experiments using MATLAB's built-in function `fminsearch`. Because fitting was computationally costly, the explicit fitting was only performed for the the S strain. Growth rates for the other strains were then obtained by comparison of linear area growth rates after 20 hours assuming a simple linear relationship between area growth and microscopic growth rates [162].
Figure 5.8 compares an experimental observation and a stohastic realization of optimized simulated growth. Additionally, linear area growth is shown by fitting a line to the experimental data.

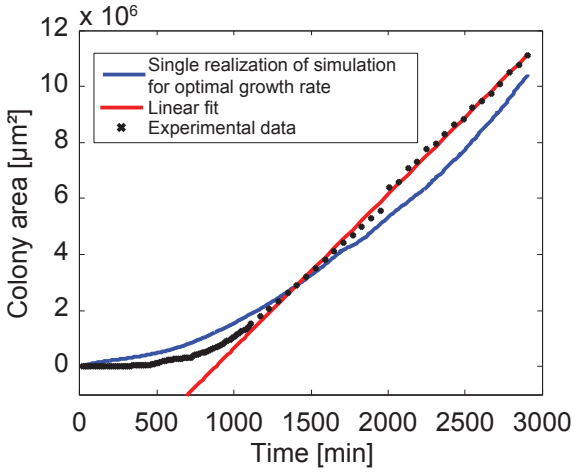

Figure 5.8.: Growth rate determination
Colony area time-lapse data is shown for experimental (black), simulated (blue), and linear regime fit (red). (Image is reused from [141] published under creative commons license 4.0.)

5.3.6. Parameter overview

During the general discussion of the various simulation aspects, several relevant simulation parameters were mentioned. For the sake of clarity, table 5.1 presents an overview of simulation parameters, their scaling behavior under coarse-graining operation, typical values, and references for typical values.
Unless otherwise stated, simulations referenced in the remainder of this thesis used the parameters from the list.

Symbol	Explanation	Scaling	Typical value	Reference
N	Lattice size	$N' = N$	250	-
Δx	Lattice spacing	$\Delta x' = \Delta x \cdot z$	$2\mu m$	-
z	Rescaling factor	-	5	-
Δt	Time-step size	-	1.5 min	-
$\mathcal{T}$	Total simulation time	-	2910 min	Similar to experiments
$D_{polygon}$	Initial colony diameter	-	225 pixel	Similar to experiments
$I_C : I_S$	Initial C:S-ratio	-	2:100	Similar to experiments
ρ	Initial density	-	0.002	Similar to experiments
λ	Colicin profile decay rate	$\lambda' = \lambda/z$	$125\mu m^{-1}$	taken from [25]
r_C	C growth rate	$r'_C = r_C/z$	0.0729	fit to exp. data from [141]
r_S	S growth rate	$r'_S = r_S/z$	0.0607	fit to exp. data from [141]
r_R	R growth rate	$r'_R = r_R/z$	0.0876	fit to exp. data from [141]
s_C	C switching rate	$s'_C = s_C/z$	e.g. 0.02	Externally tuned according to eq. 4.13
s_S	S switching rate	$s'_S = s_S/z$	1500	see chapter 6
$d_{C_{ON}}$	C_{ON} death rate	$d'_{C_{ON}} = d_{C_{ON}}/z$	0.02	From single cell studies (see sec. 4.1.1)
$d_{S_{Stop}}$	S_{Stop} death rate	$d'_{S_{Stop}} = d_{S_{Stop}}/z$	0.001	negligibly small in [141] and set to zero in [163]

Table 5.1.: Simulation parameters
Overview of simulation parameters, scaling behavior under coarse-graining operation, typical values, and references for typical values.

5.4. Simulation

After all the technical details of the computational model, we will now shortly discuss general properties of the model before it is applied to specific problems and discussed in the biological context in chapters 6 and 7.

5.4.1. Competition dynamics

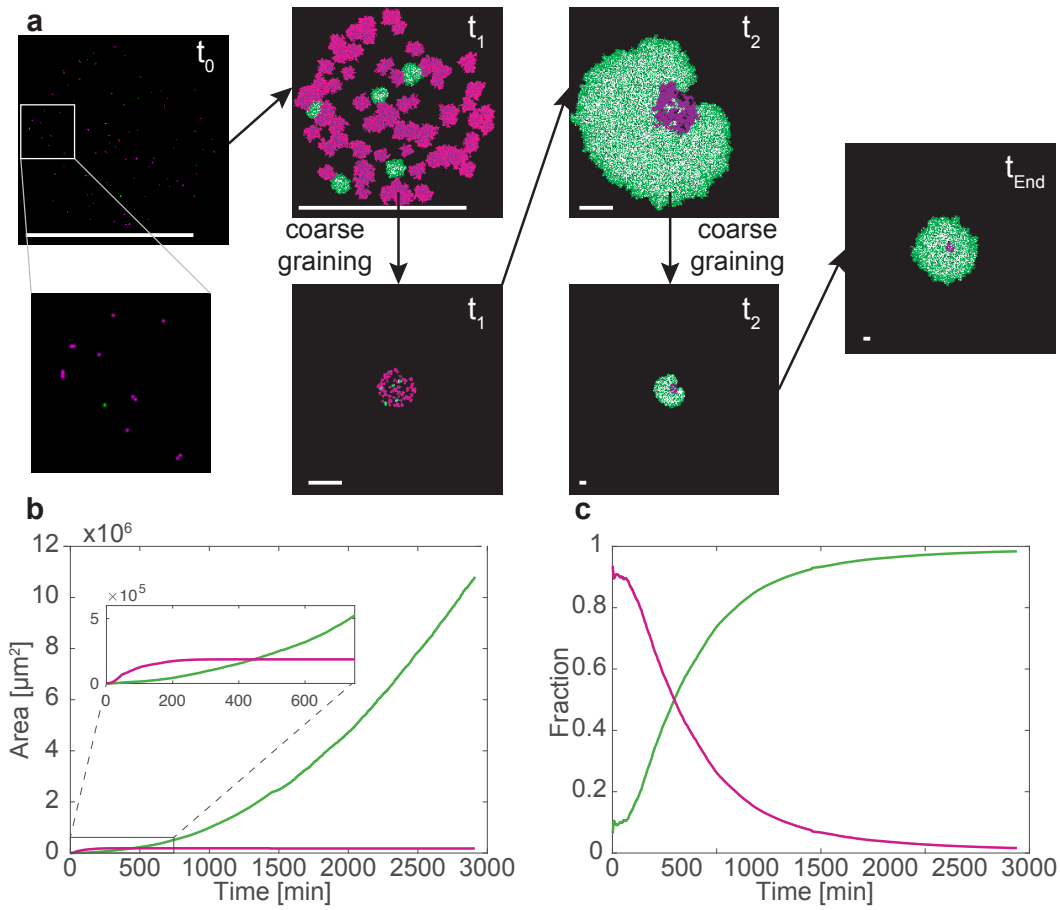

Figure 5.9.: Exemplary simulation

a Exemplary simulation featuring two coarse graining steps. After initialization (t_0 with magnified insert), cells expand and induce a coarse-graining step at t_1. In the second regime the C strain takes over until another coarse-graining step becomes necessary (t_2). From there on the colony just expands until t_{End}. Note how the scale bar (400 μm) changes with every zoom step. Color code: C green, C_{ON} white, S bright magenta, S_{Stop} dark magenta, F black. **b & c** Absolute simulated area **(b)** and relative fraction **(c)** show C take-over during competition. Color code: C green, S magenta.

A typical simulation time-course is displayed in figure 5.9. Panel a illustrates how the lattice sites evolves over time. From the sparsely populated initial lattice (t_0), the individual cells build clusters (t_1) and once the lattice border is touched, the coarse-graining step is performed (t_1 bottom). Then, the competition continues and here C takes over the population. At t_2 another coarse-graining step is performed before the simulation ends after a fixed time t_{End}. Panels b and c display the absolute and relative area of both strains respectively. Again, the take-over of C is evident.
The model was calibrated using experimental data and used to predict competition outcome distributions. Overall, the computational and experimental results have been found to agree well and will be discussed in detail in chapters 6 and 7.

5.5. Discussion

This chapter presented a spatially explicit computational model of the population dynamics in the colicin E2 system. As we will see later, the model delivers competition outcomes in good agreement to experiments and the dynamics are at least qualitatively similar to the experimentally determined ones. While the biological relevance will be discussed in the following chapters, here, I focus on discussing the technical aspects and validity of the assumption made in formulating the model.
In addition to well-mixed models, spatially explicit models have long been used to study ecological model systems [117, 118]. They comprise lattice based models [16], as well as individual based models [116] to investigate ecological interactions and pattern formation. Traditionally, models of the colicinogenic interaction [97, 99, 101] do not consider the phenotypic structure of the colicin producer population. Only recently, models do not only explicitly model both phenotypes [25] but also vary the phenotypic structure to probe the ecological system response [21]. Similarly in the model presented here, the phenotypes are explicitly considered and starting from initially small population sizes really allows the system to approach the absorbing extinction boundary.
Interestingly, the model and experimental results of publication [B1] have been discussed from the perspective of percolation theory and using a simplified spatial model of the pure C population dynamics confirm a phase transition from perstistence to extinction phase [155].
A novel aspect of the simulation algorithm used is a coarse-graining step that occurs once the growing population touches the lattice boundary. The advantage of the coarse-graining step is the reduction of computational time while maintaining the microscopic structure of initial community composition. While the transfer of only every z-th lattice site (typically $z = 5$) potentially introduces critical errors due to irregular removal of rare lattice site types, the coarse-graining happens after the initial demixing [164] and therefore errors are estimated to be small.

Another distinctive feature of the algorithm is the fixed time step of a *naive* stochastic simulations algorithm (SSA) [158]. While the fixed time steps allows control over the computational time elapsed, it is computationally expensive because in many iterations the lattice site does not change. Gillespie's SSA [52, 54] has the advantage that only updates in which the state variable changes are considered and, thus, is faster.
In addition to the algorithmic details, some of the underlying assumption have to be critically discussed. First of all, the model simulates a three dimensional colony as a 2D projection. This introduces differences between single cell doubling rate and area growth rate. Therefore, the computational growth rate is overestimated initially. Furthermore, after application of the cells to the agar surface they are subject to a growth lag such that they start replication only after a lag time [25]. This was not considered here and could be introduced to improve the description of microscopic growth.
Another inaccuracy of the model is the neglect of mechanical forces which have been recently found to play a crucial role in range expansion sector formation [165]. Such mechanical forces can prevent the trapping of replicating cells behind small numbers of non-replicators, i.e. C cells could push away inhibited S_{Stop} cells and break through to continue growth.
Recent results questioned the view that once a C cell switched to toxin production it certainly lyses and cannot switch back [21]. However for the model presented here, these temporary switching events are unimportant and do not influence the dynamics per se.
Taken together, the computational model presented here, is a suitable toy model to simulate the interaction dynamics and as every model it has its imperfections. Nonetheless, it has been assessed to "exhibit[...] behavior which is remarkably similar to [...] empirical observations" [155].

6. Investigation of bacterial interactions: Competition by toxin production[1]

The simple interaction system of a colicin producing and sensitive bacteria constitutes a manageable model system to study general properties of ecological interactions. Previous studies investigating colicinogenic and susceptible strains of bacteria used this system as a model system for allelopathy [96,97,99,101] and highlighted the importance of interaction parameters such as colicin production cost, toxin effectiveness, and initial strain ratios for the competition outcome. Focusing on the effective interaction parameters, these studies mainly neglected microscopic details of the interaction mechanisms. While some theoretical studies included the phenotypic variation in modeling the interaction [25], the explicit consideration of how heterogeneity and stochasticity in colicin production affect competition outcome and C strain success was largely unexplored.
In order to fill this gap in knowledge, the two-strain interaction between C and S was investigated using the multi-scale fluorescence setup (see chapter 3) in combination with the stochastic lattice-based population dynamics model (see chapter 5). The results of this investigation are presented in this chapter.
Taken together, the results revealed that the competition dynamics featured two qualitatively different competition phases. First, stochastic effects in toxin production dynamics and random initial positioning influenced the number of viable C clusters at the colony border. Then, the competition dynamics progressed deterministically according to the degree of division of labor, i.e. the fraction of toxin producer within the C strain, and the number of viable C clusters at the colony edge that resulted from the stochastic initial dynamics.

6.1. Interaction scheme

The interaction between the C and S strain features a complex interaction scheme (Fig. 6.1). The competitive interactions are given by the toxin action of the colicin molecules that kill sensitive cells and the limited access to nutrients that S imposes on C by spatial exclusion. As discussed earlier, toxin production in the C strain is subject

[1] This chapter is largely based on publication [B1]. (Images are partly reused and modified from [141] published under Creative Commons License 4.0 [85])

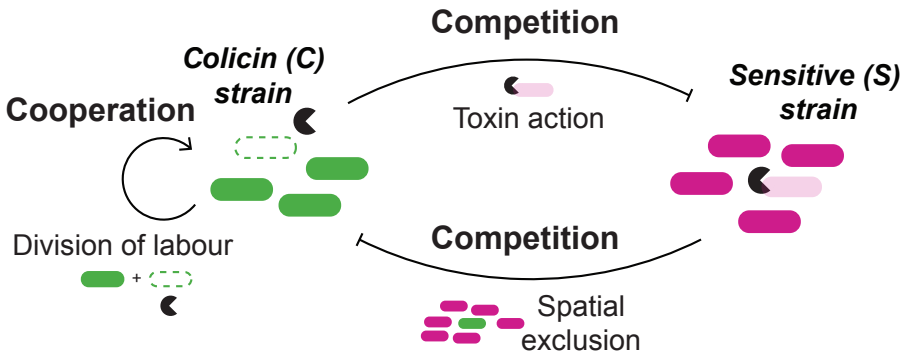

Figure 6.1.: Interactions between the colicion producing and sensitive strain
Interactions between the colicin producing (C) and the sensitive (S) strain are characterized by self-sacrificing toxin production in the C strain which constitutes a intra-species cooperation by division of labor. At the same time, the toxin impact on the S strain is an inter-species competitive action. The S strain exhibits a competitive action on the C strain by excluding it from access to resources.

to phenotypic heterogeneity (see section 2.2) and the simultaneous presence of both phenotypes (toxin-producing and reproducing) represents a division of labor. Taken together, the interaction system is characterized by intra-species cooperation in the C strain and inter-species competition between S and C.
Abstracting from the details of the interactions, the competition outcome depends on effective interaction parameters. While the impact of spatial exclusion depends on the growth rates and initial strain ratios, the toxin action depends on the toxin sensitivity of the S strain and the fraction of toxin producers that can be tuned using an external inducing agent MitomycinC (MitC) [20, 83].
In previous studies similar model systems were investigated in terms of the effective interactions between the competitors. These theoretical studies predicted that given a set of parameters, the outcome of competition was unambiguous and fully determined by initial conditions [97].

6.2. Competition Experiments

In order to study the competition experimentally, mixed bacterial communities of the fluorescently labelled CpMO3 and Srfp strains (see section 3.2.1) were prepared on solid M63 growth medium with an initial C:S ratio of 1:100 by acoustic droplet ejection (see section 3.2.2). This ratio facilitated spatial exclusion and boosted the competitiveness of the S strain. Droplets with inoculum culture measured 2.5 nl in volume and created initial colonies of 450 μm in diameter on the agar surface. The colonies were imaged

using a stereoscopic microscope with a zoom function (see section 3.2.3), which enabled acquisition of time-lapse recordings of the complete competition from the near single-cell level up to mature, macroscopic colonies. The resulting time-lapse recordings were analyzed using customized image and data analysis software (see section 3.3) and yielded traces of the competition dynamics (see Fig. 6.2).

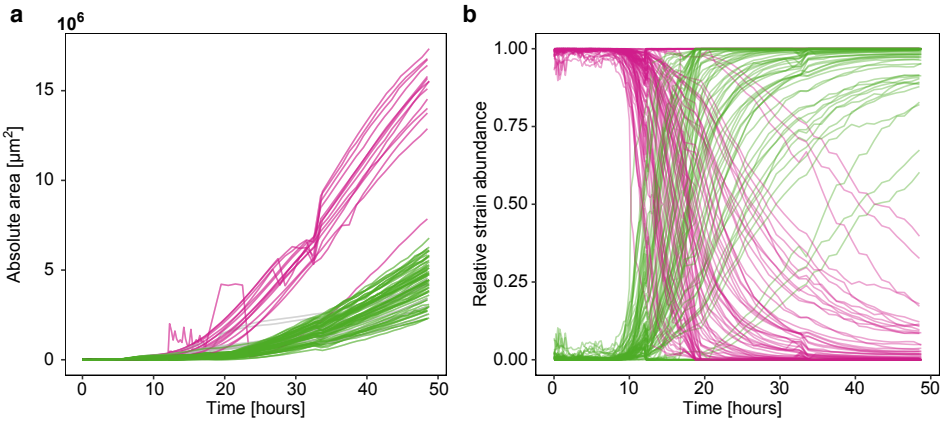

Figure 6.2.: Competition dynamics

a The individual total area curves are obtained in competition experiments and color coded according to the competition outcome (C wins: green, S wins: magenta). **b** Relative strain abundance of two-strain competition is color coded according to the strains (C: green, S: magenta). The curves show the tendency of the C strain (green) to take over the population after prolonged competition. Example traces from competition with 0.005 μg/ml MitC.

6.2.1. Competition outcome

To assess the effect of increasing toxin producer fractions within the C strain on competition outcome and C strain success, range expansion experiments were performed at four different inducer concentrations (0.0, 0.005, 0.01, 0.1 μg/ml MitomycinC). The DNA damaging agent Mitomycin C (MitC) is known to induce the SOS response regulating toxin production and can be used to tune the fraction of toxin producers [20, 83]. Competition outcomes were classified according to the relative area occupied by the strains after 48 hours of competition with A_X^{48h} being the area of strain X after 48 hours. A strain was said to dominate if it occupied over 90% of the colony area; strains were coexisting if both occupied between 10% and 90% of the area; and communities were said to be extinct if the total area amounted to less than $10^6 \mu m^2$. After 48 h of competition, all four distinct outcomes were observed (Fig. 6.3 a). However, the outcome distribution varied strongly with inducer concentration (Fig. 6.3 b) in terms of the final C strain fraction $F_C = A_C^{48h}/(A_C^{48h} + A_S^{48h})$.

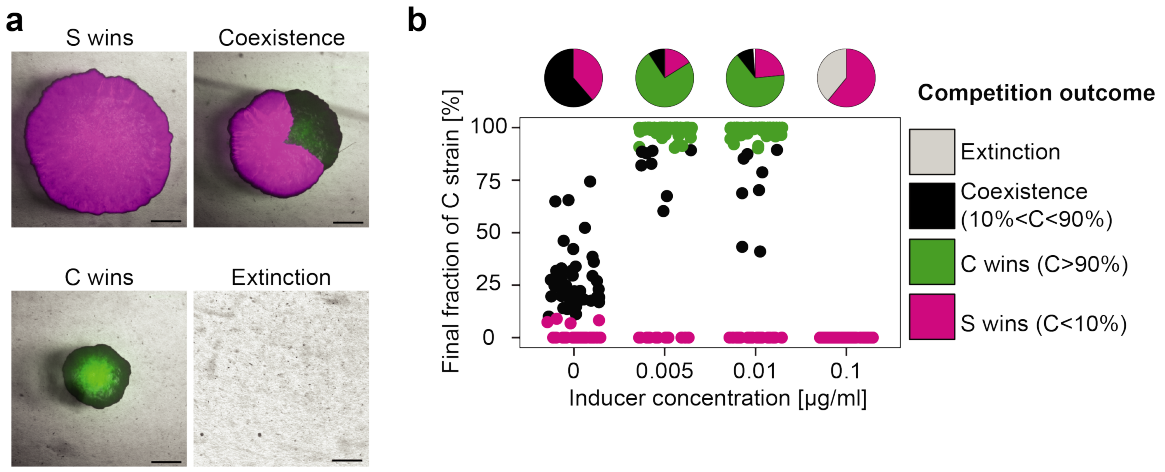

Figure 6.3.: Competition outcome

a After 48 hours of competition, four distinct outcomes were observed. S wins, C wins, coexistence, and extinction. The scale bar represents 1 mm. **b** The final C strain fraction varied with inducer concentration. Individual competition experiments at four inducer concentrations are displayed as dots (lateral spread for better visibility). Depending on the relative strain abundance, the competition outcomes were classified into one of the four classes (see main text for details) and colored here accordingly. The pie charts on top represent the distribution of distinct competition outcomes for each condition. Without external inducer (0.0 μg/ml), the competition mainly resulted in S success or coexistence. At intermediate inducer concentrations (0.005 & 0.01 μg/ml), the outcome distribution became bimodal occupying S success as well as C success regions. For high induction (0.1 μg/ml), C success declined and colonies were dominated by S or went completely extinct.

Surprisingly, for each competition condition there was no single unique outcome and only main outcomes could be described. Without external inducer, either S dominated, or the two strains coexisted. At low inducer concentrations (0.005 & 0.01 μg/ml MitC), C mostly dominated, while at high inducer concentrations (0.1 μg/ml MitC) C perished, and one observed either S domination or extinction of both strains.
These results have two main implications. First, the C strain was most successful at intermediate inducer concentrations which indicates an optimum toxin producer fraction at which the trade-off between toxin benefit and production cost is balanced. Second, despite the clear differences in outcome distributions between conditions, an unexpectedly large variation within the distributions was observed. Under similar initial conditions (the same inducer concentration) multiple outcomes were observed, which will be referred to as multi-stability.
In order to gain a better understanding of these two effects, the competition dynamics were analyzed in more detail. First focusing on the deterministic dynamics and then on stochastic effects.

6.3. Deterministic competition

Experimental time-lapse data as well as computational modeling was used to investigate competition parameters that govern the deterministic dynamics: growth rate, toxin producer fraction within the C strain, and toxin sensitivity [97].

6.3.1. Experimental competition parameters: Growth rate and toxin producer fraction

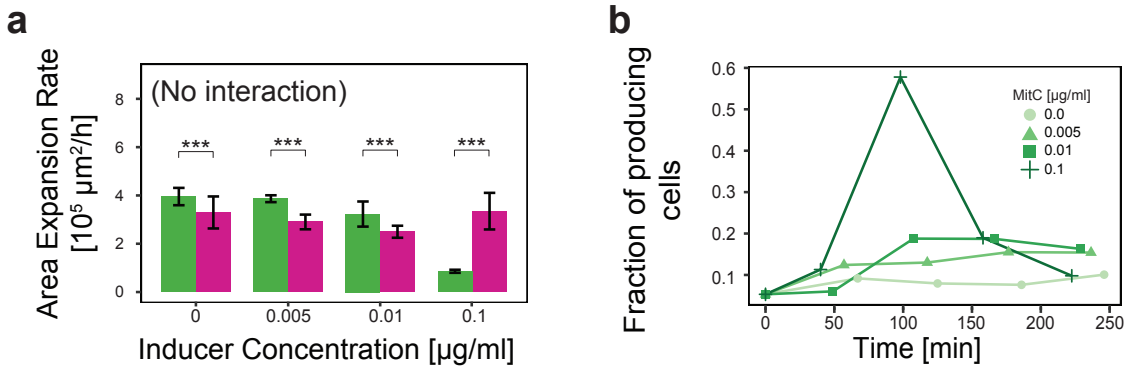

Figure 6.4.: Competition parameters

a The strain specific growth rate in terms of area expansion rate for C (green) and S strain (magenta) did not vary much between inducer concentrations except for high induction which considerably reduces C growth (*** denotes significance with $p < 0.001$). **b** The fraction of toxin producers within the C strain was determined analyzing the fluorescence of toxin expressing cells using a high resolution microscopy setup (see section 3.5). For different inducer concentrations, the population response clearly differed. The color code indicates the inducer concentration.

In a first step, the growth rates (area expansion rates) were analyzed using linear regression in the linear growth regime (see section 5.3.5). Comparing the growth rates for the two strains without and at low induction revealed growth rates that were in accordance to previous studies [25], and a S:C growth rate ratio of $78.6 \pm 6.6\%$ that was constant within the error range for inducer concentrations 0.0-0.01 μg/ml MitC (see Fig. 6.4 a). At high induction, however, C's growth rate was significantly lower compared to the other conditions due to increased cell lysis accompanying toxin production, while the S strain was not significantly slower compared to the uninduced case.
The stable growth rate ratio excluded pure growth rate effects from being responsible for the observed success of the C strain at intermediate inducer concentrations. Consequently, the dependence of the second parameter, producer fraction within the C strain

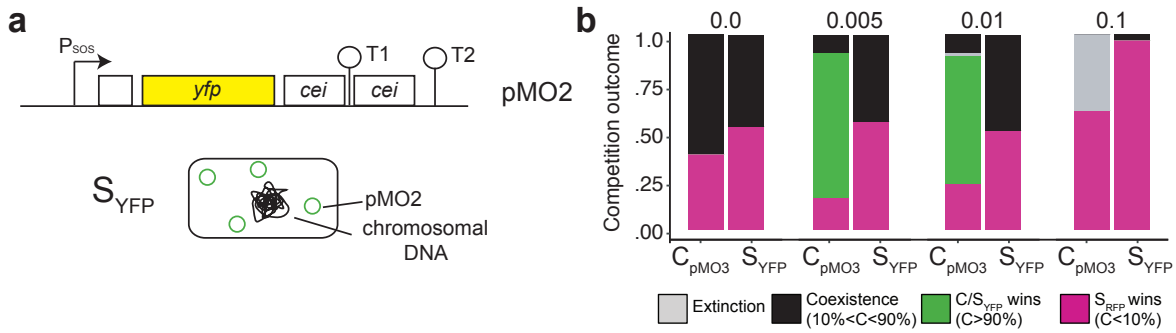

Figure 6.5.: Alternative competition scenario without toxin release
a The plasmid pMO2 carries the colicin operion in which the *cea* gene is replaced by a *yfp* gene. The transformation of pMO2 into the S wild type strain yields the S_{YFP} strain that lyses in response to SOS activation but is unable to release any toxin. **b** Competition outcome comparison shows that S_{YFP} (right) performs worse compared to C_{pMO3} (left) in competition with the S_{RFP} strain due to missing toxin action.

population, on MitC concentration was investigated.
As discussed earlier, the response dynamics of single cells to SOS stress (by MitC) have been investigated previously in liquid conditions using time-lapse microscopy [20]. The individual single cell dynamics led to a collective response that was strongest 75 min after induction and was found to increase with the external stress level (see section 2.2). In order to verify that these results were also valid under the experimental conditions of the competition experiments on solid growth media, the degree of phenotypic heterogeneity was assessed using high-resolution microscopy (see 3.5). The results on solid growth medium were qualitatively similar, although lower inducer concentrations yielded similar results compared to liquid conditions (Fig. 6.4 b). Without external inducer a low but steady producer fraction ($7.0 \pm 1.5\%$) was detected. At low inducer concentrations, the mean producer fraction increased to $14.5 \pm 1.9\%$ (average of 0.005 and 0.01 μg/ml MitC conditions) over the time-course of the experiment and stayed relatively constant. At high induction (0.1 μg/ml MitC), however, a synchronized response peaking at $57.8 \pm 3.2\%$ toxin producers was observed, followed by a collective decrease due to cell lysis.
Applying the phenomenological model from chapter 4, this behavior can be interpreted as the inducer setting the switching rate s and thereby altering the steady state of toxin producers $\frac{s}{r+d}$. Without external inducer, the producer fraction stays constant. At low induction, the population can settle to the new steady state. At high induction, however, the switching rate is so large that the switching process eventually drives the system to the absorbing boundary $C_{OFF} = C_{ON} = 0$.

To further support the hypothesis that indeed toxin production was responsible for the success of the C strain at intermediate producer fraction, competition experiments were performed in which the C strain was replaced by the S_{YFP} strain unable to produce

the toxin. This S_{YFP} strain contained the colicin E2 operon in which the *cea* gene was replaced by a *yfp* gene on the pMO2 plasmid (see Fig. 6.5 a). Consequently, it was able to produce the Cei and Cel proteins upon SOS response but without any toxin released upon lysis. The qualitative competition results (Fig. 6.5 b) clearly showed that in contrast to the C strain, the non-toxic mutant was unable to dominate over the S_{RFP} strain, although it was even faster in growth (see table A.2 in the appendix). This further supported the hypothesis that the observed shift in competition outcome distribution with varying inducer concentration was due to the change in toxin-producer fraction.
Taken together, at intermediate inducer concentration, there was no significant decrease in growth rate compared to the uninduced case, i.e. the cost of toxin production for the C is sufficiently low. Nonetheless, the increase in toxin producer fraction already created a sufficiently large toxin action on the S strain such that C could succeed. At high induction however, the production cost was too high and a prolonged toxin benefit could not be established. Therefore, it was hypothesized that only varying the toxin producer fraction should be sufficient to alter the overall competition outcome. In order to investigate the sole influence of a variation of toxin producer fraction without any distorting effects, the computational model (chapter 5) was applied to the C-S interaction.

6.3.2. Simulation parameters: Switching rate, toxin sensitivity/effectivity, and growth rate

In addition to the experiments, the computational model presented in chapter 5 was used to simulate to competition dynamics. For each condition a set of replicate simulations was performed. One result of the experimental analysis was that the fraction of toxin producers was mainly responsible for the observed shift in competition outcome with varied inducer concentration. In order to corroborate these findings, the simulations were performed for a range of switching rates s_C that determined the fraction of toxin producers[2]. Due to the close relation between s_C and the fraction of toxin producers, both terms are used interchangeably.

However, while the growth rates r_C and r_S for both strains and the lysis rate $d_{C_{ON}}$ of the C_{ON} state were known, one remaining free parameter was the toxin sensitivity s_S which was hard to determine experimentally. The parameter s_S combines the toxin effectivity and toxin sensitivity of the susceptible strain S and is therefore interchangeably called toxin effectivity depending on the focus. In order to take into account its effect, s_S was varied in addition to s_C simultaneously. As a first result, it is worth not-

[2] Please note that in the simulations for this chapter, a different functional relationship between toxin producer fraction and s_C was used compared to the definition from chapter 4. $Frac_{SS} = \frac{C_{ON}}{C_{ON}+C_{OFF}} = \frac{s/d}{1+s/d}$ However, this did not change the simulation results qualitatively.

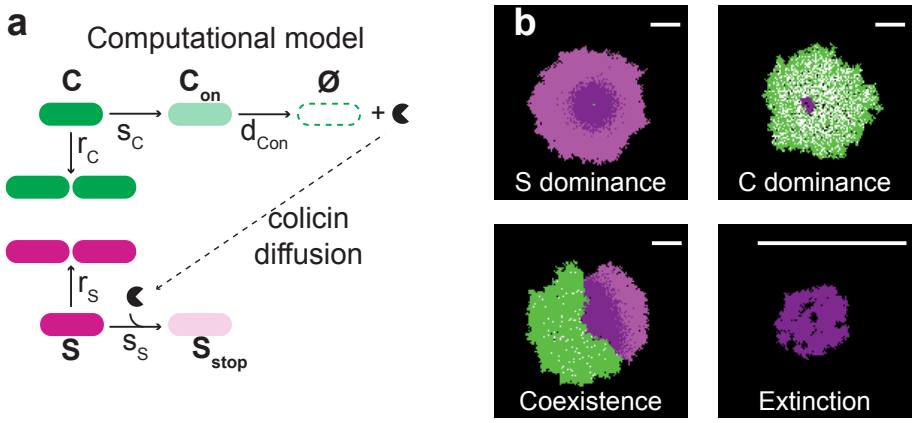

Figure 6.6.: Computational model

a The computational model featured reproduction and state switch reactions of both C (green) and S (magenta) strain as well as lysis of the C_{ON} strain. See chapter 5 for details[3]. **b** The model could reproduce the four distinct competition outcomes taking into account S (bright magenta), S_{stop} (dark magenta), C (green), and C_{ON} (white) cells. The scale bar corresponds to 1 mm on the computational grid.

ing that the computational model was able to reproduce the four different experimental competition outcomes (Fig. 6.6 b).

The system was simulated for a range of s_C and s_S values, generating phase diagrams for each of the four competition outcomes (see Fig. 6.7). Dominance of the C strain was maintained for a broad range of toxin effectivities s_S for intermediate inducer concentrations. Accordingly, S dominance was most prominent under conditions in which C failed. Similarly, coexistence was mostly found in regions, in which C could not dominate: at low toxin producer fractions or low toxin effectivity. Extinction events occurred under conditions in which toxin is effective and prolonged toxin production is ensured. Despite the capability of the model to generate extinction outcomes, it could not reproduce the high incidence of extinction events seen in experiments at high inducer levels. A more detailed model taking into account synchronous toxin responses was able to generate high extinction probabilities. However this will not be discussed in this thesis and the interested reader is referred to the original publication [141].

By comparing the competition outcome of experiments (see Fig. 6.3) and simulations (see Fig. 6.8 a), the free toxin effectivity parameter of the simulation was fixed to $s_S = 1500$. Then focusing on the exclusive variation of the switching rate s_C, the simulations underlined that only varying the switching rate was sufficient to explain the observed changes in outcome distribution. This will be discussed in more detail in the following.

[3] The death reaction of growth inhibited S_{Stop} cells was considered in the simulation but with a negligible rate and therefore not shown in the scheme.

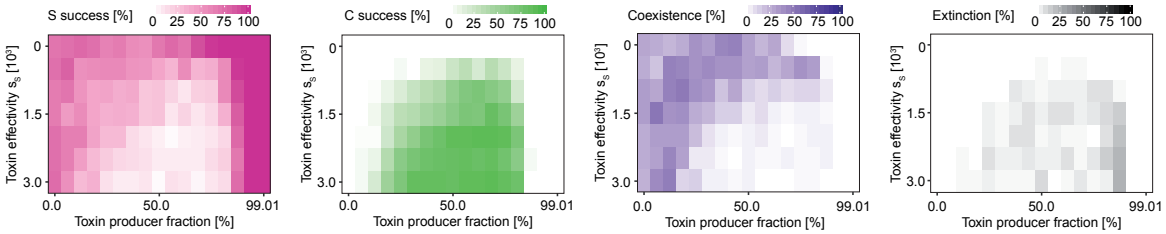

Figure 6.7.: Toxin effectivity s_S and switching rate s_C parameter variation
The phase diagram for the simultaneous s_C and s_S parameter variation shows the outcome probability for the four outcomes S and C domination, coexistence, and extinction.

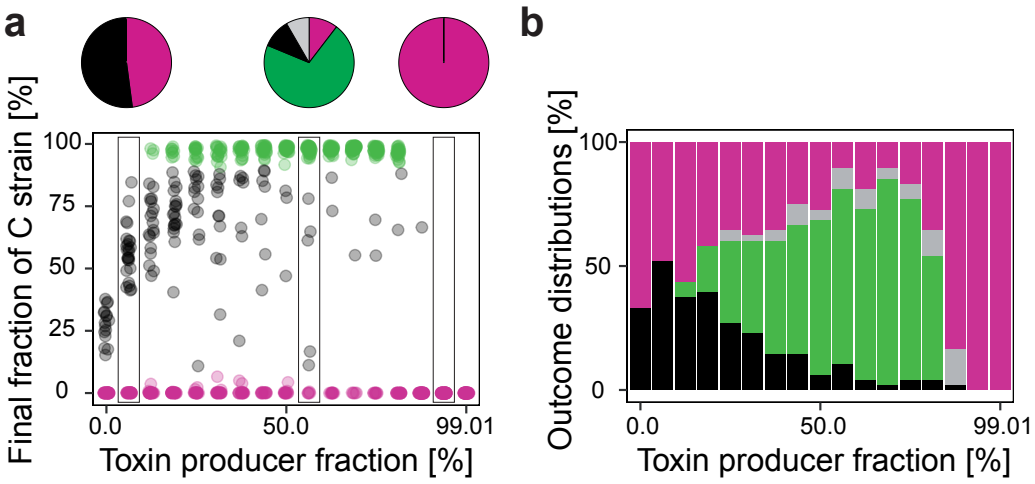

Figure 6.8.: Outcomes of switching rate variation for constant $s_S = 1500$
a The final C strain abundance changes with increasing producer fraction, determined by the switching rate, similar to experiments. **b** Translating the C strain abundance into distinct outcomes, the change in outcome distribution is even more evident. Color code as in Fig. 6.3 b.

By increasing s_C and keeping s_S constant (1500), which is the computational equivalent of increasing the inducer concentration, qualitative changes similar to the experimentally obtained ones could be observed (Fig. 6.8 a). At low and very high s_C values, domination of the C strain could not be observed, while C was successful for intermediate s_C values. In particular, at approximately half of the C population producing the toxin, mostly C dominance was found (see Fig. 6.8 a, middle boxed outcome distribution). However, similar to the experiments the presence of the three other competition outcomes was conserved. The classification into distinct outcomes (see Fig. 6.8 b) made

it even more evident: C domination was only found at intermediate inducer concentrations, i.e. balanced division of labor.
Finally, the computational model was used to assess the influence of a change in relative growth rate of the strains. To this end, the growth rate of the competitor (S) strain was systematically varied and expressed in terms of the growth rate r_C of the C strain. By simultaneously varying the toxin sensitivity s_S of the competitor, two dimensional outcome phase diagrams could be obtained (Fig. 6.9). The phase diagrams showed a diagonal area of coexistence that divided the regions in which mainly C or S dominate. This diagonal represented a trade-off between growth rate and sensitivity. Below the separating region, strains were sensitive and slow, and consequently succumbed to the toxin producer (see highlighted square S_{RFP}). However, being equally sensitive but faster in growth enabled it to cross the diagonal thereby overcoming the toxin action and to thrive in competition (see highlighted square S_{NFP}).

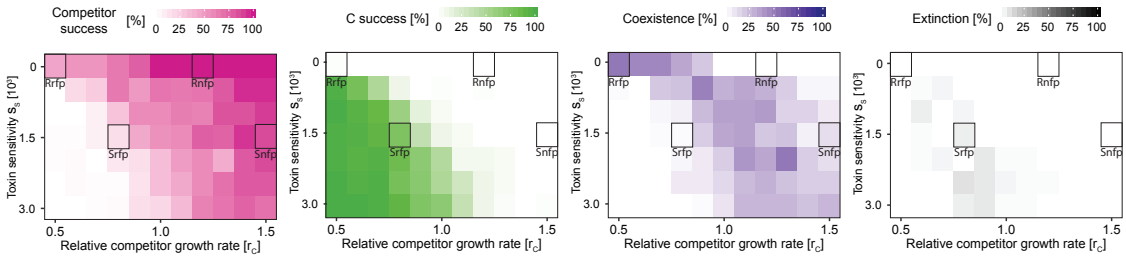

Figure 6.9.: Toxin sensitivity s_S and competitor (S) growth rate r_S parameter variation
The growth rate of the competitor (S) strain was varied and is expressed in terms of the C growth rate r_C.

Conclusion

Taken together, the theoretical model allowed to investigate various competition parameters: switching rate s_C, toxin effectivity / sensitivity s_S, and growth rate r_S. The most important result was that only varying the switching rate and thereby the toxin producer fraction within the C strain population was enough to reproduce the experimentally observed shift in outcome distribution. The explanation for this effect is a balanced division of labor between toxin production and reproduction which is only successful at intermediate levels.
Furthermore, the computational model allowed exploration of experimentally inaccessible parameter combinations that yielded outcome phase diagrams. In particular the simulations allowed to draw conclusions on how the system changes if only one of the parameters was changed while the others are kept constant (see Fig. 6.10). Focusing on

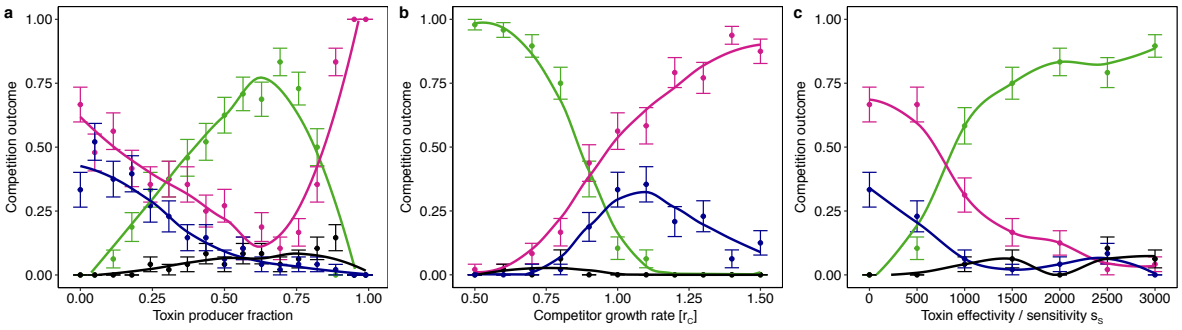

Figure 6.10.: The effect of simulation parameter variation on competition outcome
The effect of the variation of the toxin producer fraction via switching rate (**a**), the competitor growth rate r_S (**b**), and toxin effectivity/ sensitivity s_S (**c**) on the competition outcome of simulations is displayed for the four different outcomes: C success (green), S success (magenta), coexistence (blue), and extinction (black). Points denote average values of competition outcome for 48 simulation replicates, error bars denote standard error the mean, and the lines are polynomial splines as guide for the eye. Simulation conditions: **a**: $r_C = 0.0729$, $r_S = 0.0607$, $s_S = 1500$, s_C varied. **b**: $r_C = 0.0729$, r_S varied, $s_S = 1500$, $s_C = 0.015$. **c**: $r_C = 0.0729$, $r_S = 0.8\,r_C$, s_S varied, $s_C = 0.015$.

the C strain, the optimum behavior of the producer fraction manifested in an inverted u-shaped relation (Fig. 6.10 a). With increasing competitor growth rate, C's success declined (Fig. 6.10 b), while C became more successful with higher toxin effectivity/ sensitivity (Fig. 6.10 c). The behavior of the S strain followed the opposite trend and coexistence was found in regions in which neither S nor C were completely advantageous.
After exploring the parameter space of the model, the question arose how well the predicted competition outcomes reflect the actual dynamics. These will be answered in the next section.

6.3.3. Testing predictions: Alternative competition scenarios

In order to test the computational predictions, competition experiments were performed using alternative competition scenarios. The parameters could only in part be extracted directly from experiments; the two strain growth rates r_C and r_S from competition control experiments and the lysis rate $d_{C_{ON}}$ from single cell studies. However, other parameters, such as toxin sensitivity and switching rate, were calibrated by comparing experimental and simulation results.
Once the system was calibrated such that $s_S = 1500$ and $s_C = 0.015$ delivered results similar to the experiments with 0.005μg/ml MitC[4], the combined r_S and s_S parameter variation could be used as an experimentally testable prediction.
By performing the competition experiments with three alternative competitor strains that varied in both toxin sensitivity and growth rate from the original competitor strain S_{RFP}, the generality of the model could be assessed. To this end, competition of the C and the alternative competitor strain X, $X \in \{S_{NFP}, R_{NFP}, R_{RFP}\}$, was performed at 0.005$\mu$g/ml MitC as outlined before. The growth rates of the strains were determined by linear fitting in the linear area growth regime and assuming linear relations between area growth and simulations growth rate (see section 5.3.5 and table A.2) and are depicted in Fig. 6.11 a. Growth rate differences arose through the costly expression of red fluorescent protein (RFP) compared to no fluorescing protein (NFP). Resistance was generated by selection of sensitive strains in presence of Colicin [166] and involves a reproduction cost as well. Knowing the growth rates and the toxin sensitivities ($s_{S_{RFP}} = s_{S_{NFP}} = 1500$ and $s_{R_{RFP}} = s_{R_{NFP}} = 0$), the simulated competition outcomes could be extracted from the phase diagrams (Fig. 6.9; highlighted rectangles correspond to the competitor strains).
The predicted competition outcomes could then be compared to the experimentally observed ones. Figure 6.11 b summarizes the competitor properties and compares simulated and experimental competition outcomes.
Overall, these data show that the model predictions were in good agreement with the experimental results. Depending on the properties of the competitor X, the competition of C and X differed from the original competition of C and S_{RFP}. As predicted by the simulations, a boost in competitor growth rate considerably improved S_{NFP}'s competition strategy of spatial exclusion and led to much higher S dominance and a large decrease in C dominance. Turning off the toxin action (resistant strains R_{RFP} and R_{NFP}) prevented large scale dominance of the C strain. Depending on the growth rate, the competitor could dominate completely (R_{NFP}) or the outcome distribution featured a mix of competitor domination and coexistence (R_{RFP}).

[4] Using the explicit formula for toxin producer fraction and the rates $s_C = 0.015$, $r_C = 0.0729$, and $d_{C_{ON}} = 0.02$ the simulated toxin producer fraction $f = \frac{s_C}{r_C + d_{C_{ON}}} = 16.1\%$ is remarkably similar to the measured fraction $f_{exp} = 14.9 \pm 1.9\%$.

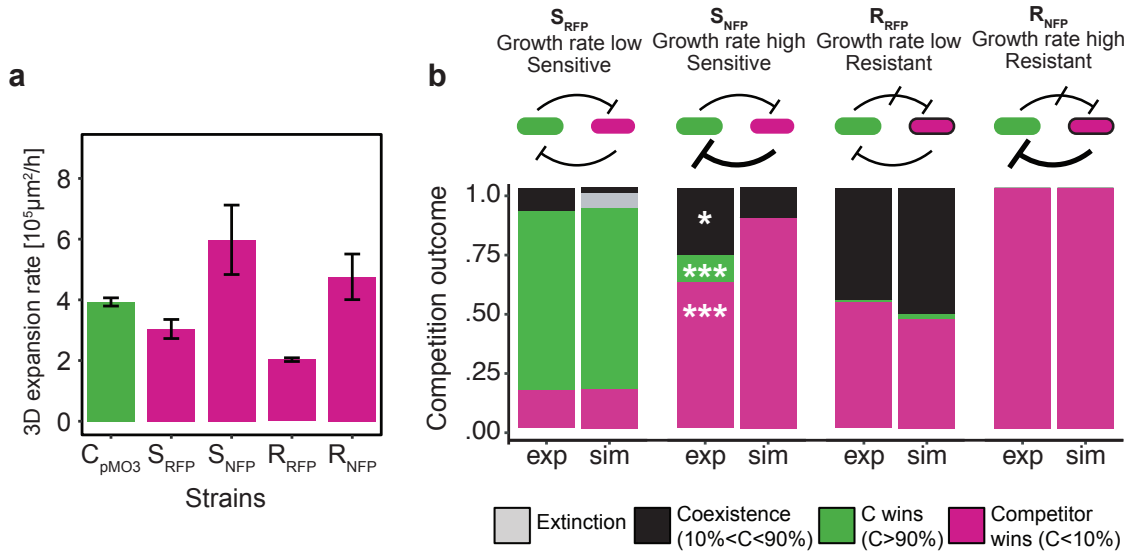

Figure 6.11.: Alternative interaction scenarios in experiment and simulation
a Area expansion rates for the various strains involved in interactions measured at 0.005μg/ml MitC. **b** Top row summarizes interaction scenarios and competitor properties. Outcome distributions for experiments (left) and simulations (right) are depicted as stacked bar plots in which the color indicates the respective outcome (see legend below). Significant differences for a certain outcome type are indicated by asterisks (significance level ***:p<0.001, *:p<0.05). Experiments were performed at 0.005μg/ml MitC. Simulation parameters: $r_C = 0.0729$, $s_C = 0.015$; r_X, s_X chosen in accordance to experimental rates (see also Fig. 6.9). Sample sizes for experiments are 87, 108, 108, 128 (from left to right) for experiments and 48 each for simulations.

In particular two of the three alternative scenarios showed very good agreement of prediction and experiments (insignificant differences). And even in the case in which significant differences were observed (S_{NFP}), the general trend of a majority of S dominance cases was reproduced [5]. This might be due to the intricate interplay between growth and toxin processes which could have been harder to predict than pure growth processes found in the scenarios with the resistant R strains. Furthermore, the S_{NFP} growth rate featured the largest experimental variance. An overestimated S_{NFP} growth rate could explain the observed deviation.
Taken together, the alternative competition scenarios demonstrated that changes in interaction parameters really alter the outcome of competitions and enabled testing of the simulated predictions. Overall, simulations and experiments agree well and underline the generality of the proposed model.

[5] The difference between experimental and simulated outcome proportion was tested for significance using t-tests. To this end, random samples were generated with corresponding mean, variance and sample size. The variance for the sample proportion was calculated according to [167] p 102.

6.3.4. Conclusion of deterministic competition

By accessing the competition parameters experimentally and simulating the competition, the deterministic factors influencing the competition were analyzed. In particular, the results revealed that the C strain is only dominant at balanced division of labor (intermediate toxin producer fractions) and that its success probability increased with increasing relative growth rate and toxin effectivity / sensitivity. Furthermore, the model was tested with alternative competition scenarios and proved to be in good agreement to experiments. However, up to now, the results did not explain the observed multi-stability of competition outcomes, i.e. why did one observe the presence of S dominance cases at intermediate inducer concentration, at which the C strain should have dominated. This question will be addressed in the next section.

6.4. Stochasticity in positioning and toxin dynamics

Up to now, the detailed analysis of the competition parameters gave no insight into the origin of multistability in this system. However, one knows that toxin dynamics itself are stochastic (see chapter 4) and there certainly is a large proportion of stochasticity involved in the initial positioning of cells by the droplet deposition. Consequently, the competition experiments were analyzed in more detail.
Figure 6.12 compares two competition experiments under similar conditions, i.e. both experiments were performed with 0.005 μg/ml MitC and initially featured three C cells (highlighted in green). In case a, all three cells switched to the toxin producing state early and lysed subsequently, giving way for S domination. However, in case b, only the two lower cells produced the toxin and lysed early, thereby killing many S cells in their vicinity, while the upper cell reproduced to form a viable C cluster which took over during the course of the experiment. Taken together, while both experiments started under very similar conditions, stochasticity in toxin dynamics led to two completely different outcomes.

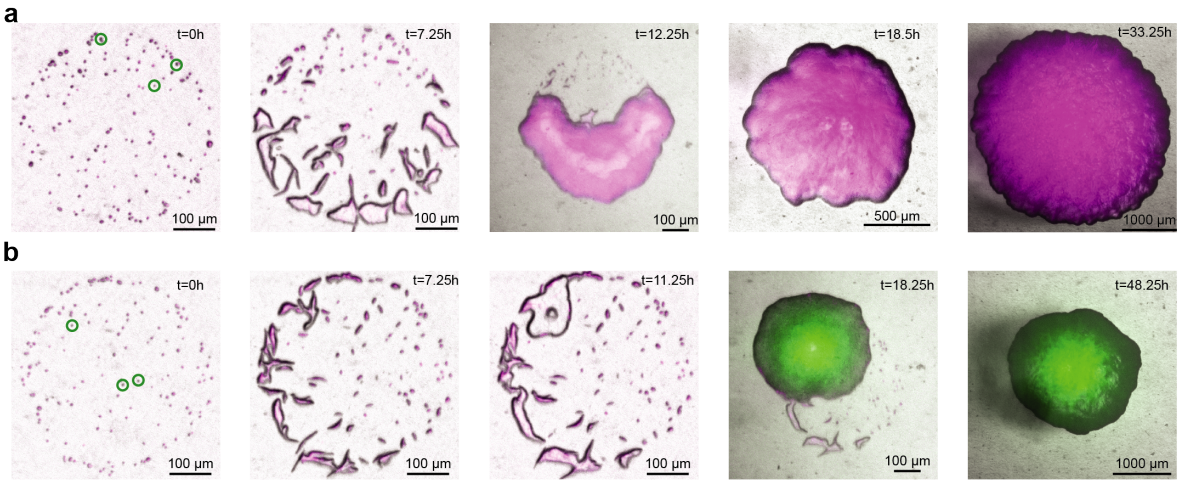

Figure 6.12.: Comparison of two competition experiments under similar conditions
The following two scenarios feature competitions under similar conditions. Both experiments were performed under 0.005μg/ml MitC, and both contained three initial C cells (highlighted with green circles in left image). However, while in case **a**, all three cells lysed giving the way for S domination, in case **b**, one cell formed a viable C cluster which took over the population during the course of the competition. Please note the variable scale bar indicating the zoom.

This motivated the following hypothesis of two phases of interaction (see Fig. 6.13). First, in phase 1, stochastic effects in positioning and toxin dynamics shape early com-

munity composition. Then, in phase 2, at sufficiently high cell numbers, the dynamics are mainly driven by the deterministic competition parameters. In this section, the stochastic effects in competition will be investigated in more detail thereby disentangling deterministic and stochastic effects.

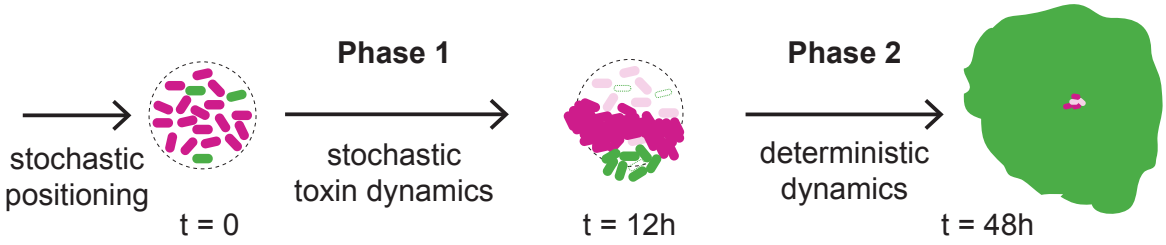

Figure 6.13.: Two phases of interaction
Experimental findings motivated a two-phase competition model. In an early phase, stochastic effects in positioning and toxin dynamics are hypothesized to shape the community at low cell numbers. Later, at high cell numbers, the dynamics are driven by the deterministic interaction parameters. Schematic example shows a surviving C cluster colony that competes under favorable conditions and takes over the colony.

6.4.1. Stochasticity in positioning and phase 1 dynamics

Initial positioning fails to explain competition outcome variability

As a first step, the initial distribution of C cells was determined in an semi-automatic fashion. Since C cells do not emit a fluorescence signal in the OFF state, they are hard to detect automatically. Therefore, exploiting the time-lapse information, initial C cells were identified based on missing RFP signal, visible toxin action, and later growth. In this assessment method, there certainly is a high degree of survival bias involved because cells that had a larger impact were more likely to be detected. However, for the remainder of the discussion this problem will be neglected.
Knowing the positions of the initial C cells i with respect to the colony center $\mathbf{x}_{C,0,i}$ allowed the calculation of three variables describing the initial positioning. First, the numbers of C cells $N_{C,0}$ was simply the summation of individual cells in a given experiment (spot). Second, the average distance from the colony center was calculated using:

$$R_{C,0} = |\mathbf{x}_{C,0}| = |\frac{1}{N_{C,0}} \sum_{i=1}^{N_{C,0}} \mathbf{x}_{C,0,i}| \tag{6.1}$$

Third, to account for the dispersal over the initial colony, the spread of the C cells was determined by:

$$D_{C,0} = \frac{1}{N_{C,0}} \sum_{i=1}^{N_{C,0}} (\mathbf{x}_{C,0,\,i} - \mathbf{x}_{C,0}) \tag{6.2}$$

In order to quantify the influence of these positioning variables on the competition outcome, the competition outcome was parametrized by the final C strain abundance F_C.

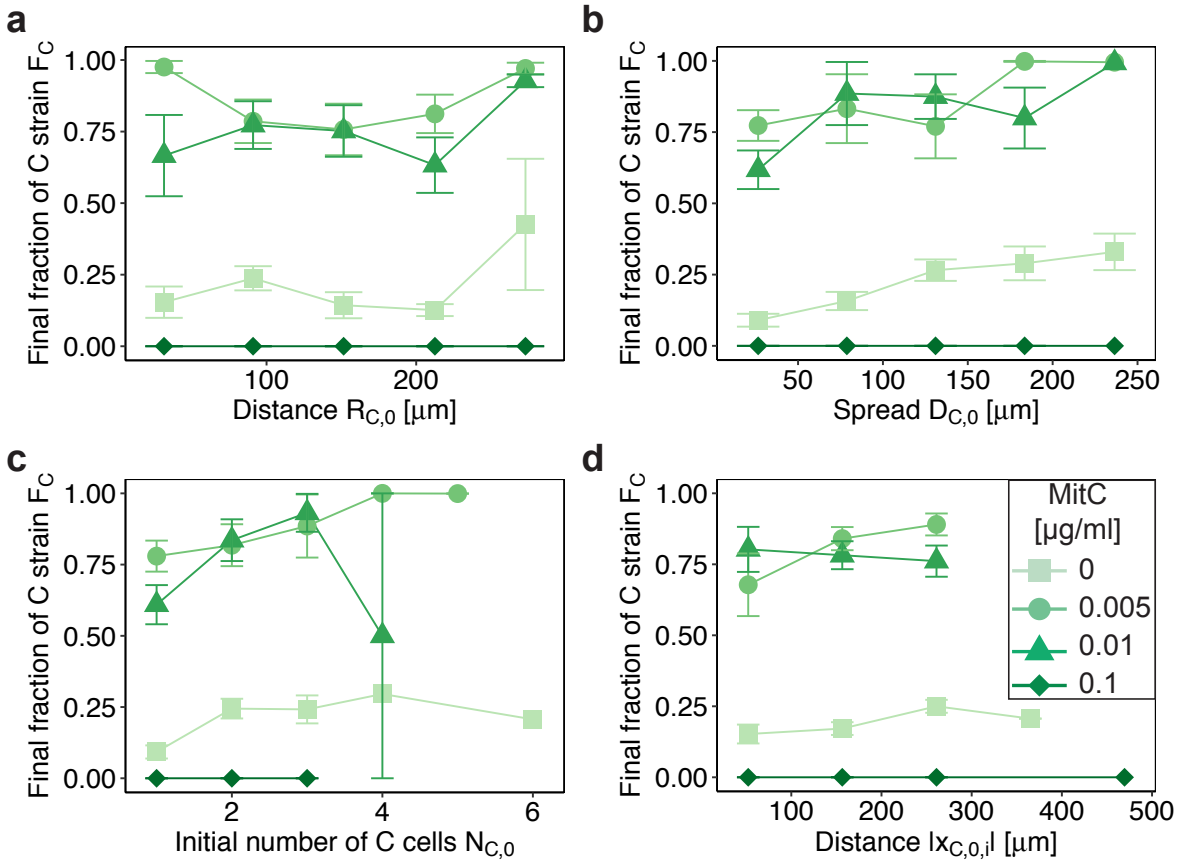

Figure 6.14.: Positioning parameters do not influence F_C

The center of mass distance from the colony center $R_{C,0}$ (**a**), the spread $D_{C,0}$ (**b**), and the number of initial C cells $N_{C,0}$ (**c**), as well as individual cells' radial positions $|\mathbf{x}_{C,0,\,i}|$ (**d**) do not strongly affect final C strain fraction. The color code represents inducer concentration and is given in **d**.

While the influence of the inducer concentration on the final C strain fraction was evident for all variables, the spatial parameters itself only very weakly influence the final outcome (see Fig. 6.14). The average distance from the colony center $R_{C,0}$ did not influence the final C strain fraction (Fig. 6.14 a), which might be explained by cancelling effects of oppositely placed initial C cells. This cancelling effect was prevented by the

spread variable $D_{C,0}$ representing the distribution over the initial colony which itself did not influence the competition strongly (Fig. 6.14 b). The same was true for the number of initial C cells $N_{C,0}$ which drove the final C strain fraction only weakly (Fig. 6.14 c). Also on the level of individual cells, the individual distance from the colony center did not influences the competition outcome.
In order to quantify these effects, the correlation between F_C and the positioning variables was calculated. In accordance to Fig. 6.14, all of the the spatial variables $N_{C,0}$, $R_{C,0}$, and $D_{C,0}$ and individual cells' radial positions $|\mathbf{x}_{C,0,i}|$ are not correlated to the competition outcome (Pearson's r <0.2). Taken together, the randomness in initial positioning did not explain the observed variability in competition outcome.

Initial positioning and stochastic toxin dynamics determine the number of C edge clusters

The failure of the spatial variables to explain the variability in competition outcome motivated the search fo another variable that includes the stochasticity in toxin dynamics in early competition. Consequently, the initial C cells were further characterized regarding their time-point of switching into the toxin producing state t_{Switch}[6] and their position at the end of phase 1 (12 hours)[7]. The position at the end of phase 1 could take one of two values depending whether it was at the edge of a colony or not.
The resulting variable $N_{C,Edge}$, the number of viable C clusters at the colony edge after 12 hours for a given competition spot, was found to be the most important factor in determining the competition outcome in addition to the deterministic parameter of toxin producer fraction. In section 6.4.2, it will be discussed how these two variables determine competition phase 2. Before that, the influence of the various positioning parameters, such as $N_{C,0}$, $R_{C,0}$, $D_{C,0}$, and the inducer concentration on the formation of edge clusters will be investigated.
The influence of the inducer concentration on the edge cluster formation was not as pronounced compared to its effect on the final C strain fraction (Fig. 6.14). While under highly induced conditions, the positioning variables still did not influence $N_{C,Edge}$, the other three inducer concentrations showed relatively similar behavior (Fig. 6.15). Similar to its effect on F_C, the average distance $R_{C,0}$ did not strongly drive the number of viable C edge clusters (Fig. 6.15 a). Instead, the dispersal of C cells over the intial colony $D_{C,0}$ led to an increase in $N_{C,Edge}$ (Fig. 6.15 b). Furthermore, with increasing initial C cells $N_{C,0}$, the number of viable C edge clusters rose as well (Fig. 6.15 c). Finally, even the radial distance of individual cells $|\mathbf{x}_{C,0,i}|$ was positively correlated with

[6] Cells that reproduced and formed viable clusters were assigned the value 48 hours.
[7] The duration of 12 hours for the initial phase was arbitrarily chosen. This time-point simply coincided with a change in zoom level and was therefore the last time-point at highest magnification.

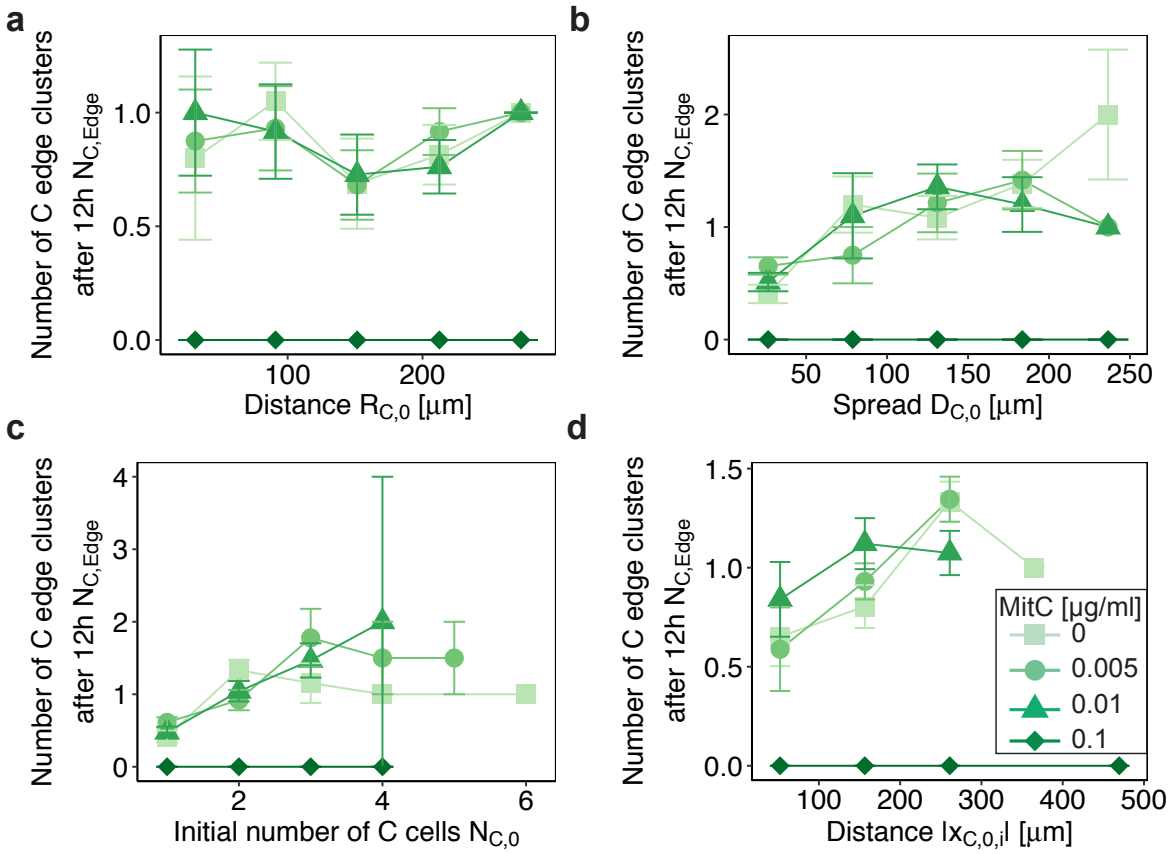

Figure 6.15.: Positioning parameters influence $N_{C,Edge}$
The center of mass distance from the colony center $R_{C,0}$ (**a**), the spread $D_{C,0}$ (**b**), and the number of initial C cells $N_{C,0}$ (**c**), as well as individual cells' radial positions $|\mathbf{x}_{C,0,i}|$ (**d**) influenced the number of C edge clusters after 12 hours $N_{C,Edge}$. The color code represents inducer concentration and is given in **d**.

$N_{C,Edge}$ (Fig. 6.15 d).

To formally analyse the influence of the various positioning parameters, such as $N_{C,0}$, $R_{C,0}$, $D_{C,0}$, and the inducer concentration, a linear statistical model was used.

$$N_{C,Edge} = \beta_1 N_{C,0} + \beta_2 R_{C,0} + \beta_3 D_{C,0} + \beta_4 [MitC] \tag{6.3}$$

The model returned highly significant contributions from all four variables with positive slopes for $N_{C,0}$, $R_{C,0}$, and $D_{C,0}$ and a negative slope for $[MitC]$ (see table A.3 for details). Such statistical models give valuable insights into the general trends, however, they neglect any underlying physical relations.

In order to investigate the effect of stochasticity in toxin dynamics on the formation of viable C edge clusters $N_{C,Edge}$, the population dynamics model for the toxin producer population discussed in chapter 4 was used. There, it was shown how stochasticity in toxin production leads to the extinction of small populations. The survival probability

of a given community with $N_{C,0}$ initial C cells was determined to equal

$$S = 1 - E^{N_{C,0}} \tag{6.4}$$

where the single cell death probability was given by $E = \frac{s_C}{r_C}$.
This single cell death probability could be also determined empirically from the competition data as the ratio of cells that produced the toxin and died in the first 12 hours $T = \sum_{\text{Spots } j} \sum_{\text{Cells } i} \theta(12h - t_{\text{Switch},(j,i)})$[8] and the total number of initial C cells $N = \sum_{\text{Spots } j} N_{C,0,j}$.

$$E = \frac{T}{N} \tag{6.5}$$

The number of C edge clusters should be proportional to the survival probability $N_{C,Edge} \propto S$. And indeed, by relating the number of edge clusters $N_{C,Edge}$ to the initial C cell number $N_{C,0}$, one could find a relationship that resembled the theoretically derived relation for the survival probability (data for intermediate inducer concentration shown in Fig. 6.16 b). Here, the blue straight line is a fit to the data with functional relation $N_{C,Edge} = \alpha \cdot (1 - E^{N_{C,0}})$ in which $E = 34.6\%$[9] that was determined according to eq. 6.5, and α was a free proportionality factor.

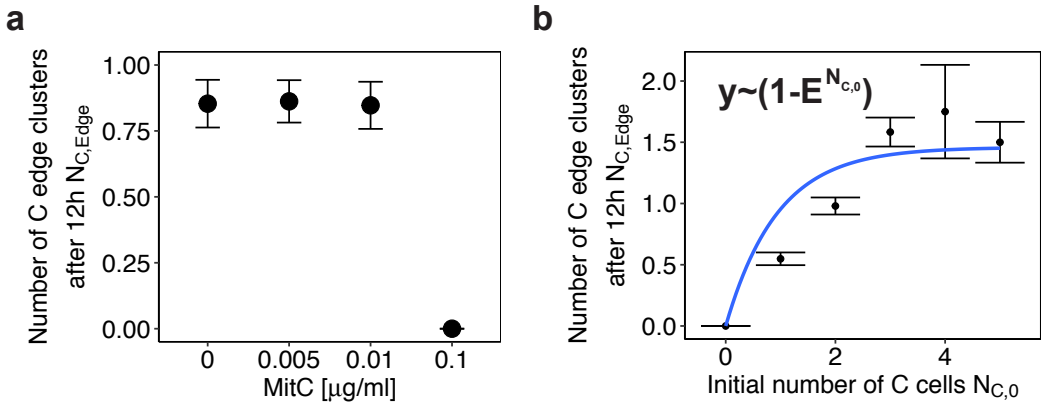

Figure 6.16.: Extinction probability and $N_{C,Edge}$

a At low and intermediate toxin producer fractions, the average number of C edge cluster did not vary much. At high induction however, the extinction probability was high and no viable C clusters could form. **b** The number of viable C edge clusters $N_{C,Edge}$ increased with increasing initial C cell number $N_{C,0}$ for intermediate inducer concentrations (data averaged for 0.005 and 0.01 μg/ml MitC). Furthermore, it was proportional to the survival probability $1 - E^{N_{C,0}}$ (blue line).

[8] Here, the Heaviside function θ was used that returns 1 if $t_{\text{Switch}} < 12h$ and zero otherwise.

[9] Previously, the toxin producer fraction, at intermediate induction was identified with an theoretical switching rate value $s_C = 0.015$ (see footnote 4). By using $r_C = 0.0729$ and the experimentally determined switching rate, one would obtain $E_{\text{prediction}} = \frac{0.015}{0.0729} = 20.6\%$. This difference might support the underestimation of initial C numbers discussed at the beginning of this section.

Conclusion

Taken together, a combination of spatial positioning and stochasticity in toxin production at low cell numbers determined the number of viable C edge clusters $N_{C,Edge}$. A broad dispersal and higher distance of individual cells from the colony center promoted $N_{C,Edge}$. Furthermore, the relationship between the number of initial C cells $N_{C,0}$ and $N_{C,Edge}$ was proportional to the survival probability as determined in chapter 4.

6.4.2. $N_{C,Edge}$ and deterministic competition parameters drive the population dynamics

Expressing the competition outcome in terms of final C strain fraction F_C, the nonlinear relation between MitC and competition outcome was confirmed (see Fig. 6.17 a). In section 6.3, it was discussed in detail, how the deterministic competition parameters (growth rate, toxin producer fraction, and sensitivity) influence this average outcome. Now, having analyzed the number of viable C edge clusters after 12 hours $N_{C,Edge}$, this experimental observable could be used as a proxy for the stochastic effects in positioning and toxin dynamics of competition phase 1.
In order to understand how the state of the community after the initial competition phase, represented by $N_{C,Edge}$, influenced the outcome of competition, the final C strain fraction F_C was plotted against $N_{C,Edge}$ for each inducer concentration separately (see Fig. 6.17 b). The data clearly showed that $N_{C,Edge}$ in combination with the inducer concentration MitC was sufficient to explain the observed competition outcomes. Depending on the dynamics in phase 1, various numbers of viable C edge clusters could form. Then, depending on the deterministic competition regime (inducer concentration), $N_{C,Edge}$ determined the competition outcome.
Once the competition was in a deterministically favorable regime (intermediate inducer concentrations), the presence of at least one cluster ($N_{C,Edge} > 0$) already led to C domination with 97.6% occupation on average, while without such clusters ($N_{C,Edge} = 0$) C was only able to occupy 39.9% on average. These latter cases ($N_{C,Edge} = 0$) included both competitions in which there were no C strain left at all and S dominated or cases in which C was present but had no access to the edge after 12 hours of competition. In these cases C was delayed in area growth but could occupy areas to be classified as coexistence later. Note that these cases of coexistence in the regime that deterministically favors the C strain (intermediate inducer concentrations) should be only transiently coexistent from a theoretical point of view [101]. However, over the time-course of our experiment (and after prolonged competition of 72h), the coexistence was stable. Furthermore, in very few cases, even with $N_{C,Edge} > 0$, coexistence cases were observed that might be explained by a remaining variability in the competition parameters.

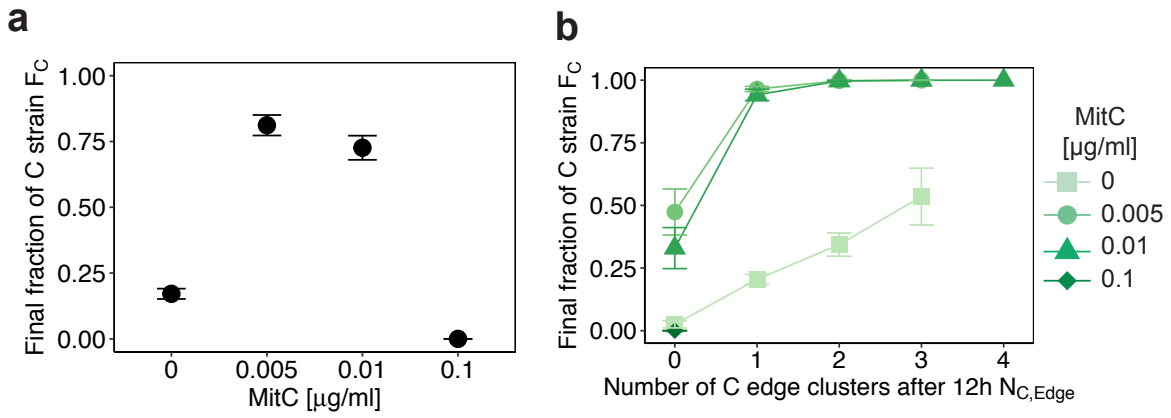

Figure 6.17.: Most important factors determining the final C fraction
a The final C strain fraction depends nonlinearly on the inducer concentration MitC. Note the nonlinear x-axis. **b** The final C strain fraction strongly depends on the number of C edge clusters $N_{C,Edge}$. Color code represents inducer concentration.

Without external inducer, the final outcome depended linearly on $N_{C,Edge}$. This indicated that a missing global toxin action reduced the toxin activity to an effective growth inhibition of S, and the interaction was mainly driven by the growth rate differences. Such interactions are known to exhibit frequency depended selection in which the initial ratio of both strains determines competition outcome [96, 97]. The linear dependence observed here might be a manifestation of that. Furthermore, this implies that even higher ratios of C:S lead to C domination without high levels of toxin production.
Finally, competition at high induction drove the small C populations extinct and no viable C edge clusters could form in the observed competition ($N_{C,Edge}$). Consequently, C could not dominate.

6.4.3. Statistical analysis of influencing factors

In order to quantify the influence of the individual contributions $MitC$, $N_{C,Edge}$, $N_{C,0}$, $D_{C,0}$, and $R_{C,0}$ on F_C and to verify the statements above, a statistical regression model was used that included interactions between the variables (see table A.4 for details). For the statistical analysis, $MitC$ was treated as a categorical variable to incorporate the qualitative differences in competition regimes. The complete model had the following form:

$$\begin{aligned} F_C = \beta_0 + MitC(\beta_1 + \beta_6 N_{C,Edge} + \beta_7 N_{C,0} + \beta_8 D_{C,0} + \beta_9 R_{C,0}) \\ + N_{C,Edge}(\beta_2 + \beta_{10} N_{C,0} + \beta_{11} D_{C,0} + \beta_{12} R_{C,0}) \\ + N_{C,0}(\beta_3 + \beta_{13} D_{C,0} + \beta_{14} R_{C,0}) + D_{C,0}(\beta_4 + \beta_{15} R_{C,0}) + \beta_5 R_{C,0} \end{aligned} \tag{6.6}$$

By analysis of variance (ANOVA), the effects of the individual independent variables on the outcome variable F_C could be estimated using the η^2 statistic [168] (see table A.5 for details). The largest contribution stemmed from the variable $MitC$ representing the deterministic competition parameters. It had a very large effect on F_C ($\eta^2 = 0.55$, $p < 2.2 \cdot 10^{-16}$). In addition, the $N_{C,Edge}$ variable that was introduced to capture the stochastic toxin dynamics had a large effect as well ($\eta^2 = 0.15$, $p < 2.2 \cdot 10^{-16}$). The other variables did not have at least medium effects on F_C in terms of the η^2 statistic. This confirmed the above results that the positioning variables only influenced the competition outcome via the formation of C edge clusters.
Finally, in order exclude the last doubts, the competition was simulated for 17 different switching rates s_C, for 16 different initial conditions IC that were each repeated 30 times. Again, the number of C edge clusters $N_{C,Edge}^{(comp)}$ was determined for these simulated competitions and a statistical model formulated (see table A.6 for details):

$$F_C^{(comp)} = \beta_0 + s_C(\beta_1 + \beta_4 N_{C,Edge}^{(comp)} + \beta_5 IC) + N_{C,Edge}^{(comp)}(\beta_2 + \beta_6 IC) + \beta_3 IC \qquad (6.7)$$

The high number of replicates enabled to test the influence of the various factors with high significance (all terms $p < 2.2 \cdot 10^{-16}$). In accordance to the experimental results very large effects stemmed from both the switching rate s_C ($\eta^2 = 0.44$) and $N_{C,Edge}^{(comp)}$ ($\eta^2 = 0.45$) while the initial conditions IC had no effect ($\eta^2 = 0.00$).
Taken together, the statistical analysis confirmed the previous results that both the deterministic parameters $MitC$ and s_C and the proxy for the stochastic initial phase $N_{C,Edge}$ determine competition outcome.

6.5. Conclusion

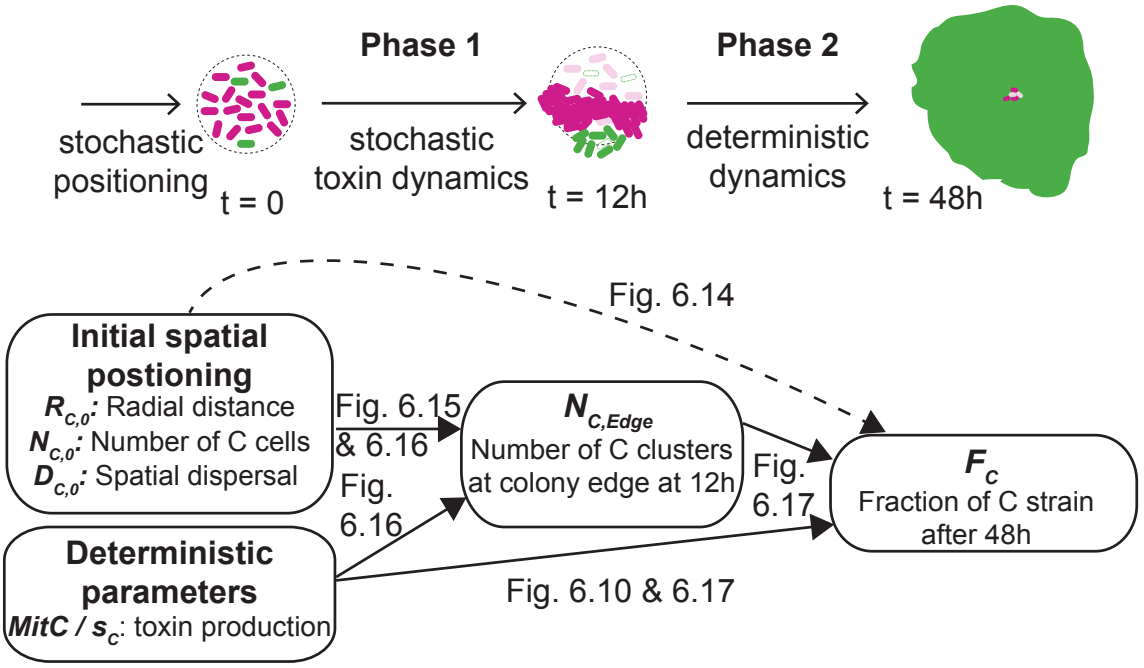

Figure 6.18.: Two phase interaction model

The experimental findings confirmed the hypothesized two-phasic interaction. First, random initial positioning and stochasticity in toxin production, shape early communities and C edge cluster formation. Second, the resulting variable $N_{C,Edge}$ together with the deterministic competition parameters (mostly the toxin producer fraction) determine the competition dynamics and consequently, the final C strain fraction F_C. References to the figures that show the indicated relations are added to the connecting arrows. Note that the arrow connecting spatial positioning and outcome is dashed because no considerable influence was observed.

This chapter showed how the interaction dynamics of a heterogeneously Colicin E2 producing strain of bacteria (C) with a sensitive strain (S) could be disentangled into two distinct interaction phases; a fluctuation dominated and a mainly deterministic phase (see Fig. 6.18).

First, stochastic processes in initial positioning and toxin dynamics shape early micro-community development which was quantified by $N_{C,Edge}$, the number of viable C clusters that formed at the colony edge after 12 hours. Taking a closer look at initial micro-colony formation, it was observed that $N_{C,Edge}$ was proportional to the survival probability of initial C cells. The survival probability $S = 1 - (s_C/r_C)^{N_{C,0}}$ (chapter 4) is determined by the random initial C cell number $N_{C,0}$ and the microscopic reaction rates of phenotype switching s_C and growth r_C.

Second, at higher cell numbers the stochastic toxin dynamics lead to an average division

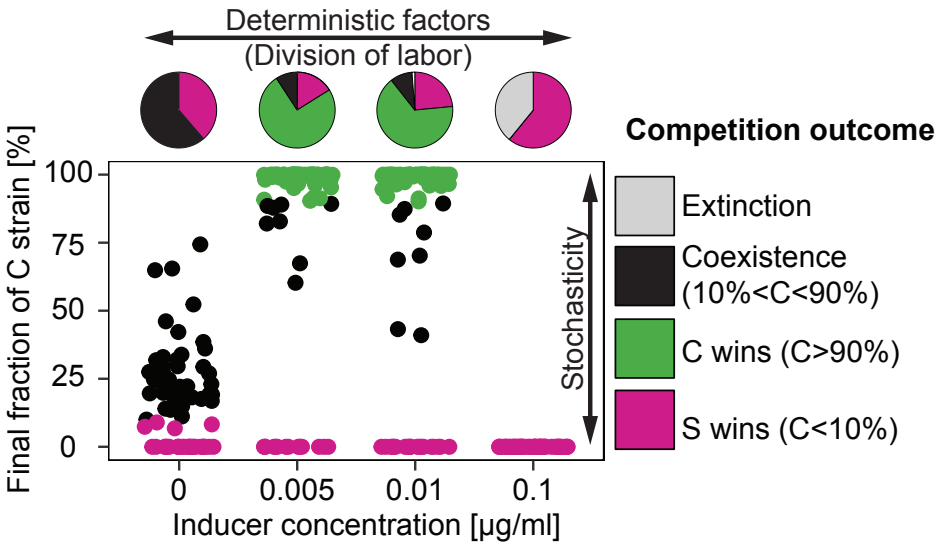

Figure 6.19.: Competition outcome explained
Condensing the insights of this chapter in one figure, one learned how deterministic and stochastic effects determined competition outcome. While the deterministic competition parameters, and in particular the degree of division of labor in toxin production, shaped the general competition outcome, stochasticity in initial conditions and early toxin production was responsible for outcome variability (multi-stability).

of labor within the heterogeneously toxin producing population with an average toxin producer fraction of $f = \frac{C_{ON}}{C_{ON}+C_{OFF}} = \frac{s_C}{r_C+d_{C_{ON}}}$ (chapter 4). Externally, the switching rate s_C and, consequently f, is varied by the addition of an antibiotic (or by parameter variation in simulations). From the experimental data one could see that varying f created qualitatively distinct competition regimes with characteristic outcomes.
However, in contrast to deterministic assumptions [97,101], the outcomes are not unique under similar conditions but feature multi-stability. The most prominent case is the simultaneous occurrence of C and S domination under weakly induced conditions that deterministically favor the C strain. It could be shown that this multi-stability arose from the stochasticity of the initial phase. C edge clusters could either establish ($N_{C,Edge} \geq 1$) or go extinct due to fluctuations ($N_{C,Edge} = 0$). In the former case, the ratio f dictates the effective interaction between C and S that governs the deterministic interaction dynamics, and in the latter case, S either survives and dominates or dies due to massive early toxin action (rare).
Taken together, the results of competitions are a combined effect of initial stochastic effects followed by deterministic dynamics set by division of labor (see Fig. 6.19). As such, the interaction system experiences a transition from a fluctuation dominated phase into a phase in which the growing number of cells results in average behavior.

By taking advantage of the experimental multi-scale method (chapter 3), the stochastic micro-dynamics as well as the deterministic competition dynamics at the macro-scale could both be investigated evenhandedly. This would not have been possible in experimental approaches focusing on one scale only. Furthermore, the obtained time-lapse trajectories were used as test data for the development of advanced statistical methods for functional response models [169][10].
The computational model used here (chapter 5) successfully complemented the experiments by exploration of experimentally inaccessible parameters such as toxin effectivity and relative competitor growth rates. Furthermore, it was able to predict competition outcome distributions in good accordance with the experimental observations and confirmed that the conclusions about stochasticity as the origin of multistability were robust with respect to a wide range of different parameters.
Just recently, instead of considering only an average toxin production cost [96], the ecological implications of the division of labor between toxin producers and surviving reproducers have been explicitly investigated [21]. In accordance to the results presented here, a strongly nonlinear inverse u-shaped producer fraction and final C strain fraction relation was found.
Previously, it was shown that initial coarsening phases are followed by later stable sector expansion for pure growth processes [115]. However, the observed variations here are even more drastic due to complete loss of one of the strains.
The independent switching of individual cells creates a survival risk for the population at low cell numbers. However, just recently, large scale *ecological suicide* was reported in soil bacteria and the authors stated potential beneficial effects for the individual bacterium [170]. While similar beneficial effects might play a role here, the colicin system can be seen as an example for what happens if population coordination fails. Mitigation strategies for the bacteria include communication by quorum sensing in order to avoid switches from the viable state to an inhibited state under conditions in which survival is unlikely [70]. In fact, colicin molecules have been shown to mildly auto-induce colicin production within the producer population, which can be interpreted as a first step towards the population level coordination of colicin production [95].
While only very few studies investigated the implications at large cell numbers explicitly in experiments, the importance of stochasticity in biological processes has been known for years. In this work, it was shown how stochastic events at the single-cell level can propagate through large-scale systems determining their long-term behavior. Therefore, the study does not only have implications for the colicin E2 interaction system, but probably for a variety of microbial systems in which stochastic phenotype switches play a role.

[10] This work is listed in the publication list as [S1].

7. Investigation of bacterial interactions: Three-strain interaction[1]

After investigating the role of stochasticity and division of labor on the two-strain interaction, the question arose, how robust these findings are in more complex interaction systems. The three-strain interactions system additionally featuring a resistant strain has long been used as a model system for transient interaction networks (Rock-Paper-Scissor) [14, 15, 98] or as a model for bacterial competition in general [25].
Only recently, the role of higher order interactions, i.e. interactions between two strains on a third one or the modulation of a pairwise interaction by a third strain [120], have been studied in detail. In particular, the role of cheating, exploitation of the toxin action by the R strain that does not bear the cost of toxin production, has been studied [100]. Furthermore, in conceptually similar Producer-Sensitive-Resistant system of mixed yeast and *E.coli* strains, the active shielding by toxin degradation was found to exhibit rich dynamic behavior [171].
However, these recent studies mainly focused on the macroscopic interaction dynamics and a microscopic investigation of such higher order interactions remains lacking. In particular, the following aspects are of interest. First, do stochastic processes play an equally important role for the competition outcome as one observed in the two-strain interaction? Second, do the competition dynamics display similar two-phasic behavior as seen for the two-strain competition? Third, toxin action is distance dependent. Does one observe shielding of the S strain by R from the toxin? Fourth, cheating as a higher order interaction is consequently also distance dependent. What consequences does this have for the population dynamics?
In order to address these questions, the extended interaction system was investigated using the multi-scale experimental setup presented earlier (chapter 3) and simulated using the computational model. In analyzing the data, a new local analysis framework was developed that connected the micro to the macro scale. Taken together, the data revealed that in addition to global effects of cheating there was a significant local variation in competition outcome due to stochastic effects in early community patterning. The parameters describing the early community formation predicted the competitions outcomes reasonably well, which resembled the two-phasic dynamics of the CS competition. However, the second phase showed prolonged neighbor-feedback due to cheating

[1]This chapter is largely based on publication [B3]

and was therefore still influenced by the random initial positioning. Furthermore, the data did not support the hypothesized shielding mechanism.
In conclusion, the work presented in this chapter underlines the importance of local and stochastic effects for deciding community fate in spatially extended competition.

7.1. Interaction scenario

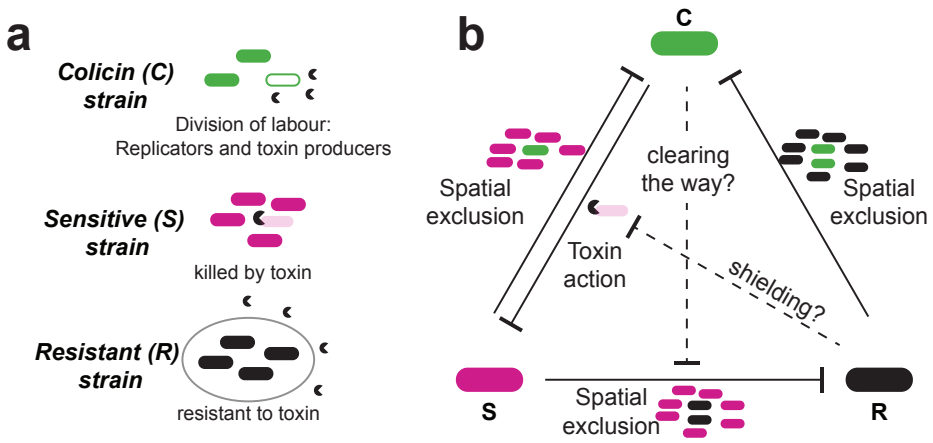

Figure 7.1.: Interactions in three strain competition
a In addition to the heterogeneously toxin producing colicin (C) strain and the sensitive (S) strain already presented in chapter 6, a resistant (R) strain was added to the competition. **b** The main interaction mechanisms were toxin action and spatial exclusion facilitated by higher initial abundance and growth rate differences. Potential higher order interactions in this system included shielding and toxin exploitation of the R strain.

In this chapter, the interaction system comprised three different bacterial strains, S_{RFP}, C_{pMO3}, and R_{NFP} (see Fig. 7.1 a). In contrast to the interactions investigated in the previous chapter, here, all three strains competed at the same time. Formerly, in the CS interaction, the main competitive interactions were the toxin action of C on S and the spatial exclusion of the C strain by S. By extending the competition system with the third toxin resistant (R) strain the number of possible interactions increased to 6 direct interactions and 3 higher order interactions that arose through the combined action of two strains on a third strain.
However, of these 9 possible interactions only the six most promising candidates are depicted in Fig. 7.1 b. First, the direct pairwise interactions, toxin action of C on S and various spatial exclusion interactions that arise through initial ratio imbalance and growth rate differences, are believed to be similar to what was observed in the two strain interaction. Second, higher order interactions such as cheating or shielding are

hypothesized to play an important role in the competition. In particular, cheating, i.e. exploitation of C's toxin action by the R strain, is expected to reduce S's adverse effects on R, and shielding of S from C's toxin by R might also be important.
This chapter now aims to unravel the individual interactions mechanisms and, in particular, to assess the importance of locality. To this end, competition experiments were performed similar to the two strain interaction. First, the final competition outcomes were analyzed with respect to the deterministic parameter toxin producer fraction aided by computational simulations. Then, motivated by earlier findings (chapter 6), the early phase of competition was analyzed in more detail and revealed the influence of stochastic effects on early community patterning which predicted the final outcome reasonably well. Third, to explain remaining variability in competition outcome, a comprehensive local analysis was performed that reveals the importance of local variation arising through stochastic positioning. Finally, the data obtained from the local analysis underlined the importance of distance dependent interactions of neighboring clusters for competition outcome.

7.2. Competition experiments

The experiments presented in this chapter were performed using the multi-scale fluorescence setup (presented in chapter 3). Again, initial communities were prepared on solid M63 agar plates supplemented with arabinose (0.2%), ampicillin (100 μg/ml), and different inducer concentrations. Then, the plates were kept at 37°C and observed for 48 hours. Due to the observed similarity in competition outcome for both intermediate inducer concentrations (see chapter 6), the experiments were performed for only three concentrations (0.0, 0.01, 0.1 μg/ml MitC).
However, compared to the interaction of the toxin producers and the sensitive strain, the experiments were changed in some regards. Most importantly, the R strain was added to initial cultures. In order to reduce the C extinction probability and increase the likelihood to find initial C and R cells in proximity, the C ratio was increased such that the initial culture had a ratio of 2:10:10 (C:R:S). Furthermore, to increase the number of observable higher order interaction sites, the spotting volume for sample preparation was increased to 15nl (formerly 2.5nl). Consequently, experimental settings were changed to accommodate larger initial communities (see table B.1).

7.2.1. Global competition outcome

When investigating the interaction network between the three strains, the prominent role of toxin action was evident. It mediates the interaction between C and S strain

directly and was consequently also involved in the potential higher order interactions cheating and shielding. Therefore, in a first step, the experiments were performed for three different inducer concentrations and the outcome was determined in terms of the relative strain abundances after 48 hours (see section 3.3.1 for details). For convenience the relative abundances $X \in \{C, R, S\}$ are denoted with their symbol $X = \frac{A_X}{\sum_{i\in\{S,R,C\}} A_i}$, A_i being the occupied area of a strain i.

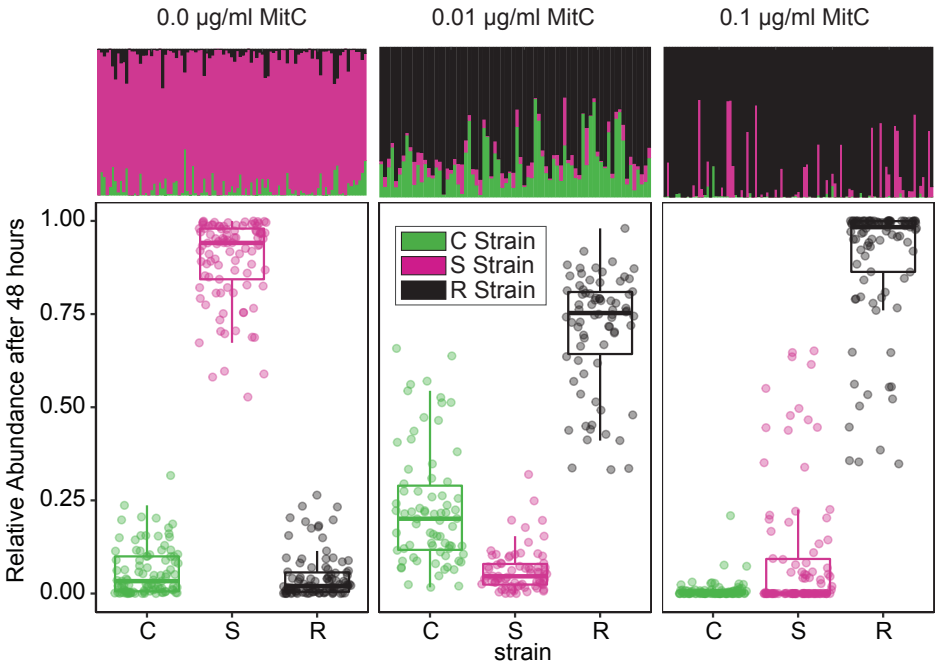

Figure 7.2.: Global competition outcome

The outcome after 48 hours of competition was determined in terms of the relative strain abundances and is depicted as dots for every replicate. Boxplots summarize the distributions of competition outcomes for the three different indcuer concentrations and display the median as inner line and the 25% (75%) percentiles as lower (upper) box edges. Color code is indicated in inset. The top row bar plots depict relative final abundances for individual competitions. Number of replicates for each inducer concentrations : $N_{0.0} = 97$, $N_{0.01} = 74$, $N_{0.1} = 95$.

Varying the toxin producer fraction by using different inducer concentrations revealed a strong dependence of competition outcome on toxin producer fraction (see Fig. 7.2). In the absence of external inducer, the S strain is most prominent (average ± standard deviation: $S = 89.5 \pm 11.1\%$) and its spatial exclusion strategy did not allow C and R to occupy large areas ($C = 5.8 \pm 6.6\%$ and $R = 4.6 \pm 6.2\%$). At intermediate toxin producer levels (0.01 μg/ml MitC), S's dominance was clearly broken and one observed a strong and significant[2] decrease in relative abundance ($S = 6.2 \pm 5.8\%$, $W = 7178$,

[2] Significance tests were performed using the Mann-Whitney-Wilcoxon test due to non-normality of

$p < 0.001$). In part, this shift in outcome stemmed from a significant increase in C strain occupation ($C = 23.0 \pm 15.8\%$, $W = 6321$, $p < 0.001$). However, the R strain profited from the increased toxin the most and is subject to a highly significant 15-fold increase in average occupation ($R = 70.9 \pm 15.5\%$, $W = 7178$, $p < 0.001$). Increasing the toxin producer fraction even further (0.1 μg/ml MitC) led to a large and significant decrease in final C strain fraction ($C = 0.8 \pm 2.4\%$, $W = 77$, $p < 0.001$). This relative area liberation due to C suicide led to a significant increase for the R strain ($R = 89.3 \pm 17.6\%$, $W = 5931$, $p < 0.001$) while the S strain was not able to occupy significantly larger areas compared to the intermediate toxin producer fractions.
In the highly induced case (0.1 μg/ml MitC), one could observe a bimodality in the outcome distributions of R and S strain. This bimodality between high and low S abundance values is believed to be similar to the multistability of extinction and S survival in the CS-competition for high induction (chapter 6).

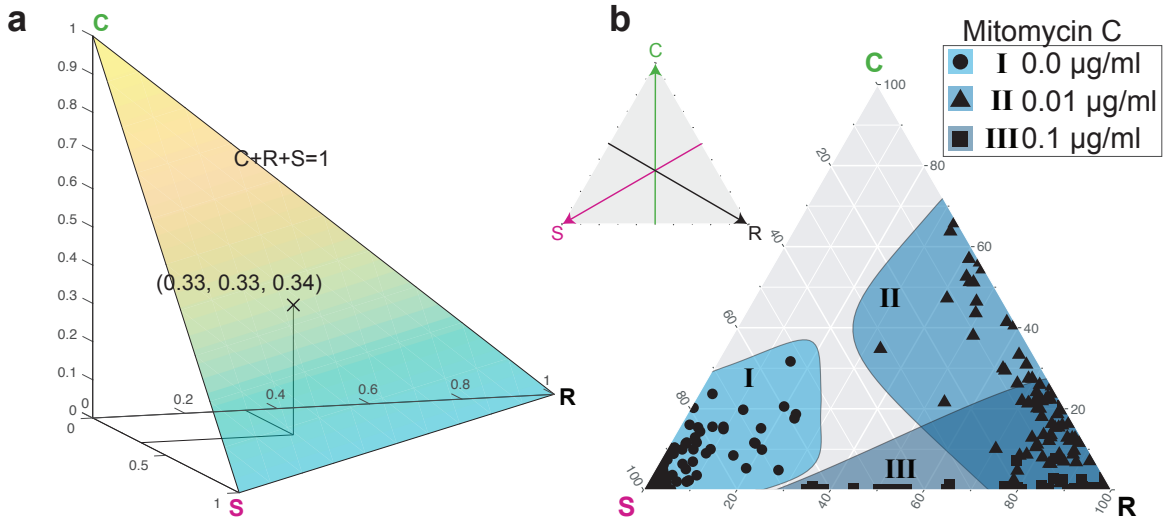

Figure 7.3.: Competition outcome in three-species simplex illustration
a The simplex hyperplane is defined by the relation $S + C + R = 1$, in which the variables $S, R, C \in [0, 1]$ denote the relative strain abundances. This illustration allows the convenient 2D illustration of the three dimensional composition vector because any possible combination is a point on this surface. **b** Illustrating the competition outcomes in such a three-species simplex plot, one sees differently occupied regions with varying inducer concentration (see shaded regions marked with I, II, and III and legend insert). The small insert simplex illustrates how to read the plots. For example, the lower left corner correspond to pure S communities.

These observations were consistent with the interaction model presented above (Fig. 7.1 b). Plotting the outcome data on a three-species simplex, the 2-dimensional projec-

the data. Consequently, the W-statistic is reported.

tion of the relative abundance hyperplane ($C + R + S = 1$) further illustrated the shift in competition outcome and the distinction between the competition regimes (see Fig. 7.3). Without external inducer, the fraction of toxin producers within the C population was low and toxin action did no play a large role. Consequently, the interactions mainly relied on spatial exclusion in which the S strain having a larger initial ratio was most successful and excluded R and C from space and resources (Fig. 7.3 b, area I). Increasing the toxin producer fraction to intermediate levels maximized the toxin action to the disadvantage of the S strain. While C itself profited from this, the true beneficiary of the increased toxin production was the R strain. Without the cost of producing the toxin and, still being freed of the suppressive S strain, R was able to thrive and occupy large area fractions. This exploitation of toxin action by the resistant strain is referred to as cheating. Consequently, the final competition outcome settled on the R-C coexistence line (Fig. 7.3 b, area II). Finally, increasing the toxin producer fraction further was to the disadvantage of the C strain. C itself was largely unable to further compete with R (and S) and its relative abundance dropped drastically. Consequently, the final outcomes settled near the R-S coexistence axis (Fig. 7.3 b, area III). In some cases, S was able to occupy relatively large area fractions, probably due to stochastic effects in initial positioning preventing it from completely succumbing to C's toxin action. Interestingly, compared to the two-strain interaction, in which high toxin producer levels led to either extinction of colonies or the recovery and later domination of S, S could not fully recover from the early toxin damage and R was able to dominate. This indicated an especially important effect of toxin action timing and resembled the two-phasic interaction observed earlier. This idea will be discussed in detail in section 7.3.
Taken together, the results suggested that both, the phenotypic balance of toxin production and the cheating action of the R strain globally influenced the outcome of competition.

7.2.2. Computational outcome

In order to generalize the experimental findings, the stochastic lattice-based computational model was extended to incorporate the resistant strain (see section 5.2.2). The growth rates were newly determined from control data with 15nl initial volume and were in accordance to data obtained in two-strain experiments (deviation $\approx \pm 10\%$) for S and C. R, however, grew considerably slower. Therefore, the newly obtained rate was used (see **??** for experimental and model growth rates).
Again varying the toxin production rate s_C enabled the comparison of experimental and computational results and revealed that the qualitative shift in competition outcome was reproducible by just varying the single s_C parameter (see Fig. 7.4). The simulated trajectories led to final states that accumulate near the experimental ones.

Hence, the dynamics were attracted to final states that are determined by the toxin producer fraction.

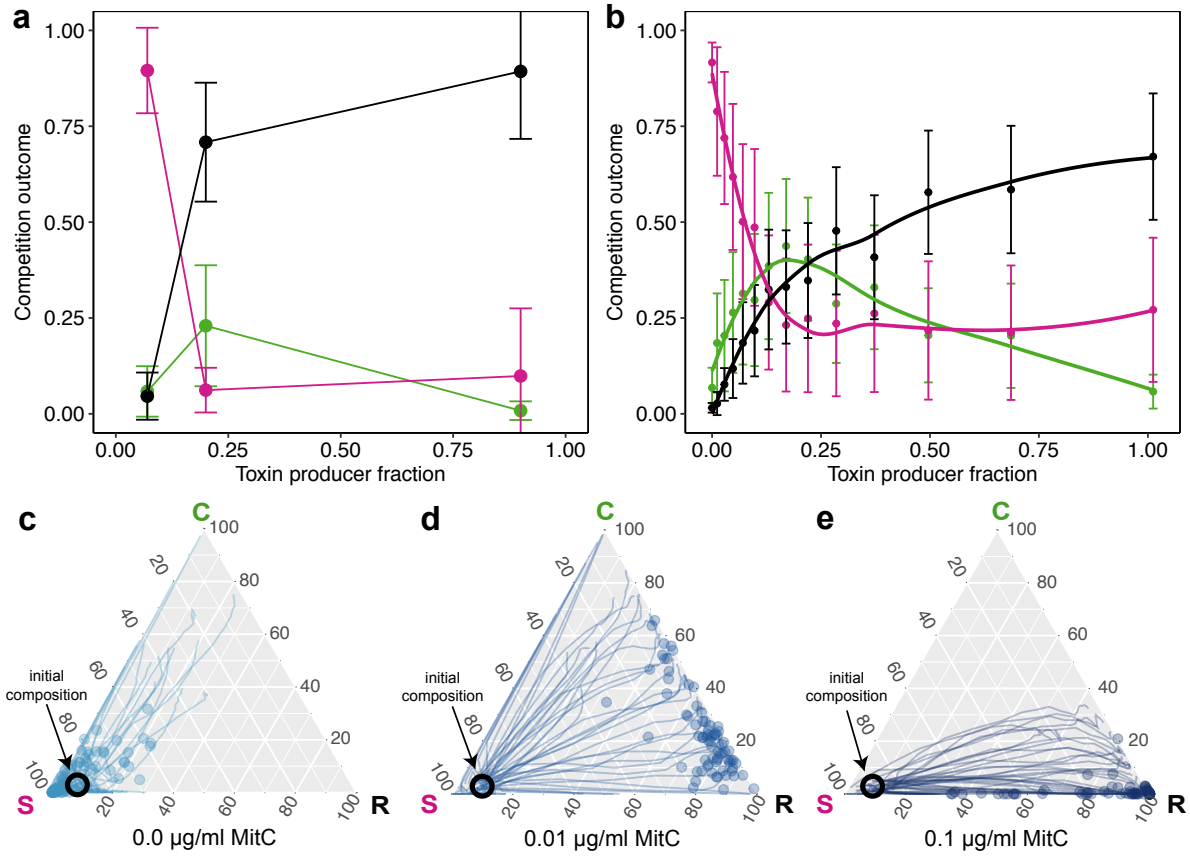

Figure 7.4.: Competition outcome in experiment and simulation

Average experimental (**a**) and simulated (**b**) competition outcomes depended on toxin producer fraction. While R (black) and S (magenta) showed increasing/decreasing behavior, C (green) showed peaking.

The experimental final competition outcomes (points) and simulated competitions (curves) were in agreement for the three interaction regimes: low producer fraction ($s_C = 0.0026$, $[MitC] = 0.0\mu$g/ml, **c**), intermediate producer fraction ($s_C = 0.02$, $[MitC] = 0.01\mu$g/ml, **d**), and high producer fraction ($s_C = 0.0920$, $[MitC] = 0.1\mu$g/ml, **e**). The initial conditions (C-R-S ratio 2:10:100) are highlighted.

7.2.3. Alternative competition scenarios

In order to verify that indeed the toxin action was the driver behind the observed competition outcome, pure R-S competitions were simulated. Starting from the same initial ratio (10:100), the simulation showed clear dominance of the S strain ($S = 98.2 \pm$

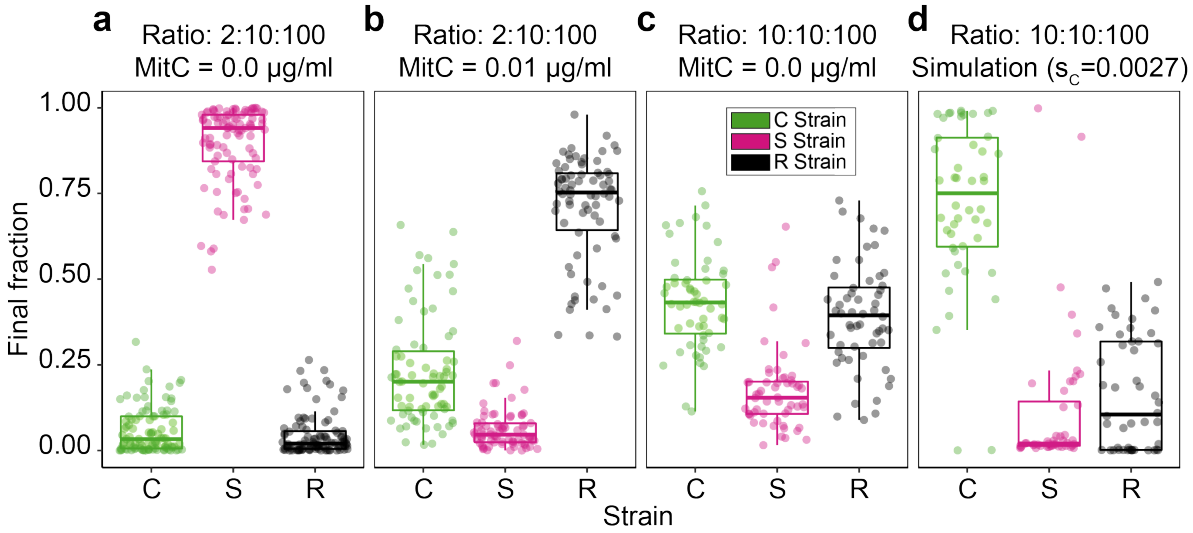

Figure 7.5.: Variation in initial condition shifts outcome distributions
a,b Experiments with initial 2:10:100 ratio (the original experiments, see Fig. 7.2) with no and low induction. **c** Experiment with higher initial C ratio without induction (10:10:100) shows clearly increased final C fraction but lower R and less suppressed S compared to (**a**). **d** Simulations of 10:10:100 initial ratios deliver qualitatively similar results as experiments.

3.1%) which was similar to the outcome of competition experiments without external inducer. To verify this prediction, experiments without the C strain were performed and yielded remarkably similar results compared to the simulation with an even higher average final S abundance of $S = 99.8 \pm 0.8\%$.
Hence, it was concluded that without the toxin action of C, the R strain is unlikely to successfully compete with S and the global success of R must therefore be attributed to C's toxin action and R's cheating.
Furthermore, a variation of strain ratios was investigated (Fig. 7.5). Experiments were performed at initial C:R:S ratio of 10:10:100 in the absence of external inducer (Fig. 7.5 c). Interestingly, the increase from no to low induction corresponds to an approximately 5-fold increase toxin producer fraction. Therefore, the new experiments can be discussed in comparison to the original (2:10:100), uninduced and lowly induced cases (Fig. 7.5 a and b). The increase in ratio (Fig. 7.5 c) boosted the C strain such that it occupied ratios higher than with low ratio and low induction (Fig. 7.5 b) but led to R fractions lower than in the induced case (Fig. 7.5 a) and less suppressed S as well.
This indicated that the change in competition dynamics due to the increase in ratio is qualitatively different than changing the toxin producer fraction. More C cells lead to more offspring sites from which C can replicate but at the same time less toxin is produced, S is less suppressed and R is consequently weaker.
Simulating the changed initial ratio delivered qualitatively similar results (Fig. 7.5 d) in comparison to the original ratios (Fig. 7.5 a,b).

7.3. Early phase of interaction

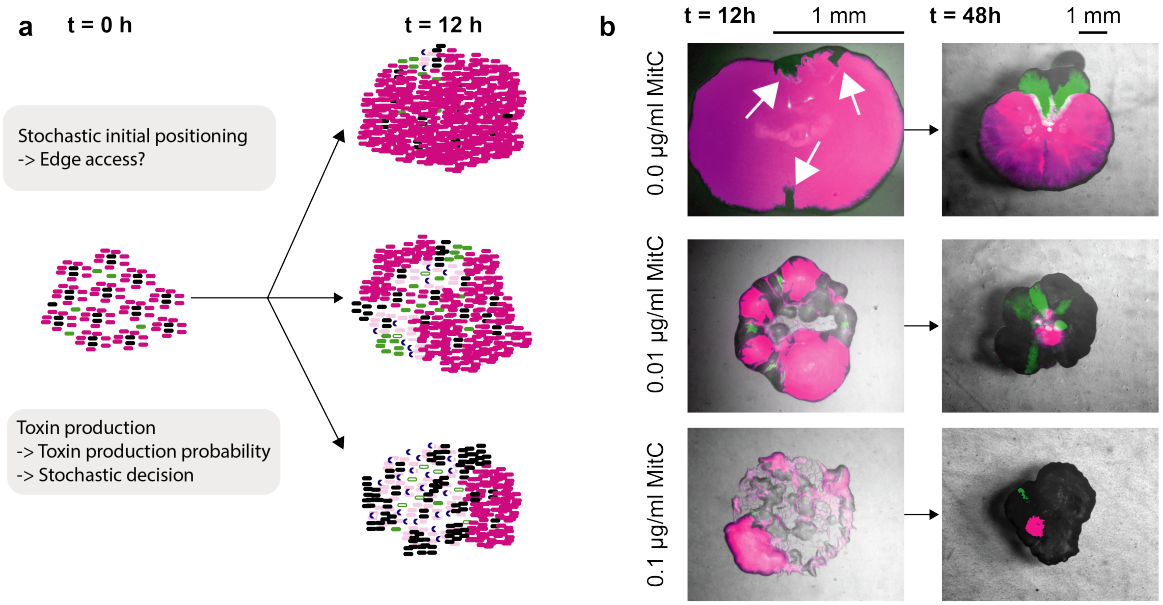

Figure 7.6.: Early toxin action determines the ensuing dynamics

a Early community development is determined by (1) the probability of toxin production, (2) the stochastic positioning of cells, and (3) the stochastic toxin production dynamics. **b** For the different inducer concentration, typical community appearance after 12 hours was already different (left). In hindsight, the final colony composition and structure (right) could be extrapolated from the 12-hour snapshot (left). Scale bar for 1 mm changes due to different zoom for 12h and 48h. White arrows in top row indicate non-S clusters.

Although the variation in competition outcome was not as pronounced as in CS interaction, the competition outcome was not unambiguous. From the two-strain interactions one knew that the competition had a stochastic early phase and a later deterministic phase. This motivated the detailed analysis of the early competition phase ($t < 12h$) in order to identify random effects in this initial phase that influence the final competition outcome.

Screening the competition experiments led to the hypothesis that originating from an initial colony of relatively uniformly distributed single cells, toxin action locally clears the space from S cells giving way to growth of C and R cells. Without toxin action, C and R cells are unlikely to have gained or gain access to the external space and thrive. So, depending on (1) the probability of toxin production, i.e. inducer concentration in experiments or s_C in simulations, (2) the stochastic positioning of cells, and (3) the stochastic toxin production dynamics, early communities form (see Fig. 7.6 a). In addition to this positioning and toxin related randomness, random growth processes - or

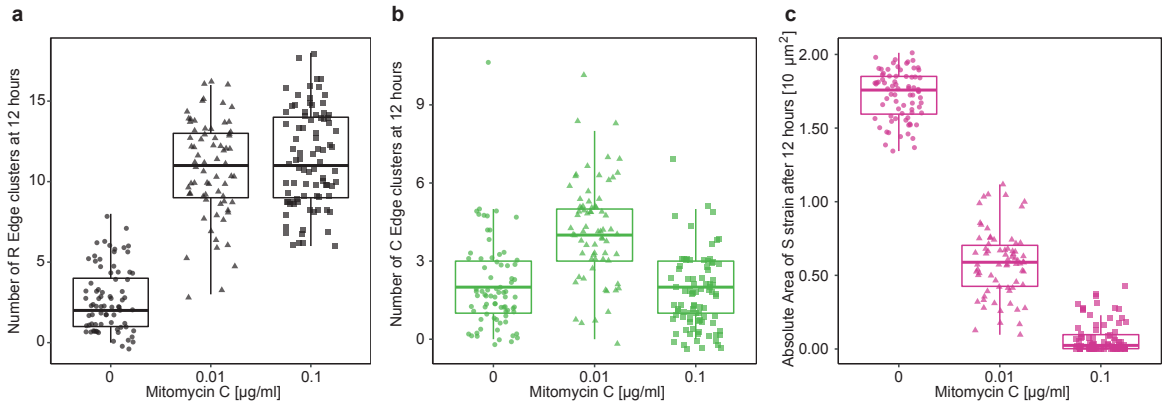

Figure 7.7.: Early community patterning is characterized by early phase variables numbers of R & C edge clusters and S area at 12 hours
Early community patterning is characterized by the number of R and C clusters at the colony edge and the S area after 12 hours of competition and shows characteristic variation with changing inducer concentration. **a** With increasing inducer concentration, the number of R edge cluster $N_{R,Edge}$ increases. **b** C edge clusters $N_{C,Edge}$ increase for intermediate inducer concentration but decline at high induction due to high lysis. **c** The area of the S strain decreased significantly with increasing inducer concentration.

genetic drift - are known to lead to an initial stochastic coarsening dynamics before stable sectors form [115]. Then, depending on who survived this initial scramble, the deterministic interactions in the second phase then mainly determine the competition outcome. For example, the colony appearance after 48 hours could already be guessed from the appearance after 12 hours (see Fig. 7.6 b).
In order to verify these suggested relations, the early community patterning was quantified by three variables characterizing the colony at 12 hours. These early variables included the number of C and R clusters with access to the colony edge $N_{C,Edge}$ and $N_{R,Edge}$ and the area of the S strain after 12 hours A_S^{12h}. As a first results, one observed that the early variables significantly varied with increasing inducer concentration (0.01 or 0.1 μg/ml MitC) compared to the uninduced case, probably due to increased toxin action (Fig. 7.7). In particular, $N_{R,Edge}$ increased significantly under induced conditions (Fig. 7.7 a). $N_{C,Edge}$ was subject to an increase as well, although it declined again under highly induced conditions due to cell lysis (Fig. 7.7 b). Finally, A_S^{12h} showed an ongoing decrease with increased toxin inducer concentration (Fig. 7.7 c), again showing how early toxin action affects the S strain's presence and early colony formation.

Characterizing the community at the 12 hours time-point enabled to correlate the early variables to the final competition outcome (Fig. 7.8 and table B.3). Interestingly, $N_{R,Edge}$ and the final R abundance only correlated weakly ($r = 0.37$, $p < 0.01$) for the intermediate inducer concentration (Fig. 7.8 a), while for the other two concentrations no significant correlation was found. Similarly, $N_{C,Edge}$ correlated with the final C abun-

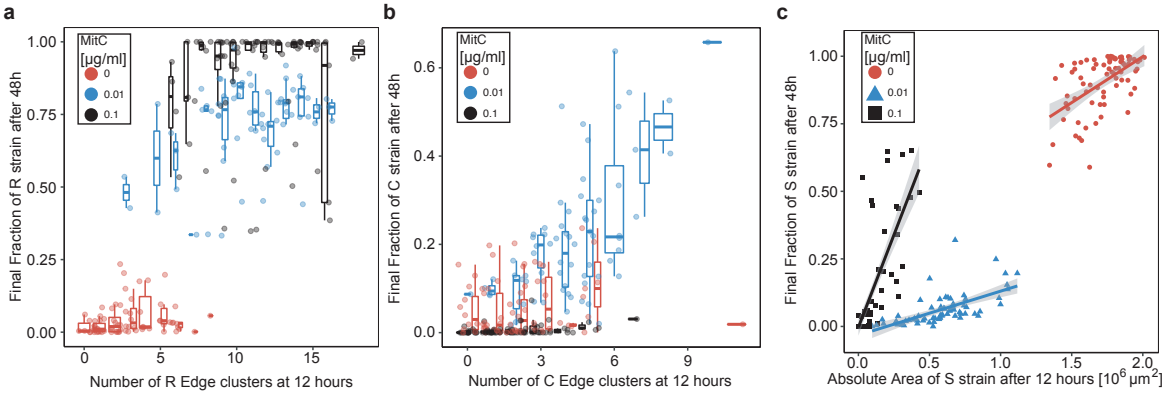

Figure 7.8.: Relation of early phase variables and competition outcome
a,b Relation between R (C) outcome (48 hours) and R (C) clusters at 12 hours. **c** Relation between S outcome (48 hours) and S area at 12 hours. Shaded regions around regression lines represent 95% confidence intervals.

dance strongest for intermediate induction ($r = 0.64$, $p < 0.001$) while the other two concentrations showed no large variation (Fig. 7.8 b). The fact that the correlations were largest at intermediate induction for the two strains underlines the R-C abundance driven competition in this regime.
Finally, for the final S abundance one could indeed find highly significant positive correlations with A_S^{12h} and the final S strain fraction (Fig. 7.8 c and table B.3). The strength of correlation in terms of the correlation coefficient r varied from medium to large effect sizes [168] and increased with inducer concentration. This dependence on inducer concentration suggested that with increasing toxin producer fraction, the competition dynamics got more predictable and deterministic for the S strain. In turn this indicated that without external inducer at low toxin producer fractions, effects not related to toxin action were more important and created large variability.

In order to condense the knowledge on the three early variables, the competition outcome was modeled using the following model for the final fraction F_i of strain $i \in C, R, S$:

$$F_i = \beta_1[MitC] + \beta_2 N_{R,Edge} + \beta_3 N_{C,Edge} + \beta_4 A_S^{12h} \tag{7.1}$$

In case of R and S strains, early community pattern variables $N_{R,Edge}$, $N_{C,Edge}$, and A_S^{12h} together with the inducer concentrations, predicted the final abundance very well ($R^2 = 0.89$, table B.5, and $R^2 = 0.92$, table B.4, $p < 0.001$ in both cases). However, in case of the C strain, the final fraction was not as predictable ($R^2 = 0.59$, table B.6, $p < 0.001$). This might be due to the stochastic toxin production that makes C less predictable and risks its survival.
Taken together, the results verify the hypothesized two-phasic interaction: After random initial patterning, largely deterministic competition dynamics follow. In the initial

stochastic phase, the community can be characterized by three variables which, in case of S and R, predict the final outcome very well.
However, the second competition phase is still subject to random processes. This is especially evident, when considering figure 7.6 b top row. There one sees how the lower one of initially three non-S clusters vanishes during competition and is overrun by S while the upper two ones build a large combined cluster. This is a manifestation of randomness in growth processes that can either stem from genetic drift [115] or might be due to local interactions with neighboring clusters. In the following these local interactions are discussed.

7.4. The importance of position

After analyzing the early competition phase and its influence on competition dynamics, it became clear, that there was still a large variability involved in the competition outcome. Two sources of stochasticity were known in this system in addition to random growth: the noisy toxin dynamics and stochastic initial positioning. The extinction probability was found to decay exponentially with initial C cell number (see equation 6.4). Therefore, the 6-fold increase in initial volume reduced the effect of toxin production stochasticity compared to the CS-competition (chapter 6).
Nonetheless, the positioning variability remained high and together an upper limit for the toxin range, locality was assumed to play a larger role compared to the two-strain competition. In order to assess this important factor, the colony images were analyzed in detail using a local analysis method that focused on regions of interest that originated from R and C clusters determined at 12 hours. Furthermore, the interactions between such clusters were assessed as a proxy for higher order neighbor interactions.

7.4.1. Local analysis methods

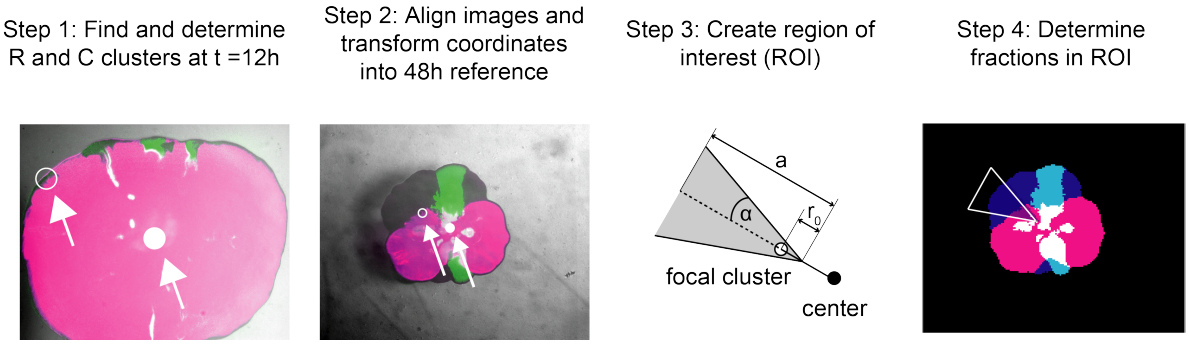

Figure 7.9.: Local analysis method
Step 1: Center positions (full white circle) and cluster position of a non-S cluster of interest (here example highlighted with hollow white circle) were detected after 12 hours of competition. Step 2: Coordinates of 12 hour positions were transformed into coordinates in the 48 hour image reference to account for zooming. Image shows overlay of final colony and initially determined positions. Step 3: For a given focal cluster, a region of interest (ROI) was constructed as a triangle (see main text for details). Step 4: This ROI was used to locally analyze the competition outcome.

The local analysis methods involved multiple steps (see Fig. 7.9). First (Step 1), positions of C and R clusters at 12 hours and the center position of the community were determined semi-automatically by screening the competition time-lapse data and

taking into account the fluorescence signals.
Then (Step 2), by using the magnification differences between the zoom levels, the 12 hours coordinates $\mathbf{x_{12}}$ were converted into the 48 hour coordinates $\mathbf{x_{48}}$ of the registered clusters. To this end, the coordinate $\mathbf{x_{48}}$ was determined by adding the connection vector from the image center $\mathbf{z} = (513, 641)$ to the 12 hours coordinate rescaled by a magnification factor $f = F_{12h}/F_{48h} = 2.2/10$:

$$\mathbf{x_{48}} = \mathbf{z} + f \cdot (\mathbf{x_{48}} - \mathbf{z}) \tag{7.2}$$

Similarly, the colony center coordinate $\mathbf{c_{48}}$ was transformed:

$$\mathbf{c_{48}} = \mathbf{z} + f \cdot (\mathbf{c_{48}} - \mathbf{z}) \tag{7.3}$$

The third step was to determine the regions of interest belonging to a certain focal cluster. By assuming radial growth, the connection vector r between colony center and cluster coordinate reads:

$$\mathbf{r} = \mathbf{x_{48}} - \mathbf{c_{48}} = |r_{48}| \begin{pmatrix} \cos(\beta) \\ \sin(\beta) \end{pmatrix} \tag{7.4}$$

The region of interest was defined as a triangle originating from a point $\mathbf{a_0}$ slightly shifted by a distance $|r_0|$ from the cluster coordinate in the direction of the colony center:

$$\mathbf{a_0} = \mathbf{x_{48}} - |r_0|/|r_{48}| \cdot \mathbf{r_{48}} \tag{7.5}$$

Then, the two equal length vectors of the isosceles triangle were defined by

$$\mathbf{a_{1,2}} = \mathbf{a_0} + |a| \cdot \begin{pmatrix} \cos(\beta \pm \alpha) \\ \sin(\beta \pm \alpha) \end{pmatrix} \tag{7.6}$$

in which α was half of the opening angle and $|a|$ the height of the triangle (see Fig. 7.9 Step 3 for details). Here, $|r_0| = 50$ pixel, $\alpha = 20°$, and $|a| = 400$ pixel was used.
Finally (Step 4), using the geometric construction outlined above the region of interest (ROI) was used to locally analyze the competition outcome for each registered focal C and R cluster.

7.4.2. Local competition outcome

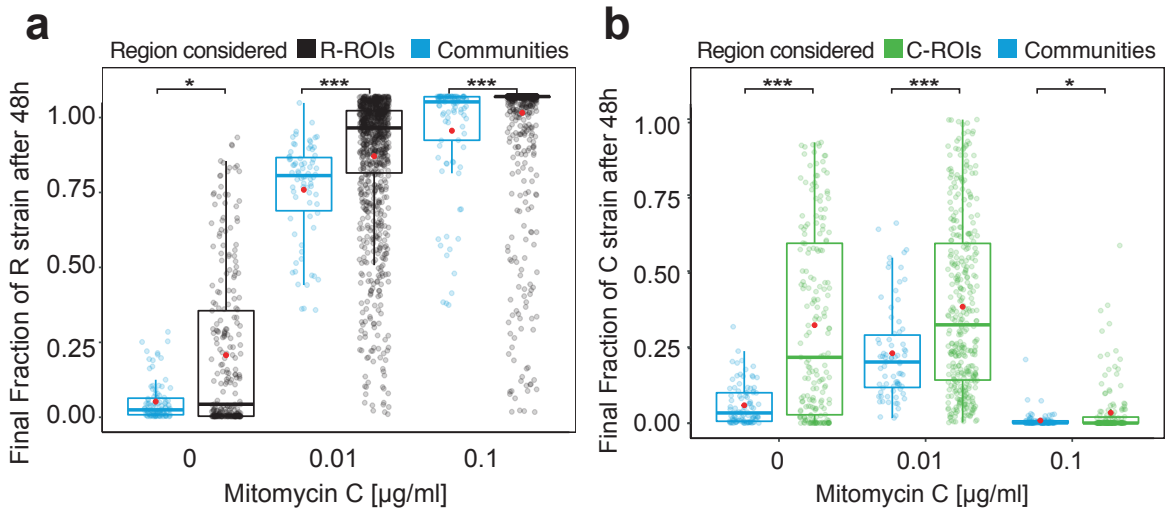

Figure 7.10.: Local competition outcome

a Final R strain fraction in ROIs originating from R edge clusters (black) show significantly higher average abundance values (red dots) and larger outcome variability except for the highly induced case compared to the complete communities (blue). **b** The same observations were made for the C strain (green). However, at high induction, both categories showed no sufficient abundances due to increased lysis. Significance is indicated with asterisks (*: $p < 0.05$, ***: $p < 0.001$).

In order to assess the effect of local variability on the competition outcome, the method outlined above was applied to the three-strain competition experiments. Comparing the relative strain abundances within the locally analyzed edge clusters to the global competition outcomes under the same conditions, one observed significant differences between local and global competition (see Fig. 7.10). For both, R and C strain, the average final abundance of the respective strains and the outcome variability in these ROIs were greatly enriched compared to the global competition outcome. Despite the significance, the size of the average differences decreased with increasing inducer concentrations for both strains and the effects were largest without external inducer.
How much variability really arose locally became evident, when the competition outcome was plotted in the three-species simplex diagram (see Fig. 7.11). Here, one clearly saw a much higher variability in competition outcome. In the uninduced case, the local outcome space was nearly evenly populated which was in stark contrast to the global competition outcome. For higher induction, the variability decreased analogously to the average difference between global and local outcome, but still, locally outcomes were realized that did not happen globally.
Taken together, the analysis showed that local and global competition outcomes could

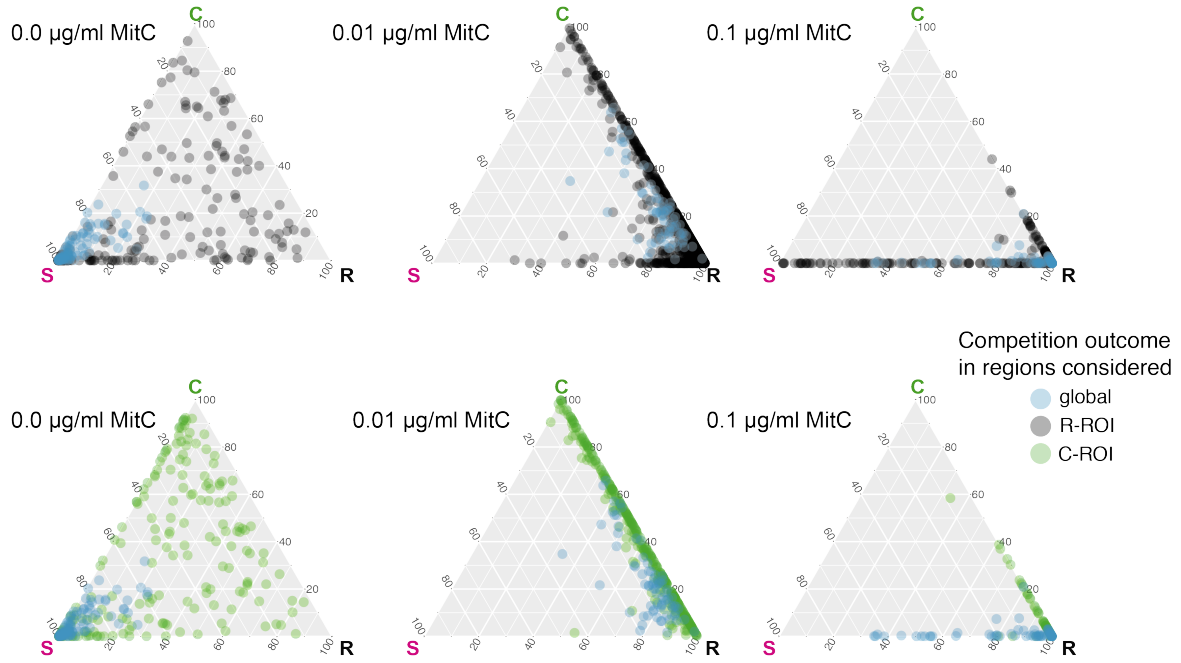

Figure 7.11.: Local competition outcome as three-species-simplex
Global (blue) and local competition outcome are plotted for the R-ROIs (**a-c**, black) and C-ROIs (**d-f**, green) for the three different inducer concentrations (**a,d**, 0.0; **b,e**, 0.01; **c,f**, 0.1 μg/ml MitC).

differ as a result of locally changed interaction dynamics. Furthermore, the observed high outcome variability underlines the importance of stochasticity on the microscopic scale. Even after the initial phase's random early colony patterning, there are still effects that lead to a high variability in the second phase which is assumed to originate from two sources. First, random genetic drift creates random growth paths [115, 172, 173] and, second, the random initial distribution of neighboring clusters continuously feeds back to the following growth due to mutual influence of these clusters. In the next section, these neighbor interactions will be investigated in more detail.

7.4.3. Higher order interactions

The dependence of R success on C presence has been shown above. Furthermore, it was hypothesized that in the later largely deterministic phase, the competition dynamics are influenced by the relative positioning of neighboring clusters. These *higher order* interactions of neighboring clusters will be investigated in this section. The term higher order interaction stems from the fact that the local R-S competition can be indirectly influenced by neighboring C clusters via toxin action.
In order to get an estimate of the relevant scales in the C-R interaction, the C fraction within R-ROIs was plotted against the distance to the nearest C cluster for weakly induced case in which toxin action and growth competition play a role (see Fig. 7.12). One observes a clear accumulation of high-valued C-fractions at distances under 250 μm. In order to get a better estimate of this cut-off distance, the data was fitted with a sigmoidal function as a smooth version of a step function:

$$f(x) = a\left(1 - \frac{1}{1 + \exp(-b(x-c))}\right) \tag{7.7}$$

in which a, b, and c were fitting parameters and x the distance. The values obtained by non-linear least square regression are given in figure 7.12 and most importantly, the distance at which the sigmoidal plot decayed to half it original value was in accordance to the assessment by eye ($b = 252.6\mu$m).

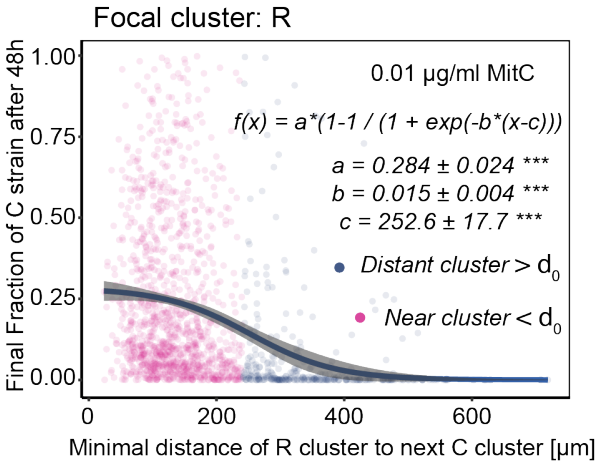

Figure 7.12.: Distance dependent interaction

C strain abundance within R-ROIs is plotted against distance to the nearest C cluster and fitted with sigmoidal function. Functional form and parameter estimates are given as insert. Data is taken from weakly induced case (0.01 μg/ml MitC). Color coding of dots according to classification of k-means clustering that separates data into near and distant clusters.

In addition, the data was analyzed using k-means clustering [174] with 2 clusters which found a division line between the near and far away subpopulation (color coding in Fig. 7.12) of the data at 240 μm in accordance to the sigmoidal fit. Having an estimate for the maximal interaction distance between C and R clusters, enabled comparison of R-ROIs whose distance to the nearest C-cluster was larger or smaller than a cut-off distance d_0. A value of $d_0 = 200$ pixel $= 258$ μm was chosen for this purpose.
First focusing on the local neighborhood of R-ROIs, one finds that the local composition is indeed significantly different in cases in which a C cluster was nearby (distance $< d_0$) compared to cases in which the nearest C cluster was distant (distance $> d_0$). Analyzing the final S fraction in R-ROIs, one found significantly lower values in R-ROIs that were closer than the cut-off distance compared to ROIs more distant to the nearest C cluster (see Fig. 7.13 a). This effect was most prominent for the uninduced case (0.0 μg/ml MitC) but qualitatively similar for the other cases. The negative distance dependent effect of C on the S abundance could be interpreted as local toxin action. Only if R-ROIs originate from clusters that are near enough to the neighboring C clusters, the toxin can act, kill the S strain, and lead to a decrease in relative S abundance. Especially in the uninduced case, it was evident that without nearby C clusters, S largely dominated in R-ROIs.

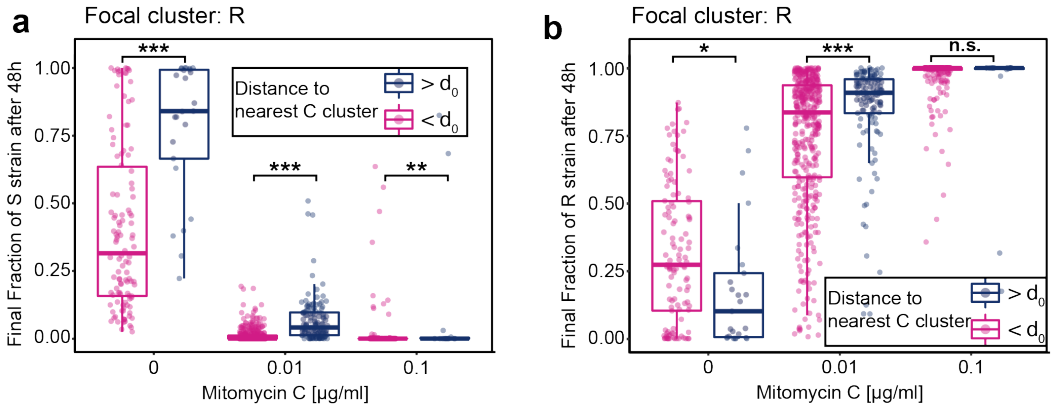

Figure 7.13.: Local cheating

Final relative S (**a**) and R (**b**) abundance in R-ROIs are depicted for various inducer concentrations for the cases that the R-ROIs originate from R clusters that were closer (magenta) or more distant (blue) than the cut-off distance d_0 from the nearest C cluster at 12 hours.

To explicitly investigate the locality of cheating, the above investigation was repeated for the fraction of R in R-ROIs (see Fig. 7.13 b). As expected, one found a significant local increase in R fraction in the uninduced case. This illustrated the distance dependence of cheating which is assumed to originate from a limited toxin range. Interestingly,

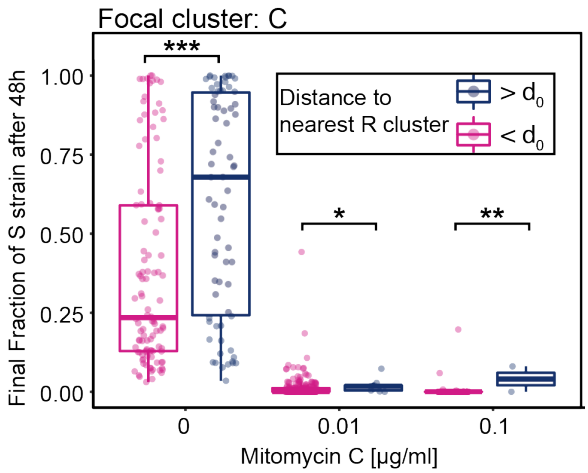

Figure 7.14.: Shielding interaction not verified
Final relative S abundance in C-ROIs is depicted for various inducer concentrations for the cases that the C-ROIs originate from C clusters that were closer (magenta) or more distant (blue) than the cut-off distance d_0 from the nearest R cluster at 12 hours.

for the weakly induced case, in which C was most successful, proximity of C clusters had a significant negative effect of local R abundance. This is attributed to the global killing of S cells by C's toxin action and subsequent direct competition between R and C. At high induction, C's early toxin action was so strong that the distance dependence between C and R was insignificant

Taken together, the toxin action of C on S was distance dependent which translated into a distance dependence in the higher order cheating interaction under conditions, in which suppression of S was necessary (no and high induction).

Finally, the data should reveal if proximity of an R strain was sufficient to rescue the S strain from dieing through the toxin, i.e. if R could shield S from C. However, by using a similar approach as before, no shielding effects could be observed (see Fig. 7.14). On the contrary, the final S abundance in C-ROIs was significantly lower if C-ROIs were originally near an R cluster compared to those that were more distant than the cut-off distance d_0 (no induction). This is assumed to stem from an increased competition by the R strain in the vicinity which further suppressed the S strain. In the cases of low and high induction, no large S abundances and therefore no differences could be observed. This approach certainly has its weaknesses, as it did not consider the relative positioning of cells. Nonetheless, no other indication of shielding was found in the experimental data.

Taken together, this investigation showed that the neighborhood has significant influence on the long-term development within the considered clusters. The relative positioning of clusters itself originates from the random initial patterning. Consequently, also in the second competition phase, the initial randomness influences competition.

7.5. Conclusion

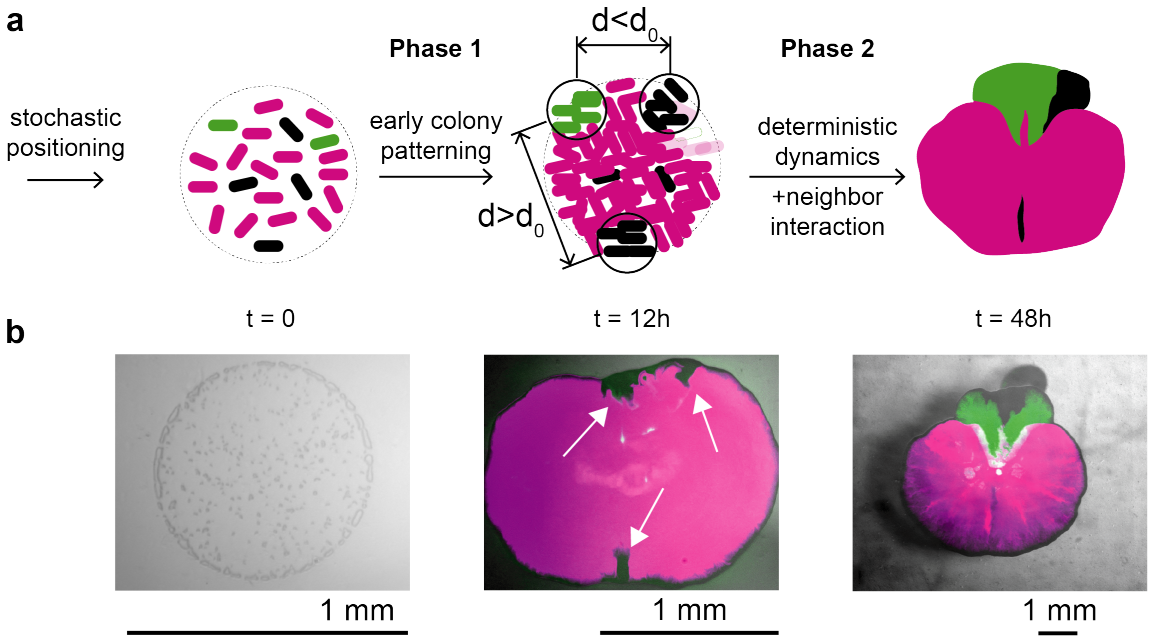

Figure 7.15.: Three-strain interaction model

a The extended three-strain interaction model is similar to what was found for the two strain interaction (Fig. 6.18): after an initial stochastic phase, largely deterministic dynamics determine colony growth and competition outcome. However, the distance dependent neighbor interaction between R (black) and C (green) creates a prolonged feedback of early patterning to the following dynamics: R clusters nearer than cut-off distance d_0 can profit from the toxin of C, while R cluster farer away than d_0 do not. **b** Example (0.0 μg/ml MitC) that illustrates the schematic model shows successful establishment of a mixed C-R cluster in the upper part, while the lower R colony was distant from C, could not profit from the toxin and subsequently was enclosed by S (magenta).

In this chapter, the extended competition dynamics featuring a third resistant strain were investigated. The most obvious effect arising from the third resistant strain is that even under conditions in which R is slower than both S and C, R can dominate large fractions after 48 hours of competition due to cheating.
It was shown that the outcome multi-stability observed in the two-strain interaction was replaced by a local variability that led to locally significantly different outcomes compared to the global competition outcome. The reduced global variability in competition outcome compared to the S-C competition can be attributed to the change in experimental conditions (6-fold higher initial volume). Arguably, two factors are responsible; first, increased spatial dimensions prevented individual toxin release events to influence

the community globally, and second, increased cell numbers reduce influence of single cell events.
Again, the interaction dynamics could be divided into a first, stochastic phase of initial colony patterning and a second largely deterministic phase (see Fig. 7.15). Similar compared to the two-strain interaction, the variables describing the colony at 12 hours in combination with the external stress parameters predicted the competition outcome well.
However, due to the distance dependent cheating interaction, the local competition is strongly influenced by the neighborhood. As a consequence, the random initial patterning has an ongoing influence of the competition dynamics which is new compared to the two-strain interaction (see Fig. 7.15).
Just recently, the importance of fluctuations in initial positioning was shown in another bacterial system. Under typically non-survivable conditions (insufficient average density), random density fluctuations created local accumulations that transcended the critical density [175].
An earlier study investigating the CRS systems [100] already revealed complex dependencies of the competition outcome on various parameters such as initial ratios, toxin production level and C-R distance. A distance dependence of similar qualitative form was found but with a clearly higher cut-off distance which might be explained by differences in the experimental methods - here, having microscopic initial conditions and subsequently smaller cell numbers delivered shorter distances.
However, overall, the results confirmed these earlier findings, and in addition, the multiscale approach employed here allowed to analyze the interaction in more detail. First, the bacterial community after initial patterning could be resolved and the ensuing dynamics predicted with the microscopic variables. Second, information on the local cluster formation could only be obtained by recording the interaction dynamics over multiple scales. Macroscopic end-point measurements would have ignored the existence of non-surviving clusters completely and hindered the correct conditioning on neighboring clusters.
While the cheating interaction could be investigated in detail, the proposed microscopic shielding mechanism could not be observed. Although potential shielding mechanisms are expected to emerge at least under conditions when the separation between C and S by R is larger than the toxin range, an earlier study could find effective shielding only for actively toxin degrading R strains [171]. Systematic variation of relative positioning is possible on an intermediate scale (initial colony diameter $\approx 450\mu m$, minimal distance $\approx 50\mu m$) by using the presented sample preparation technique and could help testing conditions for shielding.
In conclusion, the extended system introduces cheating as a new interaction mechanism compared to the system investigated in chapter 6. While this new interaction influences the competition outcome globally, the most important effects are local. In contrast to

the CS interaction, the spatial dimensions are larger and cheating creates a local coupling between neighboring clusters. Consequently, the competition outcome does not only vary locally but depends on the neighborhood which originates from the initial random positioning.

8. Conclusion and outlook

In this thesis, a novel approach for the investigation of mixed bacterial communities has been introduced that enables the analysis of bacterial interactions on various spatial scales. This approach relies on the combination of nanoliter-precision arrangement of initial communities on agar medium and zooming fluorescence microscopy. By bridging the scales between micro and macro, it is especially suited to investigate the effects of stochastic single-cell events on the macro-dynamics of bacterial interactions.
Consequently, this approach was applied to the bacterial Colicin E2 interaction system. First, the two-strain interaction of the toxin producer and the sensitive strain was investigated before the system was extended with the third resistant strain for a second study. Taken together, both investigated systems, the two- and the three-strain interaction, highlight the close connection between early stochastic and later deterministic phases in bacterial competition. In doing so, the thesis explicitly confirmed how stochastic events at the single-cell level can propagate through large-scale systems determining their long-term behavior. As such, the work is not only relevant for the Colicin system investigated here but has consequences for many systems in which the individual constituents are subject to stochastic state switches.
In a broader context, this thesis contributes to a quantitative approach to the understanding of biological systems that tries to use simple model systems and manageable *physical* models [8] to explain the seemingly irreducible complexity of life's phenomena. These investigated phenomena include but are not restricted to fundamental dynamical properties of cellular processes [8], active matter properties of cell collectives [176, 177], spatio-temporal pattern formation [128, 178, 179], or the quest in understanding the evolutionary principles and the origin of life itself [63].
Since the early years of biophysics, microbial model systems served as toy models for understanding more general principles; one of the most prominent examples being the Luria-Delbrueck study [180] that proofed the spontaneity of mutations by thoroughly analyzing distributions of bacterial mutants. Likewise only in the last four years, the time-frame of this thesis, a large number of studies contributed to the our understanding of microbial systems by combining experimental insights with physical modeling.
The composition of microbial assemblies is increasingly seen as the result of complex, interacting dynamical systems [12] which are preferably reduced to simple systems [107, 114], or even created *de novo* by artificially coupling isolated cells [181]. More and more studies highlight the importance of considering the whole range of com-

plexity "From Genes to Ecosystems" [26] in order to understand these interactions. And - like in this thesis - it is increasingly acknowledged that population behavior and the associated interactions can emerge from single-cell heterogeneity [72]. The individuality of cells has interesting effects in particular under non-linear growth conditions [175], when phenotypic heterogeneity plays a role [21], or under combined random and mechanically driven growth [179].

This appreciation of single-cell heterogeneity has been driven by advancements in experimental techniques since the last 20 years. A steady improvement in experimental and data analysis techniques now increasingly allows to relate single-cell behavior to large scale community behavior [182].

The approach presented in this thesis contributes to a similar effort by bridging the gap between single-cell and macroscopic colony studies. In general, the systems to be investigated using the multi-scale approach profit the most if they combine effects on different length scales. The following examples are currently studied or would be worthwhile future endeavors.

A series of recent studies revealed the elaborate machinery of colicin E2 producing bacteria to coordinate the time points of toxin production and a delayed release [20, 91, 92]. Knowledge on the multi-scale competition dynamics could elucidate the evolutionary purpose of this delay.

Biofilm forming bacteria represent another type of microbial systems that features interesting relations between micro-scale composition and macro-scale behavior. Among others, one particularly suitable example is cooperativity in biofilm formation. Recently, cooperative biofilm formation has been found to function optimally at a fixed ratio of two labor dividing subpopulations [153]. The approach presented here could aid in resolving how the ratio influences the cooperation by tracking the dynamics during the different phases of biofilm formation.

Overall, the main achievements of this thesis are two-fold; first, developing the multi-scale experimental approach and, second, the explicit confirmation of how stochastic events at the single-cell level can propagate through large-scale systems determining their long-term behavior. Although the role of noise and stochasticity is stressed in most modern textbook on biological physics [6, 8, 183, 184], the consequences of population level stochasticity for bacterial competition have been largely unexplored, experimentally. This thesis closes this gap and shows, how stochastic effects can have dramatic effects during competition.

A. Appendix for chapter 6

A.1. Experimental settings

	Zoom Level			
Experimental Parameter	**1**	**2**	**3**	**4**
Magnification	15.75	10	5	2.2
$T_{Start}[h:min]$	00:00	12:15	18:30	33:30
Δt[min]	15	15	60	60
Pixel size [μm]	0.819	1.29	2.58	5.86
Bright field intensity [%]	9	5	5	5
Bright field signal gain	1	1	1	1
Bright field exposure time [ms]	7.3	5	2.1	1.9
RFP excitation intensity [%]	100	100	100	100
RFP signal gain	46	9.6	1	1
RFP exposure time [ms]	2000	2000	2000	1000
GFP excitation intensity [%]	100	100	100	100
GFP signal gain	46	9.6	1	1
GFP exposure time [ms]	2000	2000	2000	1000

Table A.1.: Microscope configuration settings for CS interaction experiments
Overview of microscope configuration and image acquisition settings for two-strain interaction (chapter 6).

A.2. Strain growth rates

	Linear Area Growth Rate from Control Experiments [$\mu m^2/h$ (relative standard deviation)]					
MitC concentration [μg/ml]	CpMO3	Srfp	Snfp	Rrfp	Rnfp	Syfp
0	395660 (9.1%)	329590 (20.1%)	-	-	-	-
0.005	393060 (3.4%)	303940 (10.3%)	597810 (19.1%)	202980 (3.0%)	475810 (15.8%)	400368.6 (5.6%)
0.01	326490 (16.1%)	254980 (10.4%)	-	-	-	-
0.1	86041 (30.8%)	334940 (22.6%)	-	-	-	-
Simulation growth rate r_X	0.0729	0.0607	0.1101	0.0374	0.0876	0.0742

Table A.2.: Linear area expansion rates

Experimentally determined linear area growth rates and corresponding model growth rates.

A.3. Statistics for linear modeling of competition data

	Standardized Coefficient	Standard Error of Coefficient	t Value	p Value
(Intercept)	3.22E-16	0.04238745	7.60E-15	1.00E+00
$N_{C,0}$	2.14E-01	0.07033569	3.05E+00	2.50E-03
$R_{C,0}$	2.60E-01	0.05267524	4.94E+00	1.23E-06
$D_{C,0}$	3.22E-01	0.07469537	4.31E+00	2.20E-05
MitC [μg/ml]	-4.66E-01	0.04250229	-1.10E+01	4.58E-24
Linear regression result				
$R^2 = 0.4071$		$R^2_{adjusted} = 0.3999$		
$F(4, 329) = 56.48$		Mean-square error= 0.600	$p < 2.2 \cdot 10^{-16}$	

Table A.3.: Regression results of linear model for $N_{C,Edge}$

Regression results for linear models used in chapter 6. Influence of various spatial parameters was modeled according to equation 6.3.

Model	Multiple R^2	Adjusted $R^2_{adjusted}$	F value	Mean-square error	p value
Experimental data	0.7452	0.723	$F(24, 275) = 33.51$	0.05785	<2.2e-16
Simulation data	0.9314	0.9283	$F(340, 7580) = 302.6$	0.0149	<2.2e-16

Table A.4.: Regression results of linear model for F_C

Regression results for linear models used in chapter 6. Experimental data was modeled according to equation 6.6 and simulation data according to equation 6.7.

ANOVA Table

Factor	Degrees of Freedom	Sum of Squares Type I	Mean Square	F Value	p Value	η^2
MitC	3	34.262199	11.420733	197.40889	< 2.2e-16	0.5487
$N_{C,Edge}$	1	9.3107	9.3107	160.93613	< 2.2e-16	0.1491
$N_{C,0}$	1	0.0790778	0.0790778	1.366869	2.43E-01	0.0013
$D_{C,0}$	1	0.0142288	0.0142288	0.245947	6.20E-01	0.0002
$R_{C,0}$	1	0.0201465	0.0201465	0.348236	5.56E-01	0.0003
MitC:$N_{C,Edge}$	2	0.5892032	0.2946016	5.092228	6.74E-03	0.0094
MitC:$N_{C,0}$	3	0.1722393	0.0574131	0.992393	3.97E-01	0.0028
MitC:$D_{C,0}$	3	0.0397318	0.0132439	0.228923	8.76E-01	0.0006
MitC:$R_{C,0}$	3	0.1678944	0.0559648	0.967359	4.09E-01	0.0027
$N_{C,Edge}$:$N_{C,0}$	1	1.7496308	1.7496308	30.242600	8.71E-08	0.0280
$N_{C,Edge}$:$D_{C,0}$	1	0.0013687	0.0013682	0.023659	8.78E-01	0.00002
$N_{C,Edge}$:$R_{C,0}$	1	0.0012870	0.0012870	0.022246	8.82E-01	0.00002
$N_{C,0}$:$D_{C,0}$	1	0.1060044	0.1060044	1.832300	1.77E-01	0.0017
$N_{C,0}$:$R_{C,0}$	1	0.0187043	0.0187043	0.323306	5.70E-01	0.0003
$D_{C,0}$:$R_{C,0}$	1	0.0006923	0.0006923	0.011967	9.13E-01	0.00001
Residuals	275	15.909626	0.0578532			

Table A.5.: ANOVA Table Experiment

ANOVA table of linear regression model used in chapter 6 for experimental data.

ANOVA Table

Factor	Degrees of Freedom	Sum of Squares Type I	Mean Square	F Value	p Value	η^2
s_C	16	725.993674	45.374605	3045.12377	< 2.2e-16	0.441036329
$N_{C,Edge}$	4	733.303964	183.325991	12303.14485	< 2.2e-16	0.445477282
IC	15	5.573827	0.37158843	24.937579	< 2.2e-16	0.003386063
s_C:$N_{C,Edge}$	46	52.042897	1.13136732	75.92691	< 2.2e-16	0.031615714
$N_{C,Edge}$:IC	19	4.13388	0.21757261	14.601461	< 2.2e-16	0.002511304
s_C:IC	240	12.112686	0.05046953	3.387048	< 2.2e-16	0.007358376
Residuals	7580	112.947627	0.01490074			

Table A.6.: ANOVA Table Simulation

ANOVA table of linear regression model used in chapter 6 for simulated data.

B. Appendix for chapter 7

B.1. Experimental settings

	Zoom Level			
Experimental Parameter	**1**	**2**	**3**	**4**
Magnification	15.75	10	5	2.2
$T_{Start}[h:min]$	00:00	09:15	13:30	26:30
Δt[min]	15	15	60	60
Pixel size [μm]	0.819	1.29	2.58	5.86
Bright field intensity [%]	9	5	5	5
Bright field signal gain	1	1	1	1
Bright field exposure time [ms]	7.3	5	2.1	1.9
RFP excitation intensity [%]	100	100	100	100
RFP signal gain	46	9.6	1	1
RFP exposure time [ms]	2000	2000	2000	1000
GFP excitation intensity [%]	100	100	100	100
GFP signal gain	46	9.6	1	1
GFP exposure time [ms]	2000	2000	2000	1000

Table B.1.: Microscope configuration settings for RCS interaction experiments
Overview of microscope configuration and image acquisition settings for two-strain interaction (chapter 7).

B.2. Strain growth rates

	Linear Area Growth Rate from Control Experiments $[mm^2/h$ (relative standard deviation)]		
MitC concentration [μg/ml]	CpMO3	Srfp	Rnfp
0	0.385 (11.6%)	0.358 (13.7%)	0.329 (9.5%)
0.01	0.305 (12.0%)	0.464 (9.1%)	0.291 (13.2%)
0.1	-	0.604 (13.7%)	0.281 (10.3%)
Simulation growth rate r_X	0.0709	0.066	0.0606

Table B.2.: Linear area expansion rates

Experimentally determined linear area growth rates and corresponding model growth rates for CRS competition.

B.3. Statistics for competition data

	Correlation between 12h variables and F_i in terms of Pearson's r and (p value)		
MitC concentration [μg/ml]	$N_{R,Edge}$	$N_{C,Edge}$	A_S^{12h}
0	0.18 (0.12)	0.13 (0.26)	0.56 (<0.001)
0.01	0.37 (0.002)	0.64 (<0.001)	0.63 (<0.001)
0.1	0.08 (0.48)	0.35 (<0.001)	0.78 (<0.001)

Table B.3.: Correlation of early phase variables and

Correlation data for figure 7.8.

	Estimated Coefficient	Standard Error of Coefficient	t Value	p Value
(Intercept)	0.3129	0.0863	3.6264	0.0004
mitC 0.01	-0.4041	0.0549	-7.3545	0.0000
mitC 0.1	-0.2066	0.0784	-2.6346	0.0090
$N_{C,Edge}$	-0.0093	0.0047	-2.0070	0.0460
A_S^{12h}	3.56565E-07	4.65742E-08	7.65585223	5.69236E-13
$N_{R,Edge}$	-0.001	0.003	-0.496	0.620
Linear regression result				
$R^2 = 0.926$				
$F(5, 225) = 560.3$		$p < 2.2 \cdot 10^{-16}$		

Table B.4.: Regression results of linear model for F_S

	Estimated Coefficient	Standard Error of Coefficient	t Value	p Value
(Intercept)	0.513	0.102	5.028	0.000
mitC 0.01	0.341	0.065	5.241	0.000
mitC 0.1	0.346	0.093	3.727	0.000
$N_{C,Edge}$	-0.010	0.006	-1.734	0.084
A_S^{12h}	-2.74E-07	5.51E-08	-4.965120378	1.36E-06
$N_{R,Edge}$	0.006	0.003	1.904	0.058
Linear regression result				
$R^2 = 0.891$				
$F(5, 225) = 366.2$		$p < 2.2 \cdot 10^{-16}$		

Table B.5.: Regression results of linear model for F_R

	Estimated Coefficient	Standard Error of Coefficient	t Value	p Value
(Intercept)	0.174	0.062	2.813	0.005
mitC 0.01	0.063	0.039	1.612	0.108
mitC 0.1	-0.139	0.056	-2.478	0.014
$N_{C,Edge}$	0.019	0.003	5.664	0.000
A_S^{12h}	-8.30095E-08	3.33625E-08	-2.488104289	0.013571254
$N_{R,Edge}$	-0.005	0.002	-2.451	0.015
Linear regression result				
$R^2 = 0.5952$				
$F(5, 225) = 65.87$		$p < 2.2 \cdot 10^{-16}$		

Table B.6.: Regression results of linear model for F_C

List of publications

Publications based on the results of this thesis:

[B1] **Benedikt von Bronk**, Sophia Anna Schaffer, Alexandra Götz, Madeleine Opitz (2017). Effects of Stochasticity and Division of Labor in Toxin Production on Two-strain Bacterial Competition in *Escherichia coli*. *PLoS Biology* 15(5): e2001457

[B2] **Benedikt von Bronk**, Alexandra Götz, Madeleine Opitz (2018). Complex microbial systems across different levels of description. *Physical Biology* 15: 051002

[B3] **Benedikt von Bronk**, Alexandra Götz, Madeleine Opitz (2018). Locality of interactions in three-strain bacterial competition in *E. coli*. *(accepted for publication in Physical Biology)*

Publications that are closely related to the investigations for this thesis:

[M1] Andreas Mader, **Benedikt von Bronk**, Benedikt Ewald, Sara Kesel, Karin Schnetz, Erwin Frey, Madeleine Opitz (2015). Amount of Colicin Release in Escherichia coli Is Regulated by Lysis Gene Expression of the Colicin E2 Operon. *PLoS ONE* 10(3): e0119124

[K1] Sara Kesel, **Benedikt von Bronk**, Carolina Falcon Garcia, Alexandra Götz, Oliver Lieleg and Madeleine Opitz (2017). Matrix composition determines dimensions of Bacillus subtilis NCIB 3610 biofilm colonies grown on LB agar. *RSC Advances* 7: 31886-31898

[G1] Alexandra Götz, Matthias Lechner, Andreas Mader, **Benedikt von Bronk**, Erwin Frey and Madeleine Opitz (2018). CsrA and its regulators control the timepoint of ColicinE2 release in *Escherichia coli*. *Scientific Reports* 8: 6537

[G2] Alexandra Götz, Andreas Mader, **Benedikt von Bronk**, Anna Weiß, Madeleine Opitz (2018). Gene expression noise in the ColicinE2 stress response system of *Escherichia coli*. *(in preparation)*

[S1] Almond Stöcker, Sarah Brockhaus, Sophia Schaffer, **Benedikt von Bronk**, Madeleine Opitz, Sonja Greven (2018). Boosting Functional Response Models for Location, Scale and Shape with an Application to Bacterial Competition. *(submitted for publication, preprint available https://arxiv.org/abs/1809.09881)*

Bibliography

[1] B. von Bronk, A. Götz, and M. Opitz, "Complex microbial systems across different levels of description," *Physical Biology*, vol. 15, p. 051002, 2018.

[2] M. Kardar, *Statistical Physics of Particles*. New York: Cambridge University Press, 2007.

[3] P. Anderson, "More Is Different," *Science*, vol. 177, no. 4047, pp. 393–396, 1972.

[4] S. Kivelson and S. A. Kivelson, "Defining emergence in physics," *npj Quantum Materials*, vol. 1, no. 1, p. 16024, 2016.

[5] H. Meyer-Ortmanns, "On the Success and Limitations of Reductionism in Physics," in *Why More Is Different* (B. Falkenburg and M. Morrison, eds.), ch. 2, pp. 13–39, Berlin Heidelberg: Springer-Verlag, 2015.

[6] W. Bialek, *Biophysics - Searching for principles*. Princeton: Princeton University Press, 2012.

[7] L. S. Tsimring, "Noise in biology," *Reports on Progress in Physics*, vol. 77, no. 2, p. 026601, 2014.

[8] P. Nelson, *Physical Models of Living Systems*. New York: W. H. Freeman and Company, 2015.

[9] H. V. Westerhoff, J. S. Lolkema, R. Otto, and K. J. Hellingwerf, "Thermodynamics of growth non-equilibrium thermodynamics of bacterial growth the phenomenological and the Mosaic approach," *Biochimica et Biophysica Acta*, vol. 683, no. 3-4, pp. 181–220, 1982.

[10] M. Delarue, J. Hartung, C. Schreck, P. Gniewek, L. Hu, S. Herminghaus, and O. Hallatschek, "Self-driven jamming in growing microbial populations," *Nature Physics*, vol. 12, no. 8, pp. 762–766, 2016.

[11] T. Earnest, J. A. Cole, and Z. Luthey-Schulten, "Simulating Biological Processes: Stochastic Physics from Whole Cells to Colonies," *Reports on Progress in Physics*, vol. 81, p. 052601, 2018.

[12] S. Widder, R. J. Allen, T. Pfeiffer, T. P. Curtis, C. Wiuf, W. T. Sloan, O. X. Cordero, S. P. Brown, B. Momeni, W. Shou, H. Kettle, H. J. Flint, A. F. Haas, B. Laroche, and J.-u. Kreft, "Challenges in microbial ecology: building predictive

understanding of community function and dynamics.," *The ISME Journal*, vol. 10, pp. 2557–2568, 2016.

[13] K. Faust and J. Raes, "Microbial interactions: From networks to models," *Nature Reviews Microbiology*, vol. 10, no. 8, pp. 538–550, 2012.

[14] M. Riley and M. Chavan, *Bacteriocins: Ecology and Evolution*. Berlin Heidelberg: Springer-Verlag, 2007.

[15] B. Kerr, M. A. Riley, M. W. Feldman, and B. J. M. Bohannan, "Local dispersal promotes biodiversity in a real-life game of rock-paper-scissors.," *Nature*, vol. 418, no. 6894, pp. 171–174, 2002.

[16] T. Reichenbach, M. Mobilia, and E. Frey, "Mobility promotes and jeopardizes biodiversity in rock-paper-scissors games.," *Nature*, vol. 448, no. 7157, pp. 1046–1049, 2007.

[17] H. Ozeki, B. A. D. Stocker, and H. De Margerie, "Production of colicine by single bacteria," *Nature*, vol. 183, pp. 337–339, 1959.

[18] M. Ackermann, "A functional perspective on phenotypic heterogeneity in microorganisms," *Nature Reviews Microbiology*, vol. 13, no. 8, pp. 497–508, 2015.

[19] N. Moris, C. Pina, and A. M. Arias, "Transition states and cell fate decisions in epigenetic landscapes," *Nature Reviews Genetics*, vol. 17, no. 11, pp. 693–703, 2016.

[20] A. Mader, B. von Bronk, B. Ewald, S. Kesel, K. Schnetz, E. Frey, and M. Opitz, "Amount of Colicin Release in Escherichia coli Is Regulated by Lysis Gene Expression of the Colicin E2 Operon," *PLoS One*, vol. 10, no. 3, p. e0119124, 2015.

[21] B. Bayramoglu, D. Toubiana, S. van Vliet, R. F. Inglis, N. Shnerb, and O. Gillor, "Bet-hedging in bacteriocin producing Escherichia coli populations: the single cell perspective," *Scientific Reports*, vol. 7, p. 42068, 2017.

[22] E. Cascales, S. K. Buchanan, D. Duché, C. Kleanthous, R. Lloubès, K. Postle, M. Riley, S. Slatin, and D. Cavard, "Colicin biology.," *Microbiology and molecular biology reviews : MMBR*, vol. 71, no. 1, pp. 158–229, 2007.

[23] J. C. W. Locke and M. B. Elowitz, "Using movies to analyse gene circuit dynamics in single cells.," *Nature Reviews Microbiology*, vol. 7, no. 5, pp. 383–92, 2009.

[24] J. W. Young, J. C. W. Locke, A. Altinok, N. Rosenfeld, T. Bacarian, P. S. Swain, E. Mjolsness, and M. B. Elowitz, "Measuring single-cell gene expression dynamics in bacteria using fluorescence time-lapse microscopy.," *Nature protocols*, vol. 7, no. 1, pp. 80–8, 2012.

[25] M. F. Weber, G. Poxleitner, E. Hebisch, E. Frey, and M. Opitz, "Chemical warfare and survival strategies in bacterial range expansions," *Journal of the Royal Society Interface*, vol. 11, no. May, p. 20140172, 2014.

[26] J.-U. Kreft, C. M. Plugge, C. Prats, J. H. J. Leveau, W. Zhang, and F. L. Hellweger, "From Genes to Ecosystems in Microbiology: Modeling Approaches and the Importance of Individuality," *Frontiers in Microbiology*, vol. 8, p. 2299, 2017.

[27] L. Dai, D. Vorselen, K. S. Korolev, and J. Gore, "Generic Indicators for Loss of Resilience Before a Tipping Point Leading to Population Collapse," *Science*, vol. 336, pp. 1175–1177, 2012.

[28] K. Lewis, "Persister cells.," *Annual review of microbiology*, vol. 64, pp. 357–372, 2010.

[29] Creative Commons, "Creative Commons License (CC BY 3.0)," 2018.

[30] R. P. Feynman, R. B. Leighton, and M. Sands, *The Feynman Lectures on Physics, Vol. I: The New Millennium Edition: Mainly Mechanics, Radiation, and Heat.* New York: Basic Books, 2011.

[31] M. H. Van Regenmortel, "Reductionism and complexity in molecular biology," *EMBO reports*, vol. 5, no. 11, pp. 1016–1020, 2004.

[32] B. Falkenburg and M. Morrison, *Why More Is Different.* Berlin Heidelberg: Springer-Verlag, 2015.

[33] T. Vicsek and A. Zafeiris, "Collective motion," *Physics Reports*, vol. 517, no. 3-4, pp. 71–140, 2012.

[34] J. van Gestel, H. Vlamakis, and R. Kolter, "From Cell Differentiation to Cell Collectives: Bacillus subtilis Uses Division of Labor to Migrate," *PLoS Biology*, vol. 13, no. 4, p. e1002141, 2015.

[35] H.-C. Flemming, J. Wingender, U. Szewzyk, P. Steinberg, S. A. Rice, and S. Kjelleberg, "Biofilms: an emergent form of bacterial life," *Nature Reviews Microbiology*, vol. 14, no. 9, pp. 563–575, 2016.

[36] F. Crick, "Central dogma of molecular biology.," *Nature*, vol. 227, no. 5258, pp. 561–563, 1970.

[37] F. Jacob and J. Monod, "Genetic Regulatory Mechanisms in the Synthesis of Proteins," *J. Mol. Biol*, vol. 3, pp. 318–356, 1961.

[38] M. Verma, S. Rawool, P. J. Bhat, and K. V. Venkatesh, "Biological significance of autoregulation through steady state analysis of genetic networks," *BioSystems*, vol. 84, no. 1, pp. 39–48, 2006.

[39] C. Vogel and E. M. Marcotte, "Insights into the regulation of protein abundance from proteomic and transcriptomic analyses," *Nature Reviews Genetics*, vol. 13, no. 4, pp. 227–232, 2012.

[40] S. H. Strogatz, "Exploring complex networks," *Nature*, vol. 410, no. 6825, pp. 268–276, 2001.

[41] U. S. Bhalla and R. Iyengar, "Emergent Properties of Networks of Biological Signalling Pathways," *Science*, vol. 283, no. 5400, pp. 381–387, 1999.

[42] E. Alm and A. P. Arkin, "Biological networks," *Current Opinion in Structural Biology*, vol. 13, no. 2, pp. 193–202, 2003.

[43] S. S. Shen-Orr, R. Milo, S. Mangan, and U. Alon, "Network motifs in the transcriptional regulation network of Escherichia coli," *Nature Genetics*, vol. 31, no. 1, pp. 64–68, 2002.

[44] R. Milo, S. Shen-Orr, S. Itzkovitz, N. Kashtan, D. Chklovskii, and U. Alon, "Network Motif: Simple Building Blocks of Complex Networks," *Science*, vol. 298, no. 5594, pp. 824–827, 2002.

[45] U. Alon, "Network motifs: theory and experimental approaches.," *Nature Reviews Genetics*, vol. 8, no. 6, pp. 450–461, 2007.

[46] M. B. Elowitz and S. Leibler, "A synthetic oscillatory network of transcriptional regulators.," *Nature*, vol. 403, no. 6767, pp. 335–338, 2000.

[47] T. S. Gardner, C. R. Cantor, and J. J. Collins, "Construction of a genetic toggle switch in Escherichia coli.," *Nature*, vol. 403, no. 6767, pp. 339–342, 2000.

[48] E. M. Ozbudak, M. Thattai, H. N. Lim, B. I. Shraiman, and A. Van Oudenaarden, "Multistability in the lactose utilization network of Escherichia coli.," *Nature*, vol. 427, no. 6976, pp. 737–740, 2004.

[49] G. M. Süel, R. P. Kulkarni, J. Dworkin, J. Garcia-Ojalvo, and M. B. Elowitz, "Tunability and Noise Dependence in Differentiation Dynamics," *Science*, vol. 315, no. 5819, pp. 1716–1719, 2007.

[50] M. B. Elowitz, A. J. Levine, E. D. Siggia, and P. S. Swain, "Stochastic gene expression in a single cell.," *Science*, vol. 297, pp. 1183–1186, 2002.

[51] A. Eldar and M. B. Elowitz, "Functional roles for noise in genetic circuits.," *Nature*, vol. 467, no. 7312, pp. 167–173, 2010.

[52] D. T. Gillespie, "Stochastic Simulation of Chemical Kinetics," *Annual Review of Physical Chemistry*, vol. 58, pp. 35–55, 2007.

[53] D. A. McQuarrie, "Stochastic approach to chemical kinetics," *Journal of Applied Probability*, vol. 4, pp. 413–478, 1967.

[54] D. T. Gillespie, "Exact Stochastic Simulation of Coupled Chemical Reactions," *The Journal of Physical Chemistry*, vol. 81, no. 25, pp. 2340–2361, 1977.

[55] H. Jeong, B. Tombor, R. Albert, Z. N. Oltvai, and a. L. Barabási, "The large-scale organization of metabolic networks.," *Nature*, vol. 407, no. 6804, pp. 651–654, 2000.

[56] B. Alberts, A. Johnson, J. Lewis, M. Raff, K. Roberts, and P. Walter, *Molecular biology of the cell*. NewYork: Garland Science, 5 ed., 2008.

[57] H. Wang, M. La Russa, and L. S. Qi, "CRISPR/Cas9 in Genome Editing and Beyond," *Annual Review of Biochemistry*, vol. 85, pp. 227–264, 2016.

[58] R. Y. Tsien, "The Green Fluorescent Protein," *Annual Review of Biochemistry*, vol. 67, pp. 509–544, 1998.

[59] O. Shimomura, F. H. Johnson, and Y. Saiga, "Extraction, Purification and Properties of Aequorin, a Bioluminescent Protein from the Luminous Hydromedusan, Aequorea," *Journal of Cellular and Comparative Physiology*, vol. 59, no. 3, pp. 223–239, 1962.

[60] Î. Chalfie, U. Tu, G. Euskirchen, W. W. Ward, and D. C. Prasher, "Green fluorescent protein as a marker for gene expression," *Science*, vol. 263, no. 5148, pp. 802–805, 1994.

[61] D. Longo and J. Hasty, "Dynamics of single-cell gene expression," *Molecular Systems Biology*, vol. 2, p. 64, 2006.

[62] J. R. Tietjen, L. J. Donato, D. Bhimisaria, and A. Z. Ansari, *Sequence-specificity and energy landscapes of DNA-binding molecules*, vol. 497. Elsevier Inc., 2011.

[63] P. Schwille, "How Simple Could Life Be?," *Angewandte Chemie - International Edition*, vol. 56, no. 37, pp. 10998–11002, 2017.

[64] S. J. Altschuler and L. F. Wu, "Cellular Heterogeneity: Do Differences Make a Difference?," *Cell*, vol. 141, no. 4, pp. 559–563, 2010.

[65] D. Wang and S. Bodovitz, "Single cell analysis: The new frontier in 'omics'," *Trends in Biotechnology*, vol. 28, no. 6, pp. 281–290, 2010.

[66] J. M. Gasol and P. A. Del Giorgio, "Using flow cytometry for counting natural planktonic bacteria and understanding the structure of planktonic bacterial communities," *Scientia Marina*, vol. 64, no. 2, pp. 197–224, 2000.

[67] D. Muzzey and A. van Oudenaarden, "Quantitative Time-Lapse Fluorescence Microscopy in Single Cells," *Annual Review of Cell and Developmental Biology*, vol. 25, pp. 301–327, 2009.

[68] J. E. Ferrell, "Bistability, bifurcations, and Waddington's epigenetic landscape," *Current Biology*, vol. 22, no. 11, pp. R458–R466, 2012.

[69] G. Balázsi, A. Van Oudenaarden, and J. J. Collins, "Cellular decision making and biological noise: From microbes to mammals," *Cell*, vol. 144, no. 6, pp. 910–925, 2011.

[70] C. M. Waters and B. L. Bassler, "Quorum Sensing: Cell-to-Cell Communication in Bacteria," *Annual Review of Cell and Developmental Biology*, vol. 21, pp. 319–346, 2005.

[71] H. Youk and W. A. Lim, "Secreting and Sensing the Same Molecule Allows Cells to Achieve Versatile Social Behaviors," *Science*, vol. 343, no. 6171, p. 1242782, 2014.

[72] B. M. C. Martins and J. C. W. Locke, "Microbial individuality: how single-cell heterogeneity enables population level strategies," *Current Opinion in Microbiology*, vol. 24, pp. 104–112, 2015.

[73] H. Vlamakis, Y. Chai, P. Beauregard, R. Losick, and R. Kolter, "Sticking together: building a biofilm the Bacillus subtilis way," *Nature Reviews Microbiology*, vol. 11, no. 3, pp. 157–168, 2013.

[74] J. van Gestel, H. Vlamakis, and R. Kolter, "Division of Labor in Biofilms : the Ecology of Cell Differentiation," *Microbiology Spectrum*, vol. 3, no. 2, pp. MB–0002–2014, 2015.

[75] L. S. Cairns, L. Hobley, and N. R. Stanley-Wall, "Biofilm formation by Bacillus subtilis: New insights into regulatory strategies and assembly mechanisms," *Molecular Microbiology*, vol. 93, no. 4, pp. 587–598, 2014.

[76] D. Lopez, H. Vlamakis, and R. Kolter, "Generation of multiple cell types in Bacillus subtilis," *FEMS Microbiology Reviews*, vol. 33, pp. 152–163, 2009.

[77] M. E. Hibbing, C. Fuqua, M. R. Parsek, and S. B. Peterson, "Bacterial competition: surviving and thriving in the microbial jungle.," *Nature Reviews Microbiology*, vol. 8, pp. 15–25, 2010.

[78] T. G. Whitham, J. K. Bailey, J. A. Schweitzer, S. M. Shuster, R. K. Bangert, C. J. Leroy, E. V. Lonsdorf, G. J. Allan, S. P. DiFazio, B. M. Potts, D. G. Fischer, C. A. Gehring, R. L. Lindroth, J. C. Marks, S. C. Hart, G. M. Wimp, and S. C. Wooley, "A framework for community and ecosystem genetics: From genes to ecosystems," *Nature Reviews Genetics*, vol. 7, no. 7, pp. 510–523, 2006.

[79] S. T. Cole, B. Saint-Joanis, and A. P. Pugsley, "Molecular characterisation of the colicin E2 operon and Identification of Its Products," *Mol Gen Genet*, vol. 198, pp. 465–472, 1985.

[80] O. Gillor, J. A. C. Vriezen, and M. A. Riley, "The role of SOS boxes in enteric bacteriocin regulation," *Microbiology*, vol. 154, no. 6, pp. 1783–1792, 2008.

[81] S. Kamenšek, Z. Podlesek, O. Gillor, and D. Zgur-Bertok, "Genes regulated by the Escherichia coli SOS repressor LexA exhibit heterogeneous expression.," *BMC Microbiology*, vol. 10, p. 283, 2010.

[82] P. Mrak, Z. Podlesek, J. P. M. Van Putten, and D. Žgur-Bertok, "Heterogeneity in expression of the Escherichia coli colicin K activity gene cka is controlled by the SOS system and stochastic factors," *Molecular Genetics and Genomics*, vol. 277, no. 4, pp. 391–401, 2007.

[83] K. G. Hardy and G. G. Meynell, ""Induction" of colicin factor E2-P9 by mitomycin C.," *Journal of Bacteriology*, vol. 112, no. 2, pp. 1007–1009, 1972.

[84] B. Kerr, "The Ecological and Evolutionary Dynamics of Model Bacteriocin Communities," in *Bacteriocins: Ecology and Evolution* (M. Riley and M. Chavan, eds.), pp. 111–134, Berlin Heidelberg: Springer-Verlag, 2007.

[85] Creative Commons, "Creative Commons License (CC BY 4.0)," 2018.

[86] J. A. Wojdyla, S. J. Fleishman, D. Baker, and C. Kleanthous, "Structure of the ultra-high-affinity colicin E2 DNase-Im2 complex," *Journal of Molecular Biology*, vol. 417, no. 1-2, pp. 79–94, 2012.

[87] J. W. Little, S. H. Edmiston, L. Z. Pacelli, and D. W. Mount, "Cleavage of the Escherichia coli lexA protein by the recA protease.," *Proceedings of the National Academy of Sciences of the United States of America*, vol. 77, no. 6, pp. 3225–3229, 1980.

[88] A. P. Pugsley, N. Goldzahl, and R. M. Barker, "Colicin E2 production and release by Escherichia coli K12 and other Enterobacteriaceae," *Journal of General microbiology*, vol. 131, pp. 2673–2686, 1985.

[89] S. Kanoh, H. Masaki, S. Yajima, T. Ohta, and T. Uozumi, "Signal peptide of the colicin E2 lysis protein causes host cell death," *Agricultural and Biological Chemistry*, vol. 55, no. 6, pp. 1607–1614, 1991.

[90] T. Y. Yang, Y. M. Sung, G. S. Lei, T. Romeo, and K. F. Chak, "Posttranscriptional repression of the cel gene of the ColE7 operon by the RNA-binding protein CsrA of Escherichia coli," *Nucleic Acids Research*, vol. 38, no. 12, pp. 3936–3951, 2010.

[91] M. Lechner, M. Schwarz, M. Opitz, and E. Frey, "Hierarchical Post-transcriptional Regulation of Colicin E2 Expression in Escherichia coli," *PLoS Computational Biology*, vol. 12, no. 12, p. e1005243, 2016.

[92] A. Götz, M. Lechner, A. Mader, B. von Bronk, E. Frey, and M. Opitz, "CsrA

and its regulators control the time-point of ColicinE2 release in Escherichia coli," *Scientific Reports*, vol. 8, p. 6537, 2018.

[93] K. Suzuki, P. Babitzke, S. R. Kushner, and T. Romeo, "Identification of a novel regulatory protein (CsrD) that targets the global regulatory RNAs CsrB and CsrC for degradation by RNase E," *Genes and Development*, vol. 20, pp. 2605–2617, 2006.

[94] A. Götz, A. Mader, B. von Bronk, A. Weiß, and M. Opitz, "Gene expression noise in the ColicinE2 stress response system of Escherichia coli (in preparation)," 2018.

[95] L. Ghazaryan, M. I. M. Soares, and O. Gillor, "Auto-regulation of DNA degrading bacteriocins: Molecular and ecological aspects," *Antonie van Leeuwenhoek, International Journal of General and Molecular Microbiology*, vol. 105, no. 5, pp. 823–834, 2014.

[96] L. Chao and B. R. Levin, "Structured habitats and the evolution of anticompetitor toxins in bacteria.," *Proceedings of the National Academy of Sciences of the United States of America*, vol. 78, no. 10, pp. 6324–6328, 1981.

[97] S. A. Frank, "Spatial polymorphism of bacteriocins and other allelopathic traits," *Evolutionary Ecology*, vol. 8, no. 4, pp. 369–386, 1994.

[98] B. C. Kirkup and M. A. Riley, "Antibiotic-mediated antagonism leads to a bacterial game of rock-paper-scissors in vivo.," *Nature*, vol. 428, no. 6981, pp. 412–414, 2004.

[99] R. Durrett and S. Levin, "Allelopathy in Spatially Distributed Populations," *Journal of Theoretical Biology*, vol. 185, no. 2, pp. 165–171, 1997.

[100] Y. Gerardin, M. Springer, and R. Kishony, "A competitive trade-off limits the selective advantage of increased antibiotic production," *Nature Microbiology*, vol. 1, p. 16175, 2016.

[101] Y. Iwasa, M. Nakamaru, and S. A. Levin, "Allelopathy of bacteria in a lattice population: Competition between colicin-sensitive and colicin-producing strains," *Evolutionary Ecology*, vol. 12, no. 7, pp. 785–802, 1998.

[102] H. A. Orr, "Fitness and its role in evolutionary genetics," *Nature Reviews Genetics*, vol. 10, no. 8, pp. 531–539, 2009.

[103] M. J. I. Müller, B. I. Neugeboren, D. R. Nelsona, and A. W. Murray, "Genetic drift opposes mutualism during spatial population expansion," *Proceedings of the National Academy of Sciences*, vol. 111, no. 3, pp. 1037–1042, 2014.

[104] S. Rakoff-Nahoum, K. R. Foster, and L. E. Comstock, "The evolution of cooperation within the gut microbiota," *Nature*, vol. 533, pp. 255–259, 2016.

[105] K. Z. Coyte, J. Schluter, and K. R. Foster, "The ecology of the microbiome: Networks, competition, and stability," *Science*, vol. 350, no. 6261, pp. 663–666, 2015.

[106] N. M. Oliveira, R. Niehus, and K. R. Foster, "Evolutionary limits to cooperation in microbial communities," *Proceedings of the National Academy of Sciences*, vol. 111, no. 50, pp. 17941–17946, 2014.

[107] J. Friedman and J. Gore, "Ecological systems biology: The dynamics of interacting populations," *Current Opinion in Systems Biology*, vol. 1, pp. 114–121, 2017.

[108] W. Z. Lidicker, "A Clarification of Interactions in Ecological Systems," *BioScience*, vol. 29, no. 8, pp. 475–477, 1979.

[109] K. R. Foster and T. Bell, "Competition, not cooperation, dominates interactions among culturable microbial species," *Current Biology*, vol. 22, no. 19, pp. 1845–1850, 2012.

[110] N. M. Oliveira, E. Martinez-Garcia, J. Xavier, W. M. Durham, R. Kolter, W. Kim, and K. R. Foster, "Biofilm Formation As a Response to Ecological Competition," *PLoS Biology*, vol. 13, no. 7, p. e1002191, 2015.

[111] S. Kommineni, D. J. Bretl, V. Lam, R. Chakraborty, M. Hayward, P. Simpson, Y. Cao, P. Bousounis, C. J. Kristich, and N. H. Salzman, "Bacteriocin production augments niche competition by enterococci in the mammalian gastrointestinal tract.," *Nature*, vol. 526, no. 7575, pp. 719–722, 2015.

[112] E. Bruger and C. Waters, "Sharing the sandbox: Evolutionary mechanisms that maintain bacterial cooperation," *F1000Research*, vol. 4, p. 1504, 2015.

[113] S. A. West, A. S. Griffin, A. Gardner, and S. P. Diggle, "Social evolution theory for microorganisms," *Nature Reviews Microbiology*, vol. 4, no. August, pp. 597–607, 2006.

[114] Y. Xiao, M. T. Angulo, J. Friedman, M. K. Waldor, S. T. Weiss, and Y.-Y. Liu, "Mapping the ecological networks of microbial communities," *Nature Communications*, vol. 8, p. 2042, 2017.

[115] O. Hallatschek, P. Hersen, S. Ramanathan, and D. R. Nelson, "Genetic drift at expanding frontiers promotes gene segregation.," *Proceedings of the National Academy of Sciences of the United States of America*, vol. 104, no. 50, pp. 19926–19930, 2007.

[116] F. L. Hellweger, R. J. Clegg, J. R. Clark, C. M. Plugge, and J.-U. Kreft, "Advancing microbial sciences by individual-based modelling," *Nature Reviews Microbiology*, vol. 14, pp. 461–471, 2016.

[117] E. Frey, "Evolutionary game theory: Theoretical concepts and applications to microbial communities," *Physica A: Statistical Mechanics and its Applications*, vol. 389, no. 20, pp. 4265–4298, 2010.

[118] M. A. Nowak, *Evolutionary Dynamics*. Harvard University Press, 1 ed., 2006.

[119] B. Momeni, L. Xie, and W. Shou, "Lotka-Volterra pairwise modeling fails to capture diverse pairwise microbial interactions," *eLife*, vol. 6, p. e25051, 2017.

[120] E. Bairey, E. D. Kelsic, and R. Kishony, "High-order species interactions shape ecosystem diversity," *Nature Communications*, vol. 7, p. 12285, 2016.

[121] T. Reichenbach, M. Mobilia, and E. Frey, "Coexistence versus extinction in the stochastic cyclic Lotka-Volterra model," *Physical Review E - Statistical, Nonlinear, and Soft Matter Physics*, vol. 74, no. 5, p. 051907, 2006.

[122] C. Gardiner, *Handbook of Stochastic Methods*. Springer, 1997.

[123] P. Moons, C. W. Michiels, and A. Aertsen, "Bacterial interactions in biofilms bacterial interactions in biofilms," *Critical Reviews in Microbiology*, vol. 35, no. 3, pp. 157–168, 2009.

[124] C. D. Nadell, K. Drescher, and K. R. Foster, "Spatial structure, cooperation, and competition in biofilms," *Nature Reviews Microbiology*, vol. 14, pp. 589–600, 2016.

[125] A. M. Turing, "The Chemical Basis of Morphogenesis," *Philosophical Transactions of the Royal Society of London, Series B, Biological Sicences*, vol. 237, no. 641, pp. 37–72, 1952.

[126] A. J. Koch and H. Meinhardt, "Biological pattern formation: From basic mechanisms to complex structures," *Reviews of Modern Physics*, vol. 66, no. 4, pp. 1481–1507, 1994.

[127] M. Cross and H. Greenside, *Pattern Formation and Dynamics in Nonequilibrium Systems*. Cambridge University Press, 2009.

[128] J. Halatek and E. Frey, "Rethinking pattern formation in reaction-diffusion systems," *Nature Physics*, vol. 14, pp. 507–514, 2018.

[129] W. P. J. Smith, Y. Davit, J. M. Osborne, W. Kim, K. R. Foster, and J. M. Pitt-Francis, "Cell morphology drives spatial patterning in microbial communities," *Proceedings of the National Academy of Sciences*, vol. 114, no. 3, pp. E280–E286, 2017.

[130] J. A. Cole, L. Kohler, J. Hedhli, and Z. Luthey-Schulten, "Spatially-resolved metabolic cooperativity within dense bacterial colonies," *BMC Systems Biology*, vol. 9, no. 1, p. 15, 2015.

[131] H. Levine, I. Aranson, L. Tsimring, and T. V. Truong, "Positive genetic feedback governs cAMP spiral wave formation in Dictyostelium.," *Proceedings of the National Academy of Sciences of the United States of America*, vol. 93, no. 13, pp. 6382–6, 1996.

[132] D. Lopez, H. Vlamakis, and R. Kolter, "Biofilms," *Cold Spring Harbor Perspectives in Biology*, pp. 1–12, 2010.

[133] H. C. Flemming and J. Wingender, "The biofilm matrix," *Nature Reviews Microbiology*, vol. 8, no. 9, pp. 623–633, 2010.

[134] P. S. Stewart and J. W. Costerton, "Antibiotic resistance of bacteria in biofilms," *Lancet*, vol. 358, no. 9276, pp. 135–138, 2001.

[135] N. Høiby, T. Bjarnsholt, M. Givskov, S. Molin, and O. Ciofu, "Antibiotic resistance of bacterial biofilms," *International Journal of Antimicrobial Agents*, vol. 35, no. 4, pp. 322–332, 2010.

[136] K. Lewis, "Riddle of Biofilm Resistance," *Antimicrobial Agents and Chemothreapy*, vol. 45, no. 4, pp. 999–1007, 2001.

[137] M. Irsfeld, B. M. Prüß, and S. J. Stafslien, "Screening the mechanical stability of Escherichia coli biofilms through exposure to external, hydrodynamic shear forces," *Journal of Basic Microbiology*, vol. 54, no. 12, pp. 1403–1409, 2014.

[138] A. Persat, C. D. Nadell, M. K. Kim, F. Ingremeau, A. Siryaporn, K. Drescher, N. S. Wingreen, B. L. Bassler, Z. Gitai, and H. A. Stone, "The mechanical world of bacteria," *Cell*, vol. 161, no. 5, pp. 988–997, 2015.

[139] C. D. Nadell, K. Drescher, N. S. Wingreen, and B. L. Bassler, "Extracellular matrix structure governs invasion resistance in bacterial biofilms," *The ISME Journal*, vol. 9, no. 8, pp. 1700–1709, 2015.

[140] S. Kesel, B. von Bronk, C. Falcón García, A. Götz, O. Lieleg, and M. Opitz, "Matrix composition determines the dimensions of Bacillus subtilis NCIB 3610 biofilm colonies grown on LB agar," *RSC Advances*, vol. 7, no. 51, pp. 31886–31898, 2017.

[141] B. von Bronk, S. A. Schaffer, A. Götz, and M. Opitz, "Effects of stochasticity and division of labor in toxin production on two-strain bacterial competition in Escherichia coli," *PLoS Biology*, vol. 15, no. 5, p. e2001457, 2017.

[142] B. Hadimioglu, R. Stearns, and R. Ellson, "Moving Liquids with Sound: The Physics of Acoustic Droplet Ejection for Robust Laboratory Automation in Life Sciences," *Journal of Laboratory Automation*, vol. 21, no. 1, pp. 4–18, 2016.

[143] E. Hebisch, J. Knebel, J. Landsberg, E. Frey, and M. Leisner, "High Variation

of Fluorescence Protein Maturation Times in Closely Related Escherichia coli Strains," *PLoS ONE*, vol. 8, no. 10, p. e75991, 2013.

[144] A. B. Pardee, F. Jacob, and J. Monod, "The Genetic Control and Cytoplasmic Expression of "Inducibility" in the Synthesis of beta-galactosidase by E. Coli," *J. Mol. Biol*, vol. 1, pp. 165–178, 1959.

[145] F. J. Segerer, P. J. F. Röttgermann, S. Schuster, A. P. Alberola, S. Zahler, and J. O. Rädler, "A versatile method to generate multiple types of micropatterns," *Biointerphases*, vol. 11, no. 1, p. 011005, 2016.

[146] P. J. F. Röttgermann, A. P. Alberola, and J. O. Rädler, "Cellular self-organization on micro-structured surfaces," *Soft Matter*, vol. 10, pp. 2397–2404, 2014.

[147] J. A. Megerle, G. Fritz, U. Gerland, K. Jung, and J. O. Rädler, "Timing and dynamics of single cell gene expression in the arabinose utilization system.," *Biophysical journal*, vol. 95, no. 4, pp. 2103–2115, 2008.

[148] Nikon Corporation, "Research Stereo Microscope SMZ25/SMZ18," tech. rep., Nikon Corporation, Tokyo, Japan, 2013.

[149] R. Tu, *Ray Optics Simulation.* https://ricktu288.github.io/ray-optics/, 2016.

[150] N. Otsu, "A threshold selection method from gray-level histograms," *IEEE Transactions on Systems, Man, and Cybernetics*, vol. 9, no. 1, pp. 62–66, 1979.

[151] J. Kittler and J. Illingworth, "Minimum error thresholding," *Pattern Recognition*, vol. 19, no. 1, pp. 41–47, 1986.

[152] J. Canny, "A Computational Approach to Edge Detection," *IEEE Transactions on Pattern Analysis and Machine Intelligence*, vol. PAMI-8, no. 6, pp. 679–698, 1986.

[153] A. Dragoš, H. Kiesewalter, M. Martin, C. Y. Hsu, R. Hartmann, T. Wechsler, C. Eriksen, S. Brix, K. Drescher, N. Stanley-Wall, R. Kümmerli, and Á. T. Kovács, "Division of Labor during Biofilm Matrix Production," *Current Biology*, vol. 28, pp. 1903–1913, 2018.

[154] Y. Lecun, Y. Bengio, and G. Hinton, "Deep learning," *Nature*, vol. 521, no. 7553, pp. 436–444, 2015.

[155] M. T. Wetherington and J. E. Keymer, "What Does Not Kill You Makes You Stronger," *Trends in Microbiology*, vol. 25, no. 8, pp. 605–607, 2017.

[156] L. Perko, *Differential Equations and Dynamical Systems.* New York: Springer, 3rd ed., 2001.

[157] L. Gray, "A Mathematician Looks at Wolfram's New Kind of Science," *Notices of the American Mathematical Society*, vol. 50, no. 2, pp. 200–211, 2003.

[158] R. Erban, J. Chapman, and P. Maini, "A practical guide to stochastic simulations of reaction-diffusion processes," *arXiv*, no. 0704.1908, 2007.

[159] A. Kicheva, P. Pantazis, T. Bollenbach, Y. Kalaidzidis, T. Bittig, F. Jülicher, and M. González-Gaitán, "Kinetics of Morphogen," *Science*, vol. 315, no. 5811, pp. 521–525, 2007.

[160] O. Wartlick, A. Kicheva, and M. González-Gaitán, "Morphogen gradient formation.," *Cold Spring Harbor perspectives in biology*, vol. 1, p. a001255, 2009.

[161] S. Liang, J. Xu, L. Weng, H. Dai, X. Zhang, and L. Zhang, "Protein diffusion in agarose hydrogel in situ measured by improved refractive index method," *Journal of Controlled Release*, vol. 115, no. 2, pp. 189–196, 2006.

[162] R. S. Kamath and H. R. Bungay, "Growth of Yeast Colonies on Solid Media," *Journal of General Microbiology*, no. 1988, pp. 3061–3069, 1988.

[163] B. von Bronk, A. Götz, and M. Opitz, "Locality of interactions in three-strain bacterial competition in E.coli (submitted for publication)," 2018.

[164] K. S. Korolev, M. J. I. Müller, N. Karahan, A. W. Murray, O. Hallatschek, D. R. Nelson, M. J. Muller, N. Karahan, A. W. Murray, O. Hallatschek, and D. R. Nelson, "Selective sweeps in growing microbial colonies," *Physical Biology*, vol. 9, p. 026008, 2013.

[165] J. Kayser, C. Schreck, M. Gralka, D. Fusco, and O. Hallatschek, "Collective motion conceals fitness differences in crowded cellular populations," *bioRxiv*, p. 267286, 2018.

[166] M. Feldgarden and M. A. Riley, "The Phenotypic and Fitness Effects of Colicin Resistance in Escherichia coli K-12," *Evolution*, vol. 53, no. 4, pp. 1019–1027, 1999.

[167] Steland, *Bassiswissen Statistik*. Berlin Heidelberg: Springer-Verlag, 2010.

[168] J. Cohen, *Statistical Power Analysis for the Behavioral Sciences*. Lawrence Erlbaum Associates, 2nd ed., 1988.

[169] A. Stöcker, S. Brockhaus, S. Schaffer, B. von Bronk, M. Opitz, and S. Greven, "Boosting Functional Response Models for Location, Scale and Shape with an Application to Bacterial Competition (manuscript in preparation)," 2018.

[170] C. Ratzke, J. Denk, and J. Gore, "Ecological suicide in microbes," *Nature Ecology and Evolution*, vol. 2, no. 5, pp. 867–872, 2018.

[171] E. D. Kelsic, J. Zhao, K. Vetsigian, and R. Kishony, "Counteraction of antibiotic production and degradation stabilizes microbial communities," *Nature*, vol. 521, pp. 516–519, 2015.

[172] M. Gralka, F. Stiewe, F. Farrell, W. Möbius, B. Waclaw, and O. Hallatschek, "Allele surfing promotes microbial adaptation from standing variation," *Ecology Letters*, vol. 19, pp. 889–898, 2016.

[173] F. D. Farrell, M. Gralka, O. Hallatschek, and B. Waclaw, "Mechanical interactions in bacterial colonies and the surfing probability of beneficial mutations," *Journal of the Royal Society Interface*, vol. 14, p. 20170073, 2017.

[174] J. MacQueen, "Some methods for classification and analysis of multivariate observations," *Proceedings of the Fifth Berkeley Symposium on Mathematical Statistics and Probability*, vol. 1, no. 233, pp. 281–297, 1967.

[175] C. Ratzke and J. Gore, "Self-organized patchiness facilitates survival in a cooperatively growing Bacillus subtilis population," *Nature Microbiology*, vol. 1, p. 16022, 2016.

[176] M. L. Zorn, A. K. Marel, F. J. Segerer, and J. O. Rädler, "Phenomenological approaches to collective behavior in epithelial cell migration," *Biochimica et Biophysica Acta - Molecular Cell Research*, vol. 1853, no. 11, pp. 3143–3152, 2015.

[177] A. Kalziqi, D. Yanni, J. Thomas, S. L. Ng, S. Vivek, B. K. Hammer, and P. J. Yunker, "Immotile Active Matter: Activity from Death and Reproduction," *Physical Review Letters*, vol. 120, no. 1, p. 18101, 2018.

[178] F. Wu, B. G. C. van Schie, J. E. Keymer, and C. Dekker, "Symmetry and scale orient Min protein patterns in shaped bacterial sculptures.," *Nature nanotechnology*, vol. 10, no. 8, pp. 719–726, 2015.

[179] J. Kayser, C. F. Schreck, Q. Yu, M. Gralka, and O. Hallatschek, "Emergence of evolutionary driving forces in pattern-forming microbial populations," *Philosophical Transactions of the Royal Society B: Biological Sciences*, vol. 373, p. 20170106, 2018.

[180] S. Luria and M. Delbrück, "Mutations of Bacteria from Virus Sensitivity to Virus Resistance.," *Genetics*, vol. 28, no. 6, pp. 491–511, 1943.

[181] R. Chait, J. Ruess, T. Bergmiller, G. Tkačik, and C. C. Guet, "Shaping bacterial population behavior through computer-interfaced control of individual cells," *Nature Communications*, vol. 8, p. 1535, 2017.

[182] K. Drescher, J. Dunkel, C. D. Nadell, S. van Teeffelen, I. Grnja, N. S. Wingreen, H. A. Stone, and B. L. Bassler, "Architectural transitions in Vibrio cholerae biofilms at single-cell resolution," *Proceedings of the National Academy of Sciences*, vol. 113, no. 14, pp. E2066–E2072, 2016.

[183] P. Nelson, *Biological Physics : Energy , Information , Life*. New York: W. H. Freeman and Company, 1st ed., 2002.

[184] R. Phillips, J. Kondev, J. Theriot, and H. G. Garcia, *Physical Biology of the Cell*. New York: Garland Science, Taylor & Francis Group, LLC, 2nd ed., 2013.

Danksagung

"Art is I; science is we"

Claude Bernard

Gemäß dem oben genannten Motto möchte ich denjenigen danken, die mich bei meiner Arbeit unterstützt haben.

PD Dr. Madeleine Opitz, Dir danke ich zunächst einmal Dir für Deinen Einsatz für die Gruppe und jeden Einzelnen darin, insbesondere trotz Schwangerschaft und Mutterschutz, für Deine Motivation und Deinen Optimismus (z.B. bei Revisions), für die mir gewährte Freiheit, für eine super Gruppenatmosphäre, natrürlich für Dein Organisationstalent und für alles, was ich noch vergessen habe!

Prof. Dr. Joachim Rädler & QBM danke ich für das Stipendium, das meine Forschung überhaupt erst ermöglicht hat. **Vielen Dank!**

QBM danke ich noch einmal gesondert für die unterhaltsame Schulklassenatmosphäre, die spannende Fortbildungen und tollen Retreats (insbesondere Venedig).

CeNS & NIM dafür, dass sie meinen Aufbau bezahlt haben. Und CeNS nochmal gesondert für den super Austausch mit der UC Santa Barbara über das JNN.

Sophia, Dir möchte ich ganz besonders für Deinen vollen Einsatz für unser Projekt während Masterarbeit, HiWi-Zeit und noch darüberhinaus danken!

Alex, danke für die super Zusammenarbeit, dafür, dass wir uns so gut ergänzt haben (also, dass Du meine Wissenslücken ausgefüllt hast ;-)), Dein Hammer-Arbeitsethos und Deine wahnsinnige Hilfsbereitschaft!

Der AG Opitz, insbesondere Andi and Sara, aber auch allen anderen Studenten und HiWis der letzten Jahre für Eure Hilfsbereitschaft, die gute Zusammenarbeit und Atmosphäre.

Meinen Studenten, Sophia, Martin, Petra, Tim, & Moritz, dafür, dass ich beim Betreuen selber viel lernen konnte. **Martin** nochmal ganz besonders für die Wahl der Variablennamen und ein witziges Antholz 2016.

Meinem Büro, Sophia, Tobi, Christoph, Matthias, Anita, Judith, Miriam, für die lustige Atmosphäre. Ich hoffe, ihr konntet Euch nicht alle meine Sprüche merken, um sie auf dem Doktorhut zu verarbeiten.

Der Dinnerrunde mit Alexandra, Ricarda, David und Peter für witzige Abende!

Dem Rest vom Lehrstuhl für das Miteinander und die Winter Schools in Antholz.